



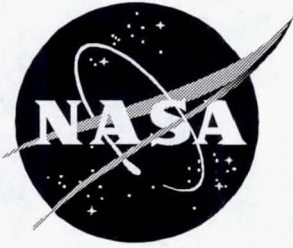
1N-02  
1998  
046311  
80P  
NASA Technical Paper 3669

# Cavity Unsteady-Pressure Measurements at Subsonic and Transonic Speeds

---

*Maureen B. Tracy and E. B. Plentovich*

December 1997



NASA Technical Paper 3669

# Cavity Unsteady-Pressure Measurements at Subsonic and Transonic Speeds

---

*Maureen B. Tracy and E. B. Plentovich*  
*Langley Research Center • Hampton, Virginia*

National Aeronautics and Space Administration  
Langley Research Center • Hampton, Virginia 23681-2199

December 1997

Available electronically at the following URL address: <http://techreports.larc.nasa.gov/ltrs/ltrs.html>

Printed copies available from the following:

NASA Center for AeroSpace Information  
800 Elkridge Landing Road  
Linthicum Heights, MD 21090-2934  
(301) 621-0390

National Technical Information Service (NTIS)  
5285 Port Royal Road  
Springfield, VA 22161-2171  
(703) 487-4650

REPORT DOCUMENTATION PAGE			Form Approved OMB No. 0704-0188	
Public reporting burden for this collection of information is estimated to average 1 hour per response, including the time for reviewing instructions, searching existing data sources, gathering and maintaining the data needed, and completing and reviewing the collection of information. Send comments regarding this burden estimate or any other aspect of this collection of information, including suggestions for reducing this burden, to Washington Headquarters Services, Directorate for Information Operations and Reports, 1215 Jefferson Davis Highway, Suite 1204, Arlington, VA 22202-4302, and to the Office of Management and Budget, Paperwork Reduction Project (0704-0188), Washington, DC 20503.				
1. AGENCY USE ONLY (Leave blank)	2. REPORT DATE December 1997	3. REPORT TYPE AND DATES COVERED Technical Paper		
4. TITLE AND SUBTITLE Cavity Unsteady-Pressure Measurements at Subsonic and Transonic Speeds		5. FUNDING NUMBERS WU 505-68-30-03		
6. AUTHOR(S) Maureen B. Tracy and E. B. Plentovich				
7. PERFORMING ORGANIZATION NAME(S) AND ADDRESS(ES) NASA Langley Research Center Hampton, VA 23681-2199		8. PERFORMING ORGANIZATION REPORT NUMBER L-17560		
9. SPONSORING/MONITORING AGENCY NAME(S) AND ADDRESS(ES) National Aeronautics and Space Administration Washington, DC 20546-0001		10. SPONSORING/MONITORING AGENCY REPORT NUMBER NASA TP-3669		
11. SUPPLEMENTARY NOTES				
12a. DISTRIBUTION/AVAILABILITY STATEMENT Unclassified-Unlimited Subject Category 02 Availability: NASA CASI (301) 621-0390		12b. DISTRIBUTION CODE		
13. ABSTRACT (Maximum 200 words) An experimental investigation was conducted in the Langley 8-Foot Transonic Pressure Tunnel to determine the flow characteristics of rectangular cavities with varying relative dimensions at subsonic and transonic speeds. Cavities were tested with width-to-depth ratios of 1, 4, 8, and 16 for length-to-depth ratios $l/h$ of 1 through 17.5. The maximum cavity depth was 2.4 in., and the turbulent boundary layer approaching the cavity was approximately 0.5 in. thick. Unsteady- and mean static-pressure measurements were made at free-stream Mach numbers from 0.20 to 0.95 at a unit Reynolds number per foot of approximately $3 \times 10^6$ ; however, only unsteady-pressure results are presented in this paper. Results indicate that as $l/h$ increases, cavity flows changed from resonant to nonresonant with resonant amplitudes decreasing gradually. Resonant spectra are obtained largely in cavities with mean static-pressure distributions characteristic of open and transitional flows. Resonance sometimes occurred for closed flow. Increasing cavity width or decreasing cavity depth while holding $l/h$ fixed had the effect of increasing resonant amplitudes and sometimes induced resonance. The effects due to changes in width are more pronounced. Decreasing Mach number has the effect of broadening the resonances.				
14. SUBJECT TERMS Cavity flows; Unsteady flows; Transonic speeds; Pressure measurements; Cavity resonance		15. NUMBER OF PAGES 78		16. PRICE CODE A05
17. SECURITY CLASSIFICATION OF REPORT Unclassified	18. SECURITY CLASSIFICATION OF THIS PAGE Unclassified	19. SECURITY CLASSIFICATION OF ABSTRACT Unclassified	20. LIMITATION OF ABSTRACT	

## Contents

Summary . . . . .	1
Introduction . . . . .	1
Symbols . . . . .	1
Background . . . . .	2
Cavity Flow Field Types for Supersonic Speeds . . . . .	2
Subsonic and Transonic Flow Field Types . . . . .	3
Experimental Methods . . . . .	4
Model Description . . . . .	4
Wind Tunnel and Test Conditions . . . . .	4
Instrumentation and Measurements . . . . .	5
Data Reduction . . . . .	5
Results and Discussion . . . . .	6
Presentation of Data . . . . .	6
Effect of Transducer Location . . . . .	7
Effect of Cavity $l/h$ and Correlation With Open, Transitional, and Closed Flows . . . . .	7
Flow Field Analysis Using Cross-Channel Analysis Between Transducers . . . . .	8
Effect of Cavity Width . . . . .	8
Effect of Cavity Depth . . . . .	8
Effect of Mach Number . . . . .	8
Concluding Remarks . . . . .	9
References . . . . .	9
Figures . . . . .	11

## Summary

An experimental investigation was conducted in the Langley 8-Foot Transonic Pressure Tunnel to determine the flow characteristics of rectangular cavities with varying relative dimensions at subsonic and transonic speeds. Cavities were tested with width-to-depth ratios  $w/h$  of 1, 4, 8, and 16 for length-to-depth ratios  $l/h$  of 1 through 17.5. The maximum cavity dimensions were 42.0 in. in length, 9.6 in. in width, and 2.4 in. in depth. The boundary layer approaching the cavity was turbulent and had an approximate thickness of 0.5 in. Unsteady- and mean static-pressure measurements were made at free-stream Mach numbers  $M_\infty$  from 0.20 to 0.95 at a unit Reynolds number per foot  $R_\infty$  of approximately  $3 \times 10^6$ . Unsteady-pressure results are presented in this paper, which is a companion paper to one previously published on static-pressure results (NASA TP-3358).

Unsteady-pressure results indicate that, as  $l/h$  increases, cavity flows changed from resonant to nonresonant with resonant amplitudes decreasing gradually. Resonant spectra are obtained largely in cavities with mean static-pressure distributions characteristic of open and transitional flows. Resonance does occur for closed flow in some cases. Other results indicate that increasing cavity width or decreasing cavity depth while holding  $l/h$  fixed has the effect of increasing resonant amplitudes and sometimes inducing resonance. The effects due to changes in width are more pronounced. Decreasing  $M_\infty$  has the effect of broadening the resonances. The effects of varying length and  $M_\infty$  on the resonant frequencies are consistent with the Rossiter equation. The values of the resonant frequencies display a slight sensitivity to changes in width  $w$  and depth  $h$  for low values of  $l/h$ .

## Introduction

With renewed interest in internal carriage of stores and the need to safely separate stores over the entire flight envelope of the aircraft, knowing the cavity flow environments for all operational speeds is important. Many investigations, both primarily experimental (refs. 1 through 29) and primarily computational (refs. 30 through 40), have been conducted to study the flow fields in rectangular cavities. These studies largely concentrated on mean static-pressure distributions and/or unsteady-pressure spectra in cavities. They were conducted at speeds ranging from subsonic through hypersonic, with the largest amount of effort concentrated on supersonic speeds since military aircraft generally operate supersonically. Radiated acoustic pressure (refs. 24, 25, 27, and 28) and store separation characteristics (refs. 18 through 23) have also been obtained in some studies.

Carrying weapons internally has aerodynamic advantages in flight. Cavities (open weapons bays) in aerodynamic surfaces, however, can generate both steady and unsteady flow disturbances. Changes in mean static-pressure distributions inside the cavity can result in large pressure gradients, and the unsteady flow disturbances can generate self-sustaining oscillations which, in turn, generate acoustic tones that radiate from the cavity. Both the steady and the unsteady flows can present difficulties for store separation from an internal weapons bay. The steady flows can generate large nose-up pitching moments, and the unsteady flows can induce structural vibration. To ensure safe carriage and separation for subsonic and transonic speeds, the flow fields that develop in cavities must be thoroughly characterized. The experimental study described herein was designed to accomplish this by obtaining mean static-pressure distributions and unsteady-pressure spectra in cavities with varying relative dimensions. The primary parameter of interest was the cavity length-to-depth ratio  $l/h$  because the cavity flow field is known to depend on  $l/h$  (ref. 6). Two other parameters, free-stream Mach number  $M_\infty$  and the ratio of cavity width-to-depth  $w/h$ , are included in this study as they can affect the values of  $l/h$  at which flow types change (refs. 6 and 2, respectively). (Other parameters that affect the values of  $l/h$  at which flow types change, not examined in this study, include the ratio of boundary-layer height to cavity depth (ref. 1) and the location of stores in the cavity (ref. 21).) Static-pressure data from this study have been used to define flow field types and to determine parameter sensitivities (ref. 5). Unsteady-pressure results are presented in this paper and are used to identify parameter combinations that support cavity resonance and the effects of parameter changes. This report is a companion paper to the previously published paper on static-pressure results, NASA TP-3358 (ref. 5). An electronic "Supplement to NASA TP-3669" containing the spectral data presented graphically in this report in ASCII format is available on request as a CD-ROM. A request form is included at the back of this report.

## Symbols

$A_1, A_2, A_3$	constants from ramped sinusoidal function
AC	alternating current
$a_\infty$	free-stream acoustic wave speed, fps
$C_p$	pressure coefficient, $\frac{p - p_\infty}{q_\infty}$
$f$	frequency, Hz
$f \frac{l}{U_\infty}$	reduced frequency
$f_m$	frequency of lengthwise acoustic mode, Hz
FPL	fluctuating-pressure level, normalized with respect to $q_\infty$ , dB

$h$	cavity depth, in.
$k$	empirical ratio of shear layer and free-stream velocities, function of $M_\infty$ , 0.57 (ref. 6)
$l$	cavity length, measured in streamwise direction, in.
$M$	Mach number
$M_\infty$	free-stream Mach number
$m$	longitudinal mode number
OASPL	overall sound pressure level, dB
$p$	measured surface static pressure, psi
$p'$	measured unsteady pressure, psi
$p'_{rms}$	root-mean-square pressure, $\sqrt{(p')^2}$ , psi
$p_\infty$	free-stream static pressure, psi
$p_{t,\infty}$	free-stream total pressure, psi
$q_\infty$	free-stream dynamic pressure, psi
$R_\infty$	free-stream unit Reynolds number per foot
SPL	sound pressure level, normalized with respect to audible sound, $2.9 \times 10^{-9}$ psi, dB
$T_{t,\infty}$	free-stream total temperature, °F
$U$	velocity, fps
$U_\infty$	free-stream velocity, fps
$w$	cavity width, in.
$x$	distance in streamwise direction, positive downstream, in. (see fig. 4(b))
$y$	distance in spanwise direction, positive left facing upstream, in. (see fig. 4(b))
$z$	distance normal to flat plate, positive down, in. (see fig. 4(b))
$\alpha$	empirical constant related to phase between instabilities in shear layer and upstream traveling pressure waves, function of $l/h$ , 0.25 (ref. 6)
$\gamma$	ratio of specific heat of test gas at constant pressure to that at constant volume, 1.4 for air
$\delta$	boundary-layer thickness, measured at center of leading edge of cavity, in.

## Background

Flow field types for transonic speeds have been identified based on a detailed evaluation of static-pressure measurements (ref. 5) and referenced to established flow field types for cavities in supersonic flows (refs. 2, 20, and 21). The flow field types identified for supersonic

speeds are used for reference because off-surface flow visualization and extensive computational studies are available for validation. Figure 1 presents schematics of the supersonic flow field types and the associated characteristic mean static-pressure distributions. These flow field types—open, closed, transitional-open, and transitional-closed—are briefly discussed in the following paragraphs. (It is important to note that the use of the word “transitional” in relation to cavity flows does not refer to transition from laminar to turbulent flow.) Following this discussion, a description of the flow field types identified for transonic flows is presented. As with supersonic cavity flow types, the subsonic and transonic flow types are defined by their characteristic mean static-pressure distributions and the values of  $l/h$  identified as bounding the various flow types are approximate, limited by the increments used in varying  $l/h$ .

## Cavity Flow Field Types for Supersonic Speeds

The first cavity flow field type identified for supersonic speeds generally occurs when the cavity is “deep” (a small value of  $l/h$ ), as is typical of bomber aircraft bays, and is termed “open cavity flow” (fig. 1(a)). Open flow occurs in cavities with values of  $l/h$  less than or equal to 10. For this regime, the flow essentially bridges the cavity and a shear layer is formed over the cavity. This flow produces a nearly uniform static-pressure distribution along the floor of the cavity which is desirable for safe store separation. However, when open cavity flow occurs, a cavity resonance can be sustained. The mechanism that produces this resonance is understood to be the reinforcement between instabilities in the shear layer and upstream-traveling pressure waves generated at the aft wall by the time-varying impingement of the shear layer. These oscillations can generate high intensity acoustic tones that can induce vibrations in the surrounding structure, including the separating store, and lead to structural fatigue (refs. 29 and 40). The frequencies at which these tones occur can be predicted with a semi-empirical equation known as the modified Rossiter equation (ref. 8)

$$f_m \frac{l}{U_\infty} = \frac{m - \alpha(l/h)}{M_\infty \sqrt{1 + [(\gamma - 1)/2] M_\infty^2} + 1/k(M_\infty)}$$

Here  $f_m$  is the frequency of a given lengthwise acoustic mode;  $l$ , the cavity length;  $U_\infty$ , the free-stream velocity;  $m$ , the longitudinal mode number;  $M_\infty$ , the free-stream Mach number; and  $\gamma$ , the ratio of specific heat of the test gas at constant pressure to that at constant volume (taken to be equal to 1.4 for perfect gases). Two empirical constants are in this equation:  $\alpha$ , which depends on  $l/h$  and is related to the phase between the instabilities in the shear layer and the upstream traveling pressure waves, and  $k$ ,

which depends on  $M_\infty$  and gives the relative speed of the instabilities in the shear layer to free stream. The values for the coefficients  $\alpha$  and  $k$  are taken from reference 6 as 0.25 and 0.57, respectively. (The value of  $\alpha$  was obtained for an  $l/h$  value of 4.0 and  $k$  was an average of values obtained for a range of  $M_\infty$  from 0.40 to 1.20.) The modification (ref. 8) of the Rossiter equation (ref. 6) equates the cavity sound speed to the stagnation sound speed to accommodate high-speed flows.

The second type of cavity flow identified for supersonic speeds occurs for cavities that are "shallow" (large values of  $l/h$ ), as is typical of missile bays on fighter aircraft, and is termed "closed cavity flow" (fig. 1(b)). Closed flow occurs for cavities with values of  $l/h$  greater than or equal to 13. In this regime, the flow separates at the forward face of the cavity, reattaches at some point along the cavity floor, and separates again before reaching the rear cavity face. This flow produces a mean static-pressure distribution with low pressure in the forward region, a plateau in the attached region, and high pressure in the aft region. Impingement and exit shocks are observed. The adverse static-pressure gradient produced by closed cavity flow can cause the separating store to experience large pitching moments that turn the store nose into the cavity. Acoustic tones generally do not occur for closed cavity flow at supersonic speeds.

The third and fourth cavity flow field types defined for supersonic speeds are termed "transitional (transitional-open and transitional-closed)" and are flow fields that occur for cavities that have values of  $l/h$  that fall between closed and open cavity flow, that is, values of  $l/h$  between approximately 10 and 13. Transitional-closed cavity flow (fig. 1(c)) occurs when  $l/h$  is decreased from a value corresponding to closed cavity flow. The change in flow field type is signaled by the collapse of the impingement and exit shocks into a single shock and the disappearance of the plateau in the mean static-pressure distribution. The shock signifies that although it does not remain attached, the flow has impinged on the floor. Similar to closed cavity flow, large static-pressure gradients occur along the cavity floor and can contribute to large nose-up pitching moments. With a very small reduction in  $l/h$  from the value corresponding to the transitional-closed cavity flow, the impingement-exit shock wave abruptly changes to a series of compression wavelets; this indicates that although the shear layer no longer impinges on the cavity floor, it does turn into the cavity. This type of flow is referred to as "transitional-open cavity flow" (fig. 1(d)). For this type of flow field, longitudinal pressure gradients in the cavity are not as large as for transitional-closed cavity flow, and consequently, the problem of store nose-up pitching moment is not as severe as closed cavity flows. The acoustic fields for the transitional-

closed and transitional-open flow fields have not been determined.

### Subsonic and Transonic Flow Field Types

Figure 2 (reproduced from ref. 5) gives the characteristic static-pressure distributions for the various flow field types defined for subsonic and transonic speeds. As with supersonic flow, open and closed cavity flow occur. For the range of  $l/h$  between those for open and closed flow, a gradual change occurs from open to closed flow and thus a single transitional type flow is defined (rather than transitional-open and transitional-closed as for supersonic flow). In this regime, the flow turns into the cavity and may or may not impinge on the cavity floor before turning out and exiting. At transonic speeds, flows with static-pressure distributions similar to the supersonic transitional-open and transitional-closed bound the transitional flow regime as indicated in figure 2. The characteristics of the static-pressure distributions used to define the flow types in reference 5 are summarized and given subsequently.

Open cavity flow has a uniform pressure distribution ( $C_p \approx 0$ ) for values of  $x/l$  up to approximately 0.6. Aft of that point the pressure distribution increases with increasing  $x/l$  and has a concave up shape. The change from open to transitional cavity flow (as  $l/h$  increases) is identified by a change in pressure distribution from concave up to concave down in the aft portion of the cavity. (This distribution is similar to that for supersonic transitional-open flow.) The concave down pressure distribution for  $x/l$  above approximately 0.6 is typical of transitional cavity flow for transonic speeds. As  $l/h$  increases, the distribution gradually changes to one marked by a uniform increase from negative values near the front face to large positive values near the aft face (similar to the supersonic transitional-closed distribution). The flow becomes closed (with increasing  $l/h$ ) when an inflection point occurs in the pressure distribution at approximately  $x/l = 0.5$ . With further increase in  $l/h$ , the inflection point becomes a plateau (a distribution typical of closed cavity flow observed at supersonic speeds). With still further increase in  $l/h$ , a dip in pressure develops aft of the region of level pressure and forward of the aft pressure rise. The maximum value of the closed pressure distribution remains approximately the same as that observed at the boundary with transitional flow. Again, note that the boundaries between the flow types are approximate and are limited by the spacing between measurement locations and the increments by which  $l/h$  was changed.

The occurrence of the various flow field types was found to depend on free-stream Mach number  $M_\infty$ , cavity length-to-height ratio  $l/h$ , and cavity width-to-height ratio  $w/h$ . A sketch from reference 5 showing this

dependence is provided as figure 3. The flow field types that occurred for each combination of  $M_\infty$  and  $l/h$  are indicated for four configurations each with different  $w/h$  values. Boundaries have been drawn delimiting the flow field types for each configuration. At transonic speeds, as seen in figure 3, open flow occurs in cavities with  $l/h$  values up to a maximum value between 6 and 8 and closed flow occurs for cavities with  $l/h$  values down to a minimum value between 9 and 15. Consequently, transitional cavity flow can occur for a range of  $l/h$  values as narrow as 1 ( $w/h = 1$  and  $M_\infty = 0.20$ ) and as broad as 7 ( $w/h = 8$  and  $M_\infty = 0.95$ ). The effect of these flow fields on the store carriage and separation characteristics is similar to that observed at supersonic speeds for like pressure distributions (ref. 23).

## Experimental Methods

### Model Description

A flat plate with a rectangular, three-dimensional cavity was mounted in the center of the tunnel as shown in figure 4(a). The plate, shown schematically in figure 4(b), was 111.0 in. long, 48.0 in. wide, and 1.0 in. thick. It had a 6.0-in-long elliptic leading-edge contour and a 12-in. wedge-shaped trailing-edge contour. A boundary-layer transition strip was applied to the leading edge of the flat plate in order to ensure that the flow approaching the cavity was fully turbulent for all conditions. According to the recommendations in references 41 and 42, a strip of No. 60 grit was applied in a band of 0.10 in., approximately 1 in. aft of the leading edge of the flat plate. The model was supported horizontally along the centerline of the tunnel by six legs. The forward two legs on each side were swept forward to distribute longitudinally the model cross-sectional area for blockage considerations. Two guy wires were attached to opposite sides of the plate to increase lateral stiffness and stability. A fairing was placed around the cavity on the underside of the plate for aerodynamic purposes.

The cavity was located 36.0 in. aft of the leading edge of the flat plate. The maximum dimensions of the cavity were 42.0 in. long, 4.2 in. deep, and 9.6 in. wide. The length of the cavity could be varied by remote control of a sliding assembly (unsealed) that combined the aft cavity wall and a portion of the plate downstream of the cavity. (See fig. 4(b).) A number of cavity lengths

were tested from the 42.0 in. maximum to 1.2 in. The depth of the cavity could be varied by changing the position of the floor. For this test, the cavity floor was positioned to achieve depths of 0.6, 1.2, and 2.4 in. (Changing cavity depth required replacing the aft wall.) The width of the cavity could be varied by installing cavity side walls with different thicknesses. For this test, cavity widths were set at 2.4 and 9.6 in. (Changing cavity width required replacing the aft wall as well as the sliding component of the downstream plate.)

Brackets were positioned on the surface of the flat plate, downstream of the aft wall, to prevent the cantilevered portion of the sliding assembly from deflecting above the plate surface. The brackets were used for most configurations and consisted of two metal supports downstream of the cavity, positioned to overlap the sliding assembly and the flat plate. Figure 5(a) is a photograph of the brackets positioned on the model, and figure 5(b) is a sketch of the bracket details. The maximum distance the sliding assembly could be cantilevered forward of the brackets was approximately 6.5 in. Data were actually taken with the aft wall of the cavity positioned forward of the bracket leading edge at distances ranging from 0.0 to 6.0 in. (A model change was required to position the brackets for a specified range of aft wall movement. Several model changes were required to allow the aft wall to traverse the full length of the cavity.) The brackets were designed to minimize the interference on the upstream flow. No assessment of the impact the brackets had on the unsteady-pressure data was done.

### Wind Tunnel and Test Conditions

The test was conducted in the Langley 8-Foot Transonic Pressure Tunnel, which is a closed-circuit, continuous-flow, single-return pressure tunnel. The 8-Foot Transonic Pressure Tunnel is capable of operating at  $M_\infty$  from 0.20 to 1.30 and can achieve  $R_\infty$  from  $0.1 \times 10^6$  to  $5 \times 10^6$  by varying stagnation pressure  $p_{t,\infty}$  from 1.5 to 29.5 psi. (Free-stream conditions are for tunnel empty along the centerline of the test section.)

For this test, the flat plate was positioned along the centerline of the tunnel at angles of attack and yaw of  $0^\circ$ , and  $M_\infty$  was varied from 0.20 to 0.95 at unit Reynolds numbers between  $2 \times 10^6$  and  $5 \times 10^6$ . The nominal test matrix is given in the following table:

$M_\infty$	$R_\infty$	$U_\infty$ , fps	$a_\infty$ , fps	$p_{t,\infty}$ , psi	$T_{t,\infty}$ , °F	$q_\infty$ , psi	$\delta$ , in.
0.20	$2.2 \times 10^6$	230.3	1151.5	26	97	0.7	0.45
0.40	3.6	456.8	1142.0	22	101	2.2	0.48
0.60	4.7	671.1	1118.5	21	99	4.1	0.47
0.80	3.8	876.2	1095.3	14	104	4.2	0.50
0.90	3.4	976.4	1084.9	13	110	4.2	0.52
0.95	3.4	1019.8	1073.5	12	107	4.2	0.55

Although the model was large (3 percent tunnel blockage), reference 5 presents data that indicate no significant deviation existed from the tunnel calibration, and thus no corrections were applied to either  $M_\infty$  or  $U_\infty$  for this test.

The values for boundary-layer thickness given are estimates based on total-pressure measurements through the boundary layer and the traditional definition of boundary-layer thickness. The edge of the boundary layer is defined as the height above the surface at which  $U/U_\infty = 0.99$ . The value of  $U/U_\infty$  was calculated from the equation

$$\frac{U}{U_\infty} = \frac{M}{M_\infty} \sqrt{\frac{1 + 0.2M_\infty^2}{1 + 0.2M^2}}$$

obtained from reference 43. Total-pressure measurements were made with a total-pressure rake positioned at the leading edge of the cavity with the floor positioned flush with the plate and a  $\pm 10$ -psid ESP (electronically scanned pressure transducer). The quoted accuracy of the ESP is  $\pm 0.15$  percent full scale ( $\pm 0.02$  psi).

### Instrumentation and Measurements

The unsteady-pressure measurements were made with flush-mounted miniature dynamic pressure transducers. Figure 6 provides the instrumentation layout. The transducers were piezoresistive with a full-scale range of 5 psid and a resonant frequency of 85 kHz. In order to utilize the maximum sensitivity of the transducers, the mean component of the pressure measurement was removed. The first step in accomplishing this was installing the transducers in a differential configuration with a local static pressure as a reference (supplied to the back side of the diaphragm). Ten ft of 0.020-in. inner-diameter flexible tubing was used between the static-pressure orifice and the transducer in order to damp out any pressure oscillations in the reference pressure. All the transducers, except the one on the aft wall, used the pressure orifice at  $x = 2.0$  in.,  $y = 2.4$  in., and  $z = h$  as the reference. Since the aft wall typically experienced higher mean pressures than the cavity floor, the transducer in the aft wall used a separate local reference. The location of the aft wall reference was specified as  $y = 0.0$  in. and  $x = l$ , with a  $z$  coordinate that depended on the availability of pressure orifices in the various aft walls used for the various cavity depths. (The available locations ranged from 63 to 74 percent of the cavity depth.) A second step in removing any mean component in the signal (a possibility due to the physical separation between transducer and reference orifice) was to AC couple the instrumentation which electronically filtered out any mean offset.

Data were recorded on analog tape (frequency modulated) with standard IRIG (Inter-Range Instrumentation Group) wide-band format at a tape speed of 7.5 in/sec (modulation band of 0 to 10 kHz with a dynamic range of 50 dB). A sine wave calibration (150 dB at 1 kHz) was applied to each dynamic pressure transducer several times throughout the test and recorded as data.

The plate and cavity were instrumented with 148 static-pressure orifices. The description of the static-pressure instrumentation and data are presented in reference 5.

### Data Reduction

Following the test, the analog data were played back and digitized at 5 kHz with a 2.5-kHz antialiasing filter. The upper frequency of 2 kHz was chosen for presentation based on the expected resonant frequencies given the range of cavity lengths and flow speeds. Digitized data were divided into 49 blocks of 2048 points each. Blocks were Fourier analyzed by using a Hanning window, and the resulting spectral density estimates were averaged. This process produced averaged spectral density estimates (referred to as "spectra" in this report) with a resolution of 2.44 Hz and a 90 percent confidence interval between 78 and 125 percent of the true value (90 percent confidence that the spectral estimate will be between  $-2.2$  and  $+1.9$  dB of the true spectrum). This confidence estimation is based on a chi-square distribution which assumes an ergodic Gaussian random process and independence of the sample blocks. (See ref. 44, pp. 284-286.)

Data are presented in two forms, sound pressure level (SPL) as is customary in acoustics and uses a reference pressure that corresponds to the threshold of hearing:

$$\text{SPL} = 20 \log \left( \frac{p'_{rms}}{2.9 \times 10^{-9} \text{ psi}} \right)$$

and fluctuating pressure level (FPL) in which pressure is nondimensionalized by  $q_\infty$  as

$$\text{FPL} = 20 \log \left( \frac{p'_{rms}}{q_\infty} \right) = \text{SPL} + 20 \log \left( \frac{2.9 \times 10^{-9} \text{ psi}}{q_\infty} \right)$$

SPL is plotted as a function of frequency and FPL is plotted as a function of reduced frequency  $f \frac{l}{U_\infty}$ . All data are presented in both forms in this report. The latter form is used to facilitate the identification of Rossiter frequencies or to remove effects due to  $q_\infty$ .

Spectra, or more accurately autospectra, are obtained from the autocorrelation functions of individual signals from individual transducers. A cross spectrum can similarly be obtained from the cross-correlation function between two signals. The cross spectrum includes phase information from which it is possible to obtain the time delay between the two signals. (See ref. 45, pp. 66–68.) A linear phase shift indicates a constant propagation or convection speed between two measurement locations. A limited amount of cross-channel phase data is examined in this report.

## Results and Discussion

### Presentation of Data

The data presented in this report are predominantly from a single transducer (transducer 1), located at  $x = 0.3$  in. and  $y = 0.0$  in. (0.3 in. below the leading edge of the cavity on the forward wall). Although the unsteady-pressure spectra varied with location in the cavity, the data obtained from transducer 1 are considered to be most representative of the unsteady-pressure field and to contain the most information with which to discriminate between resonant and nonresonant conditions. Figures 7 through 10 provide data to support this choice and are discussed in the section "Effect of Transducer Location." (This section and the one entitled "Flow Field Analysis by Using Cross-Channel Analysis Between Transducers" are the only sections that include data from more than one transducer.) Figures 7 through 10 illustrate the variation in unsteady-pressure data with location in the cavity for typical resonant and nonresonant conditions. Figures 7 and 9 provide spectra  $SPL(f)$  obtained at all measurement locations in a resonant and a nonresonant cavity, respectively. Peak amplitudes from the spectra presented in figure 7 are plotted as a function of cavity location in figure 8. OASPL (overall sound pressure level obtained from the integration from 0 to 2 kHz) of the spectra presented in figure 9 are presented in figure 10 as a function of cavity location. Figure 11 provides the static-pressure distribution corresponding to figure 10.

Because the cavity flow type is most sensitive to the parameter  $l/h$  (ref. 6), the variable cavity model was designed to allow the most freedom in selecting values of  $l/h$  to study. For this study,  $l$  was varied from 1.2 to 42.0 in., whereas  $w$  and  $h$  were held constant for  $w/h = 1, 4, 8,$  and  $16$ . Figures 12, 13, 14, and 15 present spectra  $SPL(f)$  for all values of  $l/h$  for  $w/h = 1, 4, 8,$  and  $16$ , respectively. The figures are each divided into parts (a) through (f), which correspond to  $M_\infty = 0.20, 0.40, 0.60, 0.80, 0.90,$  and  $0.95$ , except figure 15, which has three parts corresponding to  $M_\infty = 0.80, 0.90,$  and  $0.95$ . Each part of figures 12 through 15 contains three groupings of plots

corresponding to open, transitional, and closed flow. For completeness, the plots in the top row of the figures contain spectra from all the values of  $l/h$  that were identified in reference 5 as supporting open, transitional, or closed flow. Below these plots, for clarity, there are selected plots of individual spectra (a maximum of three when available: spectra from the shortest, an intermediate, and the longest cavity length supporting each flow field type). These data are examined in the section "Effect of Cavity  $l/h$  and Correlation With Open, Transitional, and Closed Flows." Figure 16 summarizes the parameter combinations that support cavity resonance.

In order to attempt to gain more insight into the correlation between mean static-pressure distributions and unsteady-pressure spectra, cross-channel analysis was used. Figures 17, 18, 19, and 20 present phase data obtained in cavities with the following flow characteristics: closed without resonance, open with resonance, transitional with resonance, and closed with resonance, respectively, and are discussed in the section "Flow Field Analysis by Using Cross-Channel Analysis Between Transducers."

Available data allowed comparisons between spectra from cavities with a given  $l/h$  for two values of  $w$  (2.4 and 9.6 in.) at a constant  $h = 2.4$  in. Data are presented in figure 21 for  $FPL\left(f\frac{l}{U_\infty}\right)$  obtained in cavities with the two widths. The figure is divided into parts (a) through (l), each corresponding to a different value of  $l/h$  (4 through 17) and containing data for the range of  $M_\infty$ . These data are discussed in the section "Effect of Cavity Width."

Figure 22 contains a similar presentation of data as figure 21 but is for spectra from cavities for two and, when available, three different values of  $h$  (2.4, 1.2, and 0.6 in.) at a constant  $w = 9.6$  in.). The figure is divided into parts (a) through (l), each corresponding to a different value of  $l/h$  (2 through 15) and is discussed in the section "Effect of Cavity Depth."

Previous results obtained for subsonic and low transonic cavity flow fields (refs. 4, 10, and 11) indicate that static-pressure distributions and unsteady-pressure spectra are very sensitive to  $M_\infty$ . Figures 21 and 22 are referred to in the section "Effect of Mach Number" for discussion of effects of  $M_\infty$  on the spectra. Figure 23 presents typical observed and predicted resonant frequencies as a function of  $M_\infty$ . Experimental data are given for all four cavity configurations ( $w/h = 1, 4, 8,$  and  $16$ ) for two values of  $l/h$  (4 and 7). These data are representative of all data obtained.

In the spectra to follow, occasionally peaks that are not associated with cavity resonances occur at

frequencies that do not change with cavity length. These spectral peaks are attributed to tunnel or other hardware/flow sources and are not included in the following discussion. (For example, as is seen later, all spectra presented for  $M_\infty = 0.40$  contain peaks at approximately 170 Hz.)

Note that the dynamic range of the instrumentation was 50 dB and the choice of the decibel range for the plots was made for presentation purposes. Scales were expanded to allow comparisons of spectra with different levels: 80 dB was used in figures 12 through 15; 70 dB was used in figures 21 and 22; and 60 dB was used in figures 7 through 10. Scales were contracted to present multiple individual spectra: 40 dB was used in figures 12 through 15. Note that the limits in the scales vary in figures 12 through 15. The contracted scale represents a compromise; some data were sacrificed in order to maintain resolution. (See, for example, fig. 13(d).)

An electronic "Supplement to NASA TP-3669" containing the spectral data presented graphically in this report in ASCII format is available on request as a CD-ROM. A request form is included at the back of this report.

### Effect of Transducer Location

From the typical unsteady-pressure spectra presented in figure 7, it is apparent that both broadband levels and resonant peak amplitudes vary with transducer location. The broadband levels increase monotonically with  $x$ , whereas the peak levels do not. As described in references 8, 9, 11, and 16, peak amplitudes are expected to coincide with mode shapes that are similar to but not identical to the classical standing wave patterns observed in longitudinal box resonators. It has been demonstrated that mode shapes observed in rectangular cavities exposed to aerodynamic flow can be described by equations with the form of a ramped (increasing with  $x$ ) sinusoidal function (ref. 16), such as

$$20 \log \left[ \frac{(P'_{rms})_m}{q_\infty} \right] \Big|_{x/l} = 20 \log \left[ \frac{(P'_{rms})_m}{q_\infty} \right] \Big|_{x/l=1} - \left[ A_1 + A_2 \frac{x}{l} + A_3 \left| \cos \left( \alpha_m \frac{x}{l} \right) \right| \right]$$

Here  $m$  indicates mode number. For the case presented in figure 8 ( $w = 9.6$  in.,  $h = 2.4$  in.,  $l/h = 10$ ), this equation can be written as

$$\begin{aligned} (\text{SPL})_m \Big|_{x/l} &= (\text{SPL})_m \Big|_{x/l=1} \\ &- 10 \left[ 1 - \left| \cos \left( \pi m \frac{x}{l} \right) \right| + 1.8 \left( 1 - \frac{x}{l} \right) \right] \end{aligned}$$

For the nonresonant case, the spectra presented in figure 9 show a broadband trend that is similar to the resonant condition, except that there is a slight decrease in level measured by the two aftmost transducers on the cavity floor. This change in broadband level with cavity location is quantified in figure 10 by using OASPL. The distribution of OASPL shows a slight correspondence to the static-pressure distribution, which is seen in comparing figures 10 and 11: lower values of OASPL in the low-pressure separated region just aft of the rearward-facing step, increasing in the attachment region, remaining somewhat level in the attached region, and decreasing slightly in the vicinity of the aft separation and increasing where the flow impinges on the aft wall.

There were three reasons for choosing transducer 1 for data comparisons. First, of all the locations in the cavity, only spectra obtained on the forward and aft walls contained all the resonant peaks for all cavity lengths. (This is seen in fig. 8.) Second, of these two locations, the ratio of peak amplitude to broadband noise (signal to noise) was greater at the forward wall. (This is seen in fig. 7.) Third, of the three transducers located on the forward wall, only transducer 1 was exposed for all cavity configurations.

### Effect of Cavity $l/h$ and Correlation With Open, Transitional, and Closed Flows

For this study,  $l$  was varied from 1.2 to 42.0 in., whereas  $w$  and  $h$  were held constant to achieve values of  $w/h$  of 1, 4, 8, and 16. These four values of  $w/h$  corresponded to  $w = h = 2.4$  in.;  $w = 9.6$  in.,  $h = 2.4$  in.;  $w = 9.6$  in.,  $h = 1.2$  in.; and  $w = 9.6$  in.,  $h = 0.6$  in., respectively.

In general, the data presented in figures 12 through 15 show that as  $l/h$  increases, cavities change from being resonant to being nonresonant with their peak amplitudes decreasing gradually. This pattern is expected for a cavity changing from supporting open to a closed flow. (Some exceptions occur for which individual peak amplitudes increased for midrange values of  $l/h$  as seen in fig. 13(d) for  $l/h = 7$  and 9.) Resonant spectra are obtained largely in cavities classified as supporting open and transitional flow. (Some exceptions are observed including the lack of resonance for most cases of open flow at  $M_\infty = 0.2$  and occasional instances of resonance for closed cavity flows as seen, for instance, in fig. 13(d) for  $l/h = 10.4$ . Furthermore, an occasional instance of resonance occurs for closed flow with increased amplitude as seen in fig. 13(c) for  $l/h = 9$ .) Figure 16 provides a chart indicating the configurations and conditions that support resonance. Since the decrease in peak amplitude occurs gradually with changing  $l/h$ , identifying the exact point at which resonance no longer occurs is often difficult. For the purpose of this chart, the

spectra are considered resonant when the difference between peak and background levels is greater than 6 dB (peak pressure twice the background level). This chart indicates that for a given value of  $M_\infty$  (with the exception of  $M_\infty = 0.20$ ), cavities with larger values of  $w/h$  sustain resonances at higher values of  $l/h$ . For a given configuration, the boundary between resonant and non-resonant cases occurs at a nearly constant  $l/h$  for  $M_\infty = 0.60$  and above; this differs from the  $M_\infty$  dependence that the boundary between transitional and closed flows exhibits.

One more observation can be made from figures 12 through 15. First, the frequencies at which resonances occur decrease with increasing  $l/h$  as would be expected from the Rossiter equation. As a consequence of this, more resonant peaks are apparent in the frequency band of analysis (0–2000 Hz) for increasing  $l/h$ .

#### Flow Field Analysis Using Cross-Channel Analysis Between Transducers

The previous section, "Effect of Cavity  $l/h$  and Correlation With Open, Transitional, and Closed Flows," contained the observation that resonance could occur for transitional and closed cavity flows. Since the traditional model for cavity resonance requires the time-varying impingement of the shear layer on the aft wall for one component of the feedback loop, data indicating resonance simultaneously with shear layer impingement on the cavity floor require further examination. Cross-channel analysis for closed cavity flow without resonance and open cavity flow produced the expected results. For closed flow without resonance, no communication appears to exist between the fore and aft walls. (See fig. 17(a).) Streamwise flow is indicated along the floor by the positive slope of the phase plots in figures 17(b) and (c). Loss of the low-frequency portion of the phase in figure 17(b) is understandable because these data were obtained in the impingement region. For open flow, the negative slope above approximately 200 Hz in figure 18(a) indicates upstream feedback between the fore and aft walls. The phase data presented in figures 18(b) and (c) for transducers on the cavity floor indicate neither upstream nor downstream propagation but suggest a standing wave.

Cross-channel analysis of data for transitional and closed cavity flow with resonance produced results that were consistent with spectra analysis and mean static-pressure data; that is, separated flow throughout the interior of the cavity is not necessary for resonance to occur. This result is significant because it indicates that a separating store could experience both large pitching moments and forced vibration simultaneously. For transitional flow, upstream feedback between the fore and aft walls is also indicated in figure 19(a). Nothing can be

concluded from figures 19(b) and (c) (floor-mounted transducers); this suggests two competing phenomena or a standing wave. The loss of phase data on the floor could also indicate impinging flow. Phase data for closed flow with resonance also indicate upstream feedback between the fore and aft walls (fig. 20(a)). Data from locations along the floor, given in figures 20(b) and (c), indicate largely streamwise flow at frequencies above approximately 800 Hz.

#### Effect of Cavity Width

The cavity width was adjusted to achieve values of 2.4 and 9.6 in. at a constant  $h = 2.4$  in. Figure 21 illustrates a clear increase in resonant amplitudes when  $w$  is increased from 2.4 to 9.6 in. Further, there are cases for which increasing the cavity width induces resonance. (See fig. 21(f) for Mach numbers 0.80 through 0.95.) These results are consistent with the static-pressure results presented in reference 5, which indicate that narrower cavities tend toward closed flow where the potential for resonance is reduced. A slight increase in the reduced frequencies at which the resonant peaks occur is also observed for cavities at lower values of  $l/h$  with increasing  $w$ . This effect decreases with increasing  $l/h$ .

#### Effect of Cavity Depth

The depth of the cavity was adjusted to achieve values of 2.4, 1.2, and 0.6 in. at a constant  $w = 9.6$  in. Figure 22 shows that although the peak amplitude levels were nearly the same for the various depths, the background levels decrease with decreasing  $h$ ; this resulted, in most cases, in an increase in peak amplitude over the background level with decreasing  $h$ . A decrease in peak amplitude over background level is taken as a tendency away from resonance; this agrees with the tendency that deeper cavities show towards closed cavity flow. There were cases of clear increases in resonant amplitude (greater than that added by the decrease in background) with depth. (See fig. 22(e), for example.) A slight decrease in the reduced frequencies at which the resonant peaks occur is also observed for cavities with decreases in  $h$  at lower values of  $l/h$ . This effect also decreases with increasing  $l/h$  and becomes no longer apparent at  $l/h = 8$ .

Note that for each plot, curves corresponding to different values of  $h$  also have different associated values of  $w/h$ , due to constant  $w$ , and of  $\delta/h$ , due to constant  $\delta$  for each  $M_\infty$ . No attempt was made to separate the effects due to each of these parameters.

#### Effect of Mach Number

From static-pressure results reported in reference 5 (a cavity with  $l/h$  which supported transitional flow at high speeds tended towards closed flow at low speeds),

the expectation would be that the peak amplitudes would decrease with decreasing  $M_\infty$ . Although this is not observed in figures 21 and 22, the characteristics of the spectra did change with  $M_\infty$ . Results are similar to those reported in reference 10—although clear resonances occur for  $M_\infty = 0.80$  through 0.95, a possible destabilization of the feedback process that generates resonance is indicated for  $M_\infty = 0.60$  and 0.4. The evidence for this result includes increases in energy observed over broadening frequency bands and multiple peaks. For most cases, spectra at  $M_\infty = 0.20$  do not indicate resonance.

As apparent in figure 23, resonance occurs at slightly lower reduced frequencies for increasing  $M_\infty$ . Only small discrepancies occur between the predicted and observed values of the Rossiter frequencies which are acceptable because single values for the empirical constants  $k(M_\infty)$  and  $\alpha(l/h)$  were used in the modified Rossiter equation. As indicated in the previous two sections, small frequency shifts are associated with changes in cavity  $h$  and  $w$ .

### Concluding Remarks

In general, cavities change from resonant to nonresonant with peak amplitudes decreasing gradually as length-to-depth ratio  $l/h$  increases. Resonant spectra are obtained primarily in cavities with mean static-pressure distributions characteristic of open and transitional flow. There are cases for which resonance occurs for closed flow. Cross-channel analysis supported the presence of upstream feedback between the fore and aft walls simultaneously with streamwise flow along the floor of the cavity. Resonant frequencies decrease with increasing  $l/h$  as would be expected from the Rossiter equation.

Increasing cavity width has the effect of significantly increasing resonant amplitudes. Cases in which increasing the cavity width induced resonance were found to occur. Small shifts in resonant frequencies with changes in cavity width  $w$  (an increase in resonant frequency with an increase in  $w$ ) are observed for low values of  $l/h$ .

Decreasing cavity depth has the effect of increasing the resonant amplitudes (the peak magnitude remains the same while the background level decreases). Small shifts in resonant frequencies with changes in  $h$  (a decrease in resonant frequency with a decrease in  $h$ ) are observed for low values of  $l/h$ .

Because different effects are observed for decreasing cavity depth and increasing cavity width, both of which increase  $w/h$ , the conclusion is that neither effect observed is due to changes in  $w/h$ .

The effect of decreasing free-stream Mach number  $M_\infty$  is to broaden the cavity resonances. Shifts in

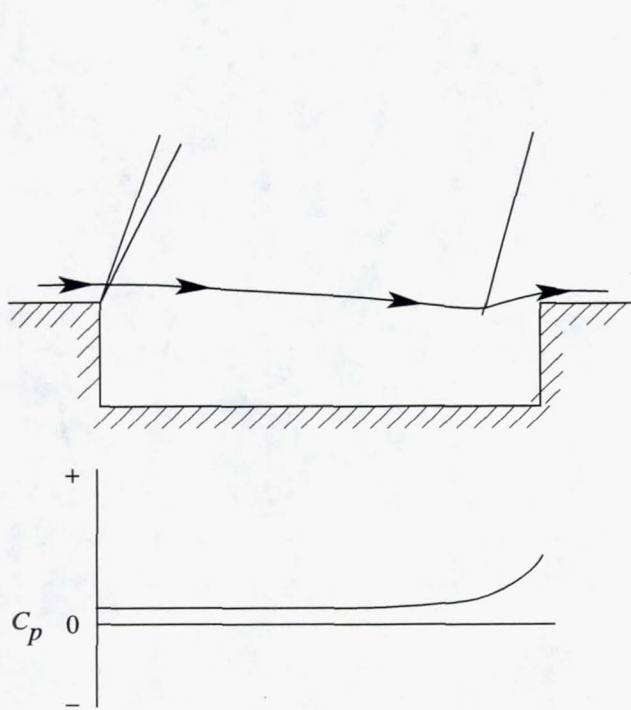
resonant frequencies with  $M_\infty$  were consistent with the Rossiter equation.

NASA Langley Research Center  
Hampton, VA 23681-2199  
August 7, 1997

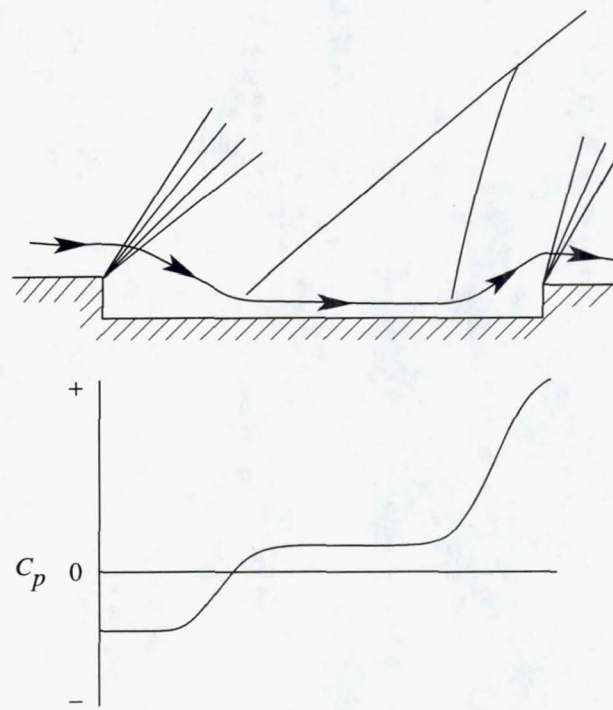
### References

1. Charwat, A. F.; Roos, J. N.; Dewey, F. C., Jr.; and Hitz, J. A.: An Investigation of Separated Flows—Part I: The Pressure Field. *J. Aerosp. Sci.*, vol. 28, no. 6, June 1961, pp. 457–470.
2. Stallings, Robert L., Jr.; and Wilcox, Floyd J., Jr.: *Experimental Cavity Pressure Distributions at Supersonic Speeds*. NASA TP-2683, 1987.
3. Plentovich, E. B.: *Three-Dimensional Cavity Flow Fields at Subsonic and Transonic Speeds*. NASA TM-4209, 1990.
4. Plentovich, E. B.; Chu, Julio; and Tracy, M. B.: *Effects of Yaw Angle and Reynolds Number on Rectangular-Box Cavities at Subsonic and Transonic Speeds*. NASA TP-3099, 1991.
5. Plentovich, E. B.; Stallings, Robert L., Jr.; and Tracy, M. B.: *Experimental Cavity Pressure Measurements at Subsonic and Transonic Speeds—Static-Pressure Results*. NASA TP-3358, 1993.
6. Rossiter, J. E.: *Wind-Tunnel Experiments on the Flow Over Rectangular Cavities at Subsonic and Transonic Speeds*. R. & M. No. 3438, British A.R.C., 1966.
7. Kaufman, Louis G., II; Maciulaitis, Algirdas; and Clark, Rodney L.: *Mach 0.6 to 3.0 Flows Over Rectangular Cavities*. AFWAL-TR-82-3112, U.S. Air Force, May 1983. (Available from DTIC as AD A134 579.)
8. Heller, H. H.; Holmes, D. G.; and Covert, E. E.: Flow-Induced Pressure Oscillations in Shallow Cavities. *J. Sound & Vib.*, vol. 18, Oct. 1971, pp. 545–553.
9. Heller, H. H.; and Bliss, D. B.: *Aerodynamically Induced Pressure Oscillations in Cavities—Physical Mechanisms and Suppression Concepts*. AFFDL-TR-74-133, U.S. Air Force, Feb. 1975. (Available from DTIC as AD B002 701L.)
10. Tracy, M. B.; Plentovich, E. B.; and Chu, Julio: *Measurements of Fluctuating Pressure in a Rectangular Cavity in Transonic Flow at High Reynolds Numbers*. NASA TM-4363, 1992.
11. Tracy, M. B.; and Plentovich, E. B.: *Characterization of Cavity Flow Fields Using Pressure Data Obtained in the Langley 0.3-Meter Transonic Cryogenic Tunnel*. NASA TM-4436, 1993.
12. Bartel, H. W.; and McAvoy, J. M.: *Cavity Oscillation in Cruise Missile Carrier Aircraft*. AFWAL-TR-81-3036, U.S. Air Force, June 1981. (Available from DTIC as AD A108 610.)
13. Shaw, Leonard; Clark, Rodney; and Talmadge, Dick: F-111 Generic Weapons Bay Acoustic Environment. AIAA-87-0168, Jan. 1987.
14. Shaw, Leonard L.: *Supersonic Flow Induced Cavity Acoustics*. AFWAL-TM-85-210-FIBG, U.S. Air Force, Dec. 1985.

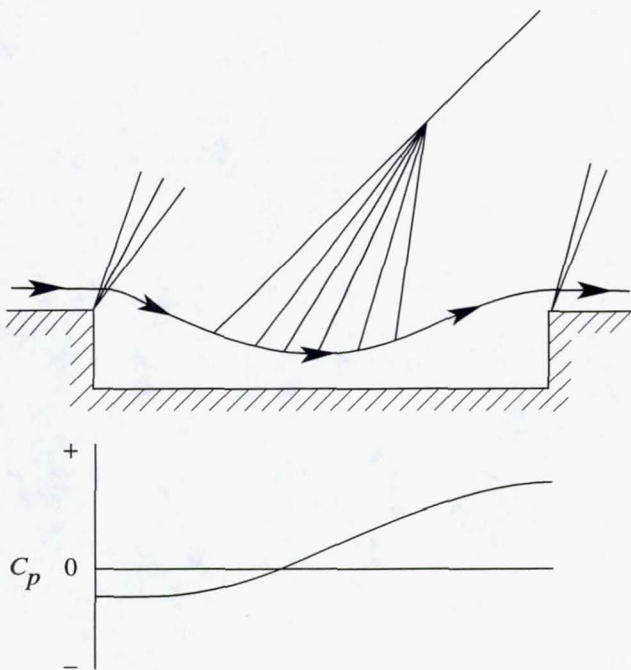
15. Rockwell, D.; and Naudascher, E.: Review—Self-Sustaining Oscillations of Flow Past Cavities. *ASME Trans., J. Fluids Eng.*, vol. 100, June 1978, pp. 152–165.
16. Smith, D. L.; and Shaw, L. L.: *Prediction of the Pressure Oscillations in Cavities Exposed to Aerodynamic Flow*. AFFDL-TR-75-34, U.S. Air Force, Oct. 1975. (Available from DTIC as AD A018 518.)
17. Komerath, N. M.; Ahuja, K. K.; and Chambers, F. W.: Prediction and Measurement of Flows Over Cavities—A Survey. AIAA-87-0166, Jan. 1987.
18. Dix, Richard E.: *On Simulation Techniques for the Separation of Stores From Internal Installations*. SAE Tech. Paper Ser. 871799, Oct. 1987.
19. Dix, R. E.; and Dobson, T. W., Jr.: *Database for Internal Store Carriage and Jettison*, Volumes 1 and 2. AEDC-TR-90-23, Arnold Eng. Develop. Center, Nov. 1990. (Available from DTIC as AD B150 543L and B151 037L.)
20. Wilcox, Floyd J., Jr.: Experimental Measurements of Internal Store Separation Characteristics at Supersonic Speeds. *Store Carriage, Integration, and Release*, R. Aeronaut. Soc., Apr. 1990, pp. 5.1–5.16.
21. Stallings, Robert L., Jr.; and Forrest, Dana K.: *Separation Characteristics of Internally Carried Stores at Supersonic Speeds*. NASA TP-2993, 1990.
22. Stallings, Robert L., Jr.; and Wilcox, Floyd J., Jr.: *Measurements of Forces, Moments, and Pressures on a Generic Store Separating From a Box Cavity at Supersonic Speeds*. NASA TP-3110, 1991.
23. Stallings, Robert L., Jr.; Plentovich, E. B.; Tracy, M. B.; and Hensch, Michael J.: *Measurements of Store Forces and Moments and Cavity Pressures for a Generic Store in and Near a Box Cavity at Subsonic and Transonic Speeds*. NASA TM-4611, 1995.
24. Block, P. J. W.: *Noise Response of Cavities of Varying Dimensions at Subsonic Speeds*. NASA TN D-8351, 1976.
25. Block, P. J. W.; and Heller, H.: *Measurements of Farfield Sound Generation From a Flow-Excited Cavity*. NASA TM X-3292, 1975.
26. Block, P. J. W.; Stallings, Robert L., Jr.; and Blair, A. B., Jr.: *Effect of Doors on Fluctuating Pressure Measurements Inside a Shallow Cavity in Supersonic Flow*. NASA TP-2849, 1988.
27. Scheiman, J.: *Acoustic Measurements of a Large Cavity in a Wind Tunnel*. NASA TM-78658, 1978.
28. Ahuja, K. K.; and Mendoza, J.: *Effects of Cavity Dimensions, Boundary Layer, and Temperature on Cavity Noise With Emphasis on Benchmark Data To Validate Computational Aeroacoustic Codes*. NASA CR-4653, 1995.
29. Tracy, Maureen B.; and Stallings, Robert L., Jr.: *Coupling of Acoustic Environment in Rectangular Cavity With Store Vibration Characteristics During Simulated Separation in Supersonic Flow*. NASA TP-2986, 1990.
30. Baysal, O.; Srinivasan, S.; and Stallings, R. L.: Unsteady Viscous Calculations of Supersonic Flows Past Deep and Shallow Three-Dimensional Cavities. AIAA-88-0101, Jan. 1988.
31. Catalano, G. D.; and Shih, C.: Turbulent Flow Over a Rectangular Cavity. *Proceedings of the Third International Conference—Numerical Methods in Laminar and Turbulent Flow*. Pineride Press, 1983, pp. 641–655.
32. Om, D.: Navier-Stokes Simulation for Flow Past an Open Cavity. AIAA-86-2628, Oct. 1986.
33. Baysal, O.; and Stallings, R. L., Jr.: Computational and Experimental Investigation of Cavity Flowfields. AIAA-87-0114, Jan. 1987.
34. Suhs, N. E.: Computations of Three-Dimensional Cavity Flow at Subsonic and Supersonic Mach Numbers. AIAA-87-1208, June 1987.
35. Srinivasan, S.; Baysal, O.; and Plentovich, E. B.: Navier-Stokes Calculations of Transonic Flows Past Open and Transitional Cavities. *Advances and Applications in Computational Fluid Dynamics Symposium*, O. Baysal, ed., FED. Vol. 66, ASME, 1988, pp. 169–179.
36. Hardin, Jay C.; and Mason, Jean P.: Broadband Noise Generation by a Vortex Model of Cavity Flow. *AIAA J.*, vol. 15, no. 5, May 1977, pp. 632–637.
37. Hardin, J. C.; and Pope, D. S.: Sound Generation by a Stenosis in a Pipe. *AIAA J.*, vol. 30, no. 2, Feb. 1992, pp. 312–317.
38. Hardin, Jay C.; and Pope, D. Stuart: Sound Generation by Flow Over a Two-Dimensional Cavity. AIAA-93-4327, Oct. 1993.
39. Dix, R. E.; and Bauer, R. C.: Engineering Model Predictions of Aeroacoustic Amplitudes in a Weapons Cavity. AIAA-93-0858, Jan. 1993.
40. Shaw, L. L.; and Shimovetz, R. M.: Weapons Bay Acoustic Environment. *Impact of Acoustic Loads on Aircraft Structures*, AGARD-CP-549, Sept. 1994.
41. Braslow, Albert L.; Hicks, Raymond M.; and Harris, Roy V., Jr.: *Use of Grit-Type Boundary-Layer-Transition Trips on Wind-Tunnel Models*. NASA TN D-3579, 1966.
42. Braslow, Albert L.; and Knox, Eugene C.: *Simplified Method for Determination of Critical Height of Distributed Roughness Particles for Boundary-Layer Transition at Mach Numbers From 0 to 5*. NACA TN 4363, 1958.
43. Adcock, Jerry B.; Peterson, John B., Jr.; and McRee, Donald I.: *Experimental Investigation of a Turbulent Boundary Layer at Mach 6, High Reynolds Numbers, and Zero Heat Transfer*. NASA TN D-2907, 1965.
44. Bendat, Julius S.; and Piersol, Allan G.: *Random Data—Analysis and Measurement Procedures*. John Wiley & Sons, 1986.
45. Bendat, Julius S.; and Piersol, Allan G.: *Engineering Applications of Correlation and Spectral Analysis*. John Wiley & Sons, 1980.



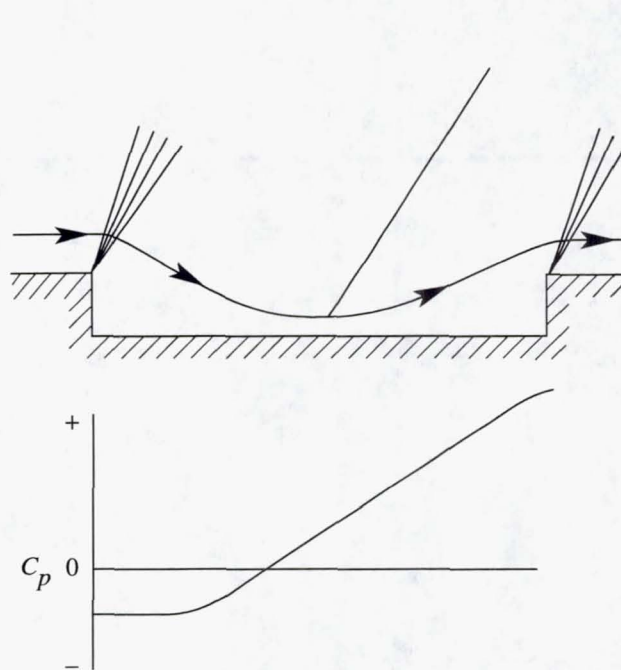
(a) Open cavity flow.



(b) Closed cavity flow.



(c) Transitional-open cavity flow.



(d) Transitional-closed cavity flow.

Figure 1. Flow field models and associated pressure distributions for supersonic speeds (ref. 20).

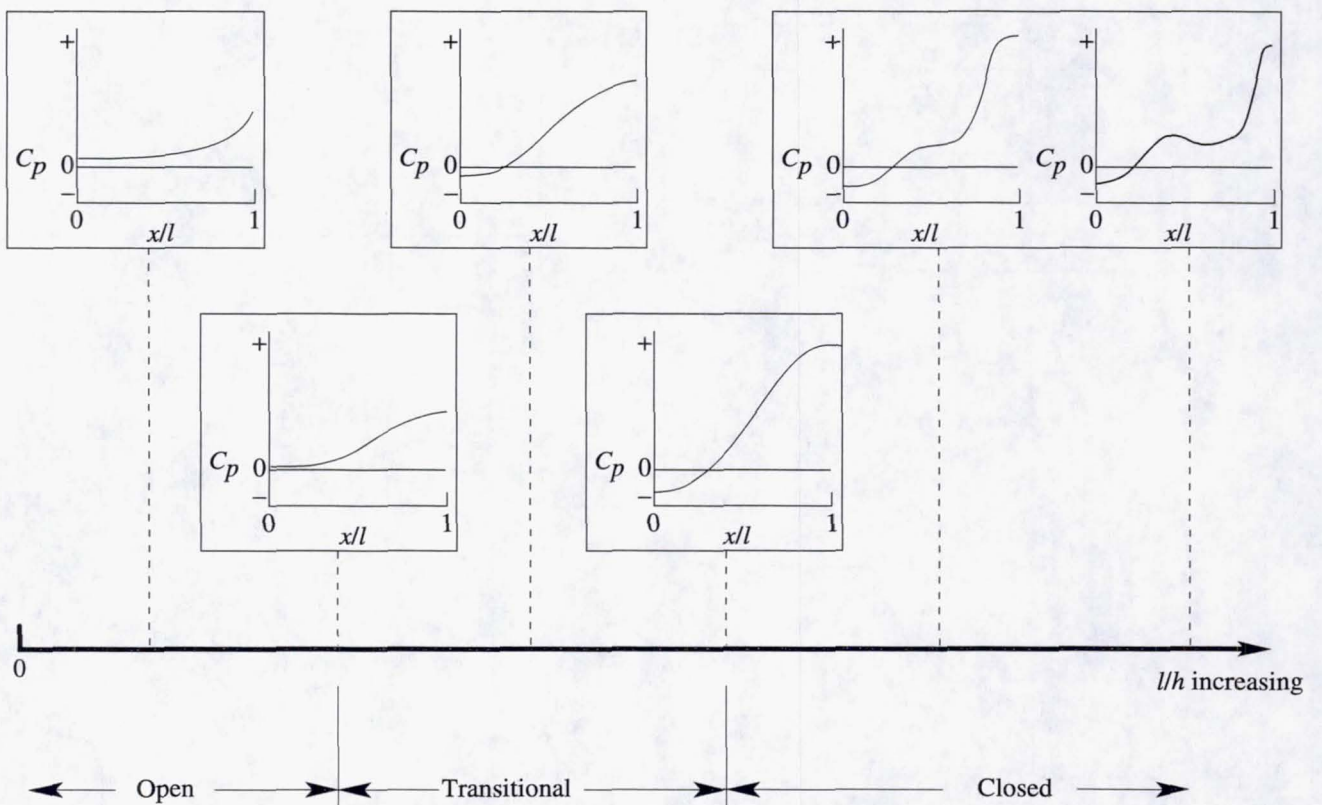
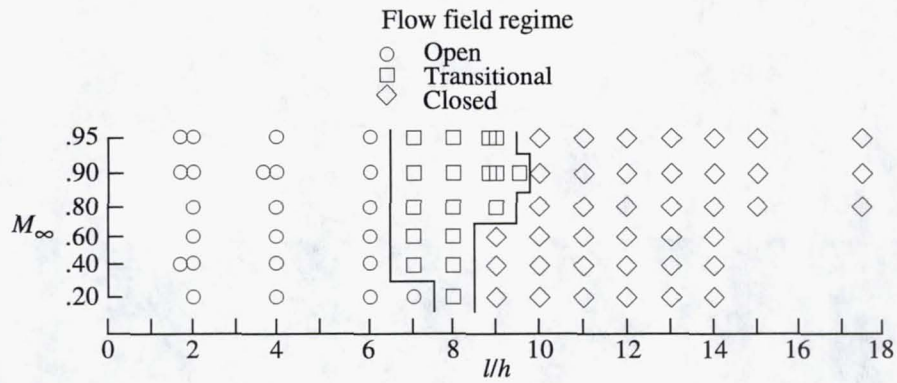
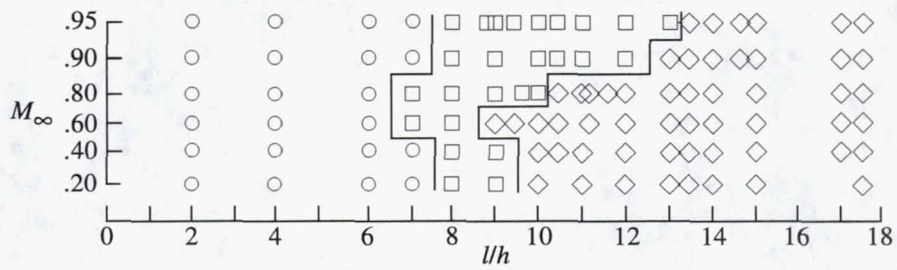


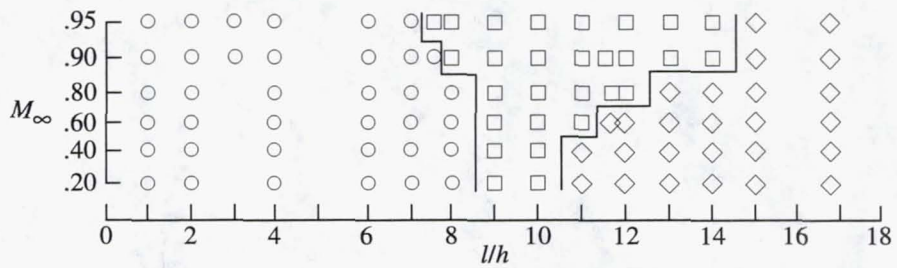
Figure 2. Representative cavity floor pressure distributions for cavity flow field types at subsonic and transonic speeds (ref. 5).



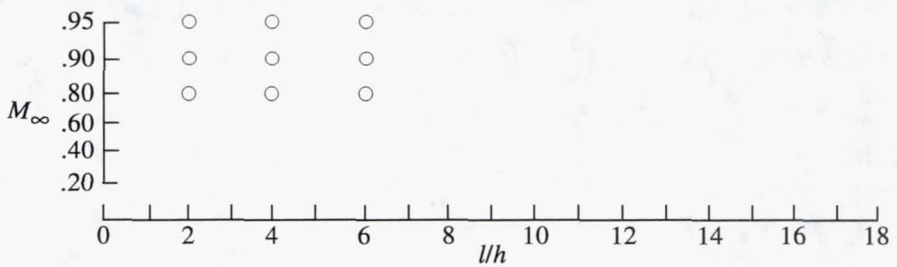
(a)  $w = 2.4$  in.;  $h = 2.4$  in.



(b)  $w = 9.6$  in.;  $h = 2.4$  in.

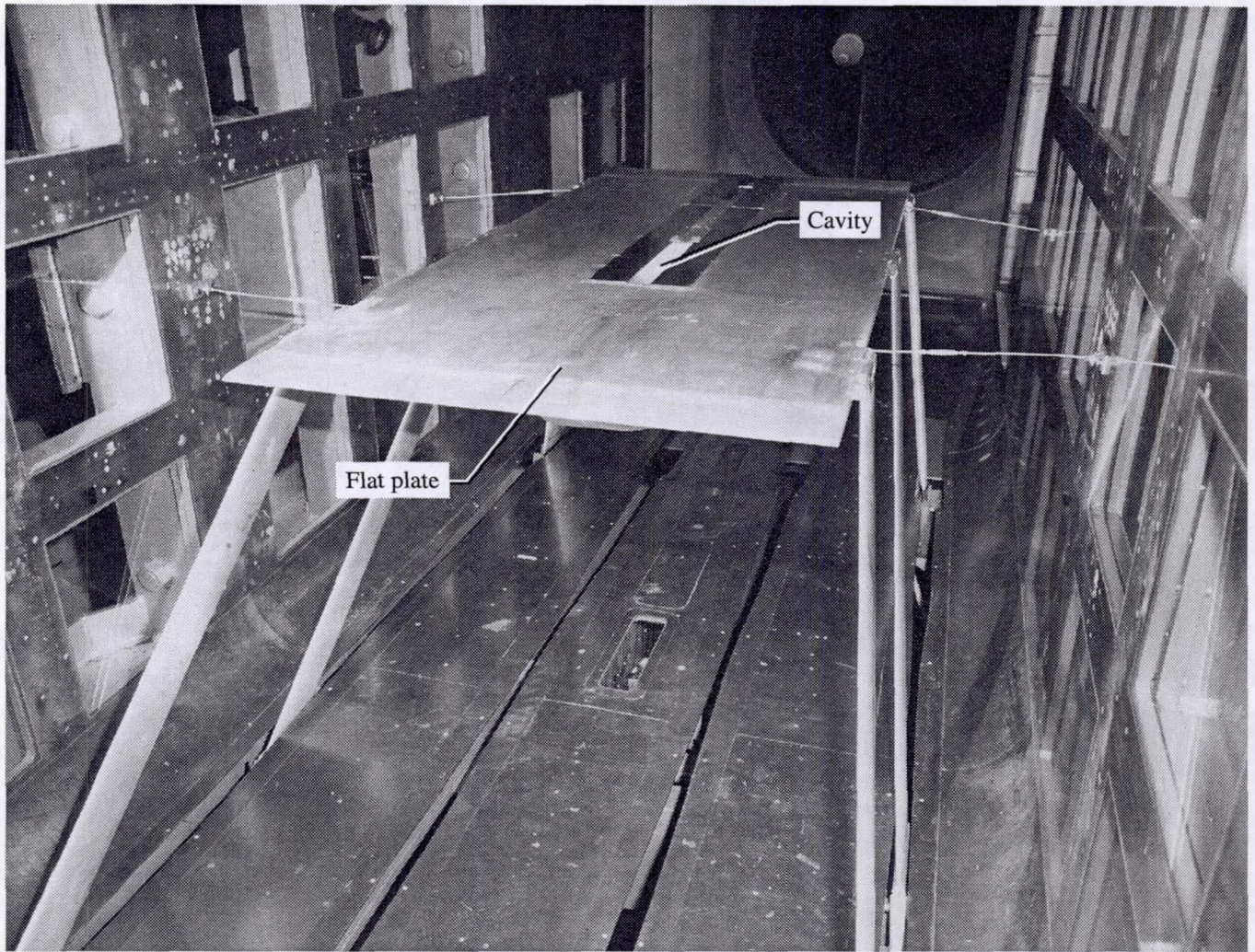


(c)  $w = 9.6$  in.;  $h = 1.2$  in.



(d)  $w = 9.6$  in.;  $h = 0.6$  in.

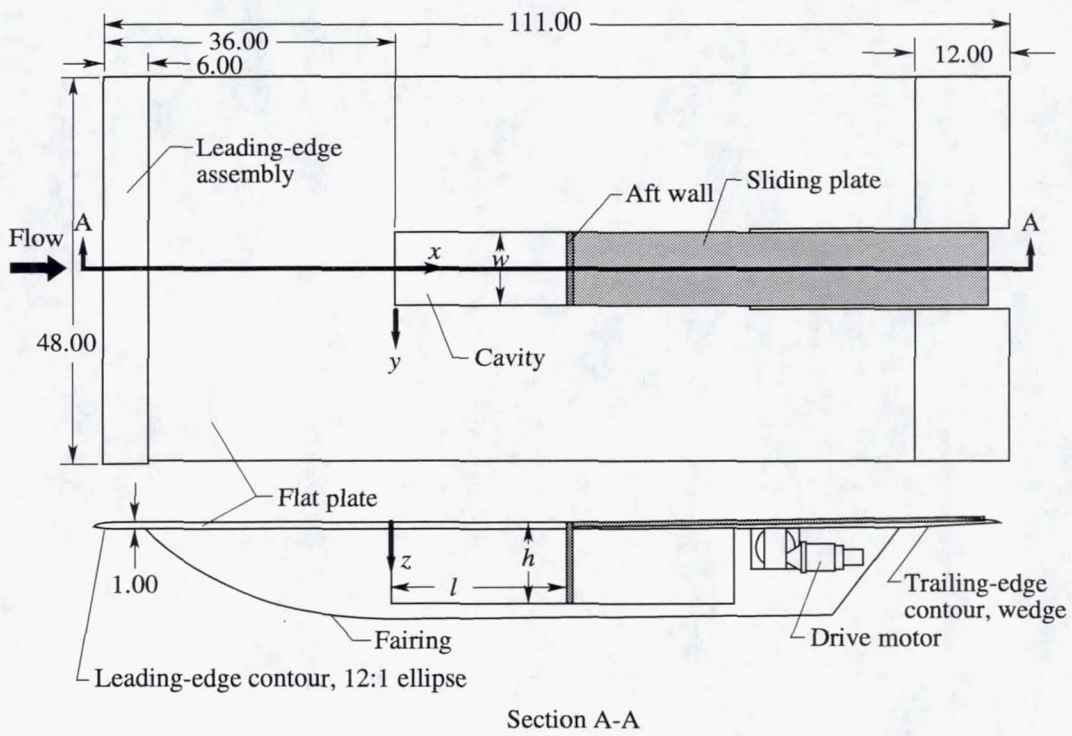
Figure 3. Boundaries of cavity flow regimes for range of cavity variables and free-stream Mach numbers (ref. 5).



L-91-02270

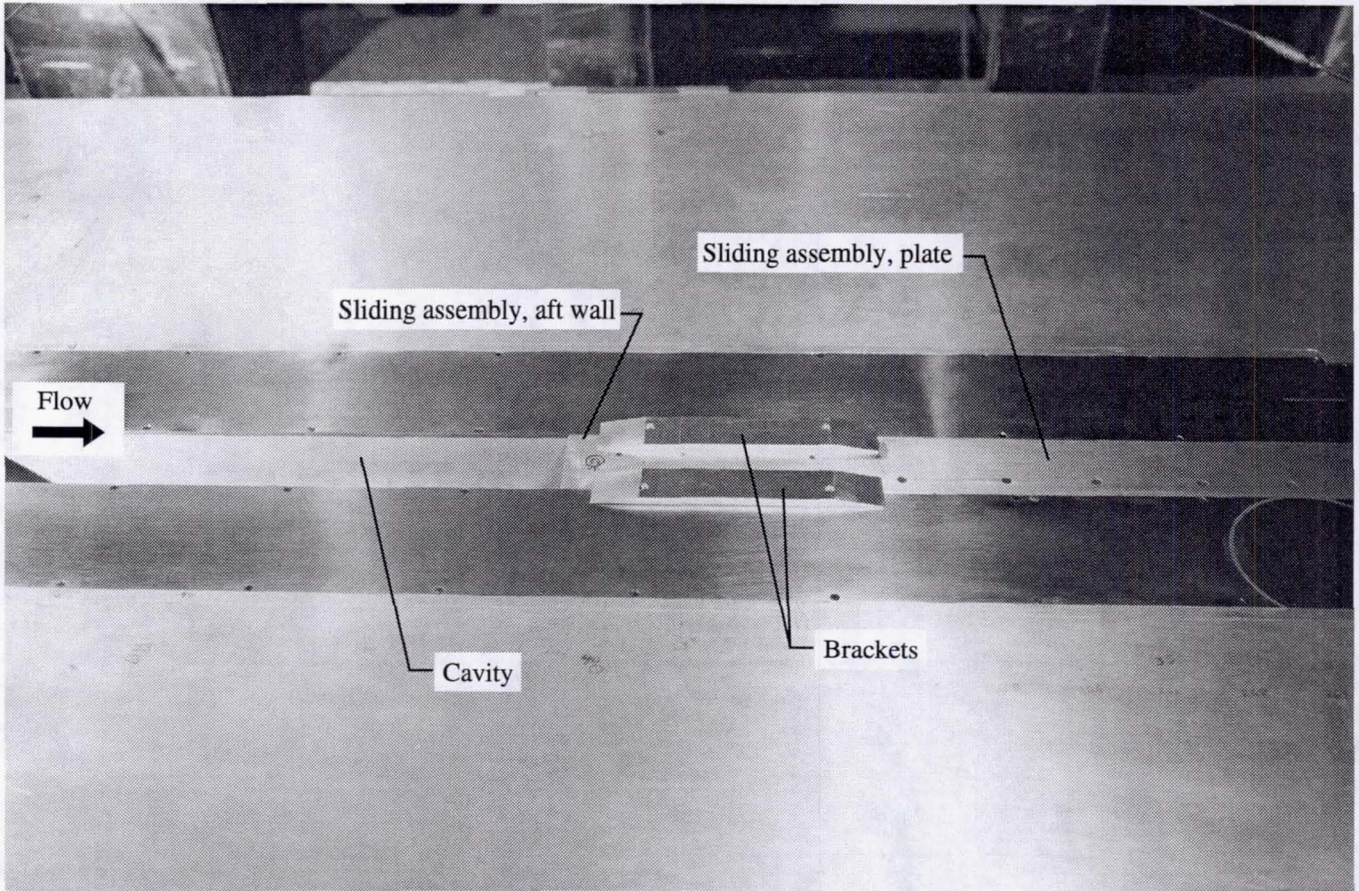
(a) Downstream view of model installed in Langley 8-Foot Transonic Pressure Tunnel.

Figure 4. Variable cavity model.



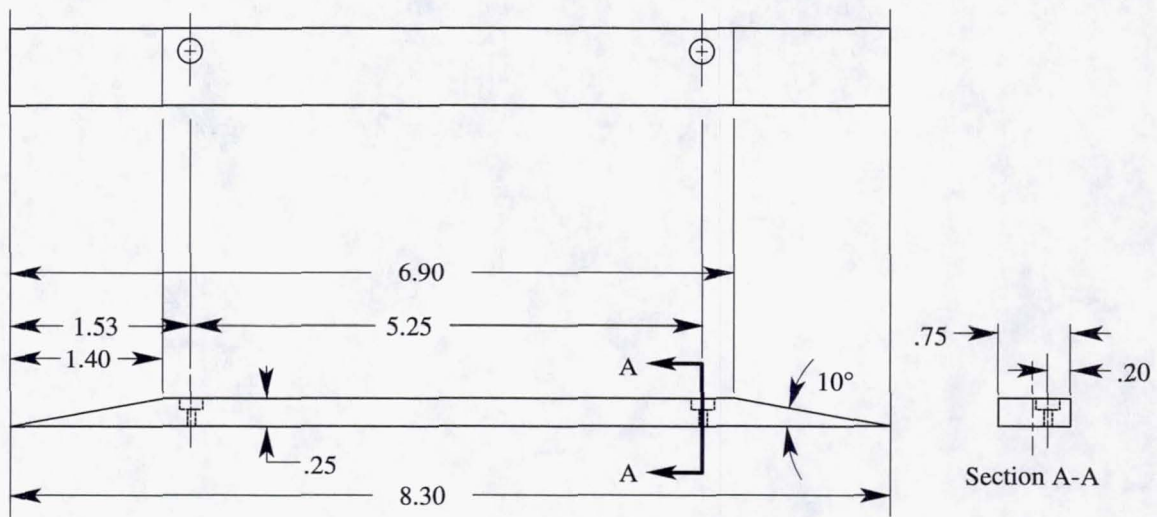
(b) Sketch of variable cavity model. Linear dimensions are in inches.

Figure 4. Concluded.



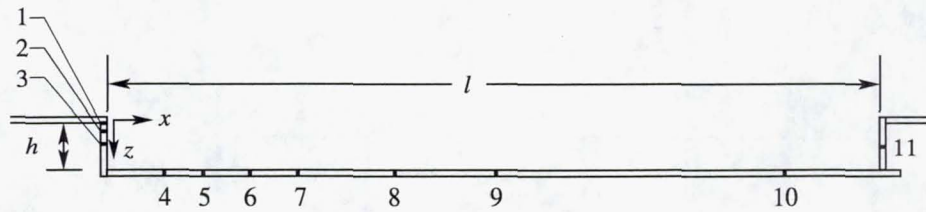
L-91-02271

(a) Photograph of brackets installed with sliding assembly.



(b) Sketch. Linear dimensions are in inches.

Figure 5. Brackets.



Transducer	x, in.	y, in.	z, in.	Model location	Reference x, in.	Reference y, in.	Reference z, in.
1	0.00	0.00	0.3	Forward wall	2.00	2.40	$h$
2	0.00	0.00	0.6	Forward wall	2.00	2.40	$h$
3	0.00	0.00	1.2	Forward wall	2.00	2.40	$h$
4	2.64	0.00	$h$	Floor	2.00	2.40	$h$
5	5.28	0.00	$h$	Floor	2.00	2.40	$h$
6	7.92	0.00	$h$	Floor	2.00	2.40	$h$
7	10.56	0.00	$h$	Floor	2.00	2.40	$h$
8	15.72	0.00	$h$	Floor	2.00	2.40	$h$
9	21.00	0.00	$h$	Floor	2.00	2.40	$h$
10	36.56	0.00	$h$	Floor	2.00	2.40	$h$
11	$l$	0.00	$h/2$	Aft wall	$l$	0.00	$0.63h-0.74h$

Figure 6. Transducer locations.

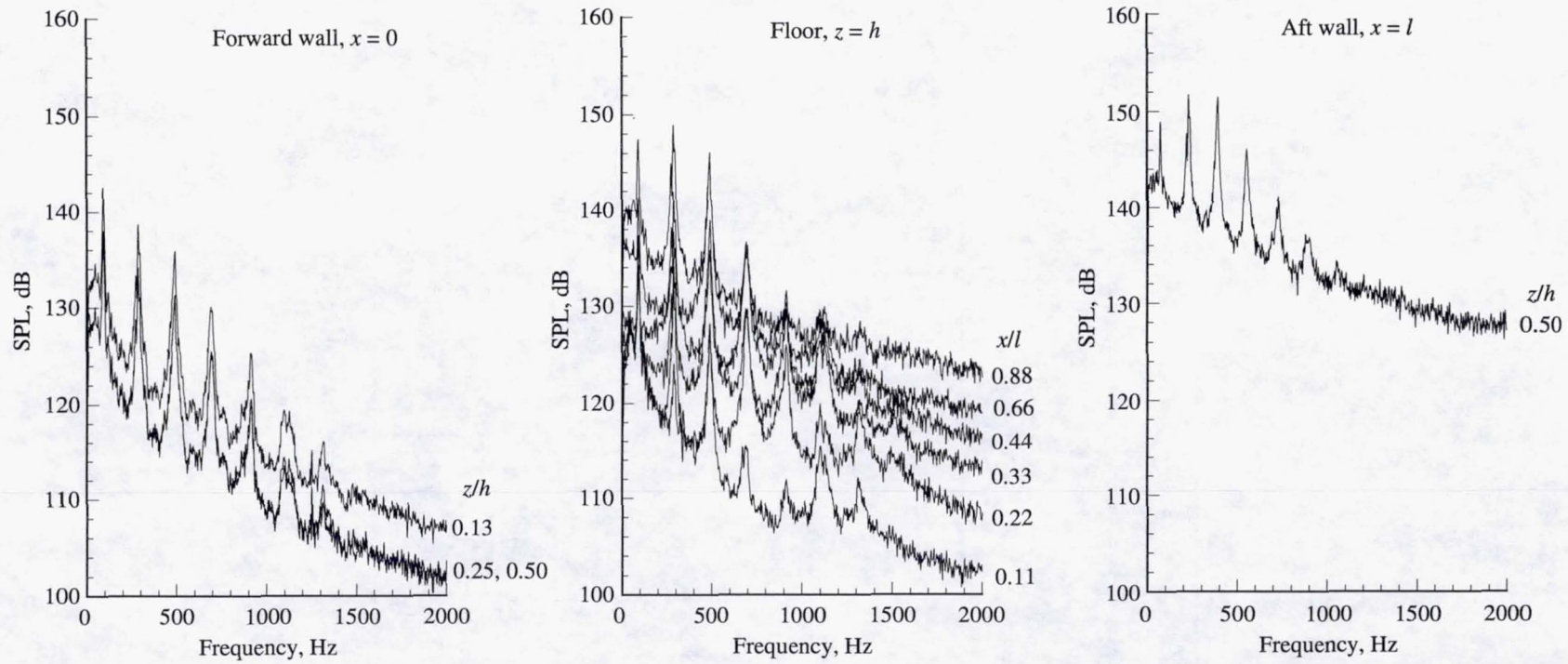


Figure 7. Effect of transducer location on unsteady-pressure spectra for  $M_\infty = 0.90$ ,  $w = 9.6$  in.,  $h = 2.4$  in., and  $l/h = 10$ .

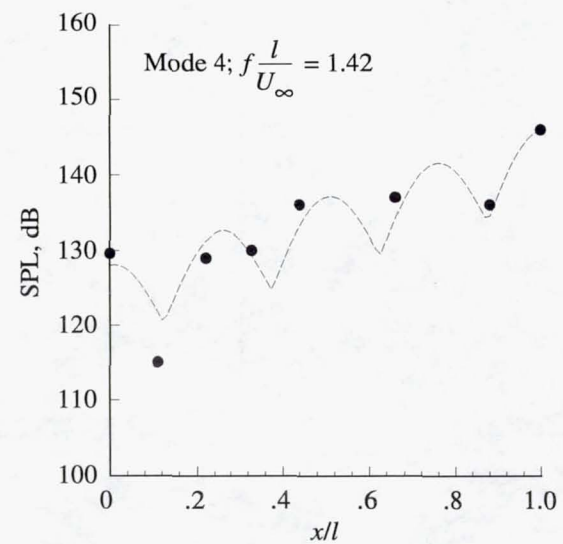
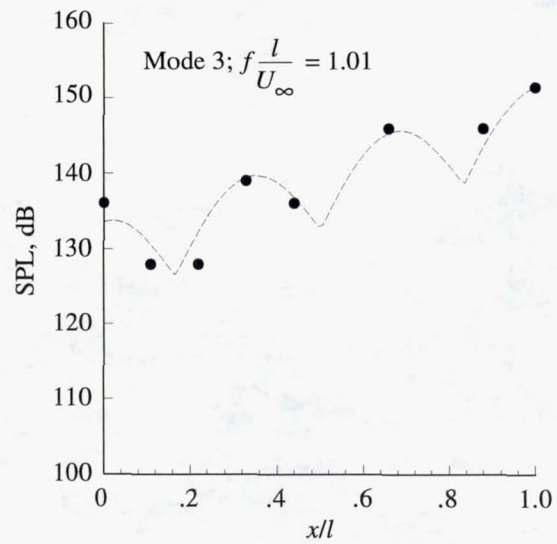
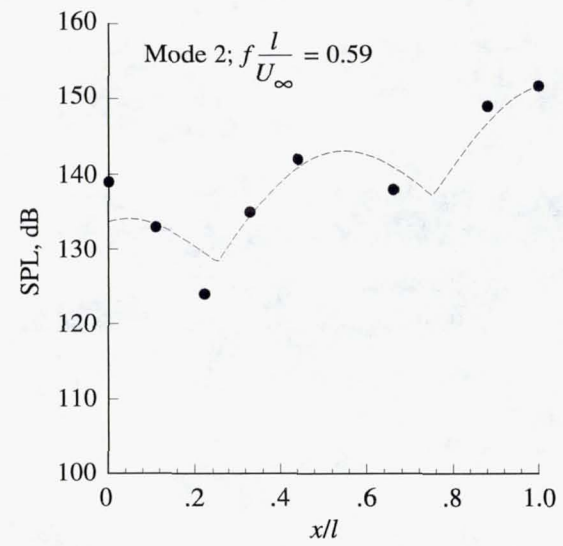
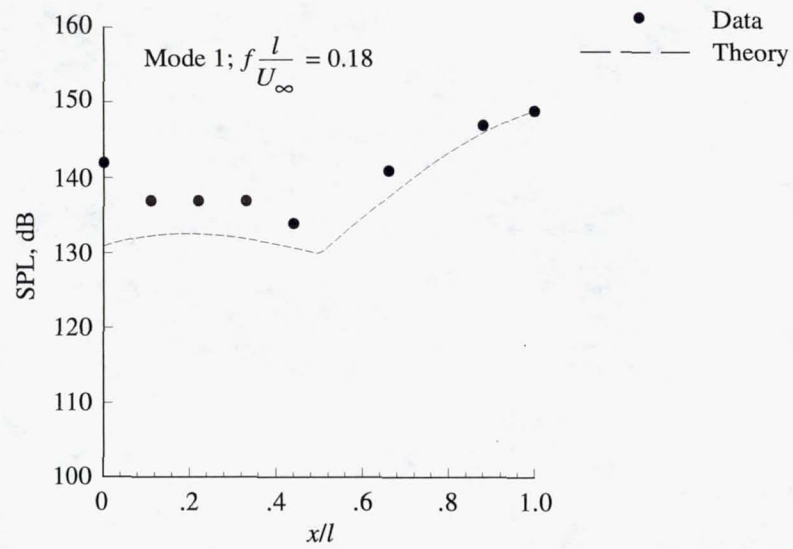


Figure 8. Peak amplitudes measured along length of cavity for  $M_\infty = 0.90$ ,  $w = 9.6$  in.,  $h = 2.4$  in., and  $l/h = 10$ .

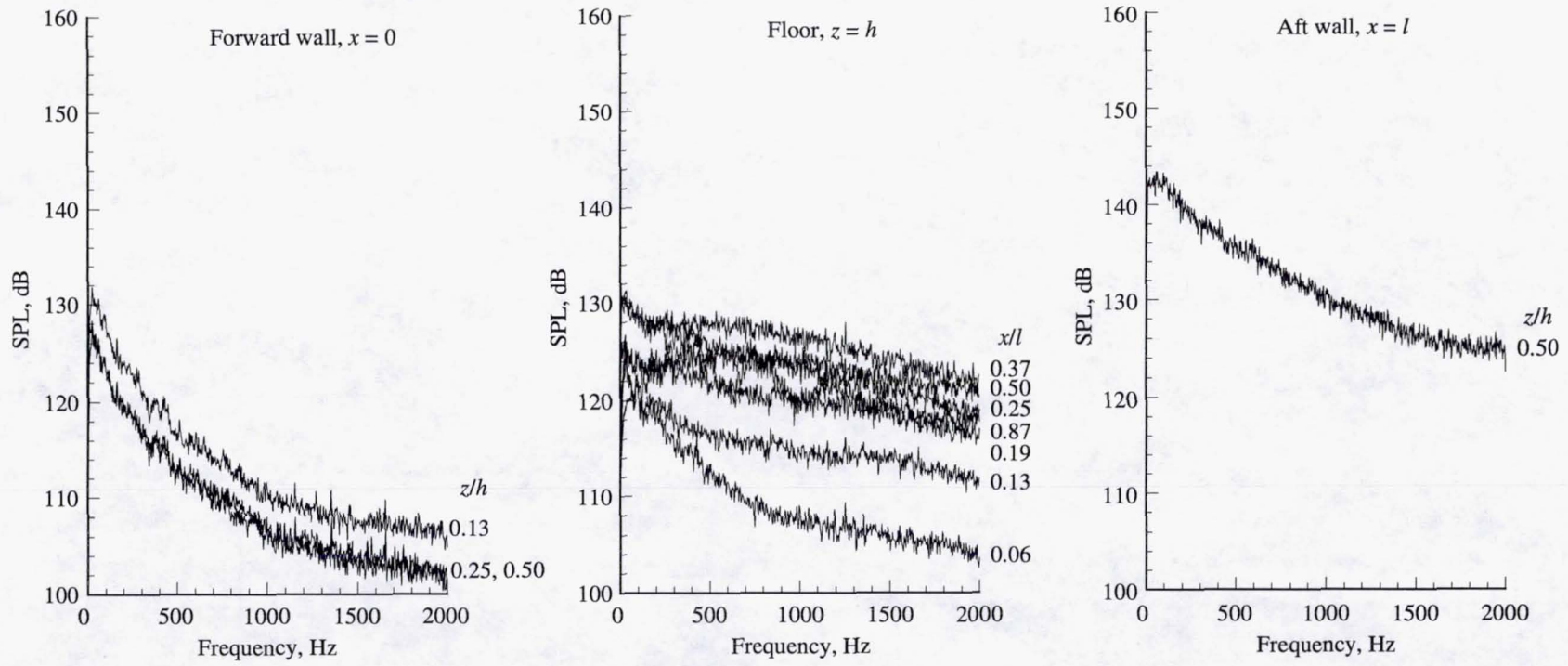


Figure 9. Effect of transducer location on unsteady-pressure spectra for  $M_\infty = 0.90$ ,  $w = 9.6$  in.,  $h = 2.4$  in., and  $l/h = 17.5$ .

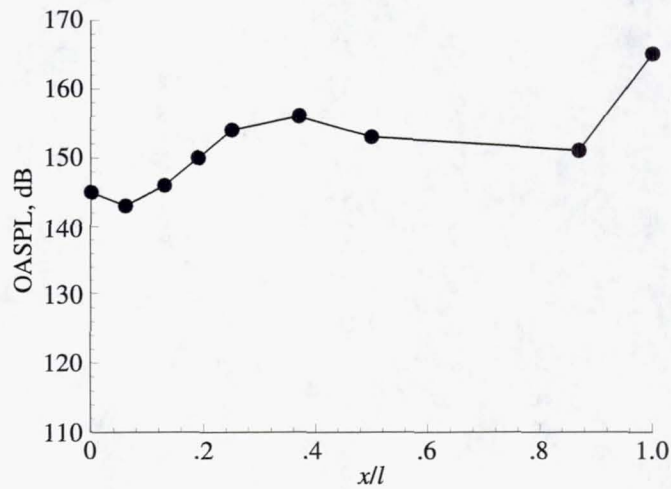


Figure 10. OASPL measured along length of cavity for  $M_\infty = 0.90$ ,  $w = 9.6$  in.,  $h = 2.4$  in., and  $l/h = 17.5$ .

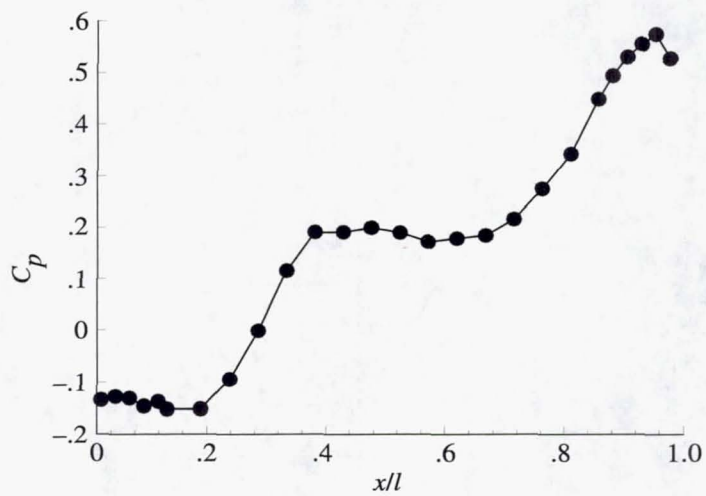
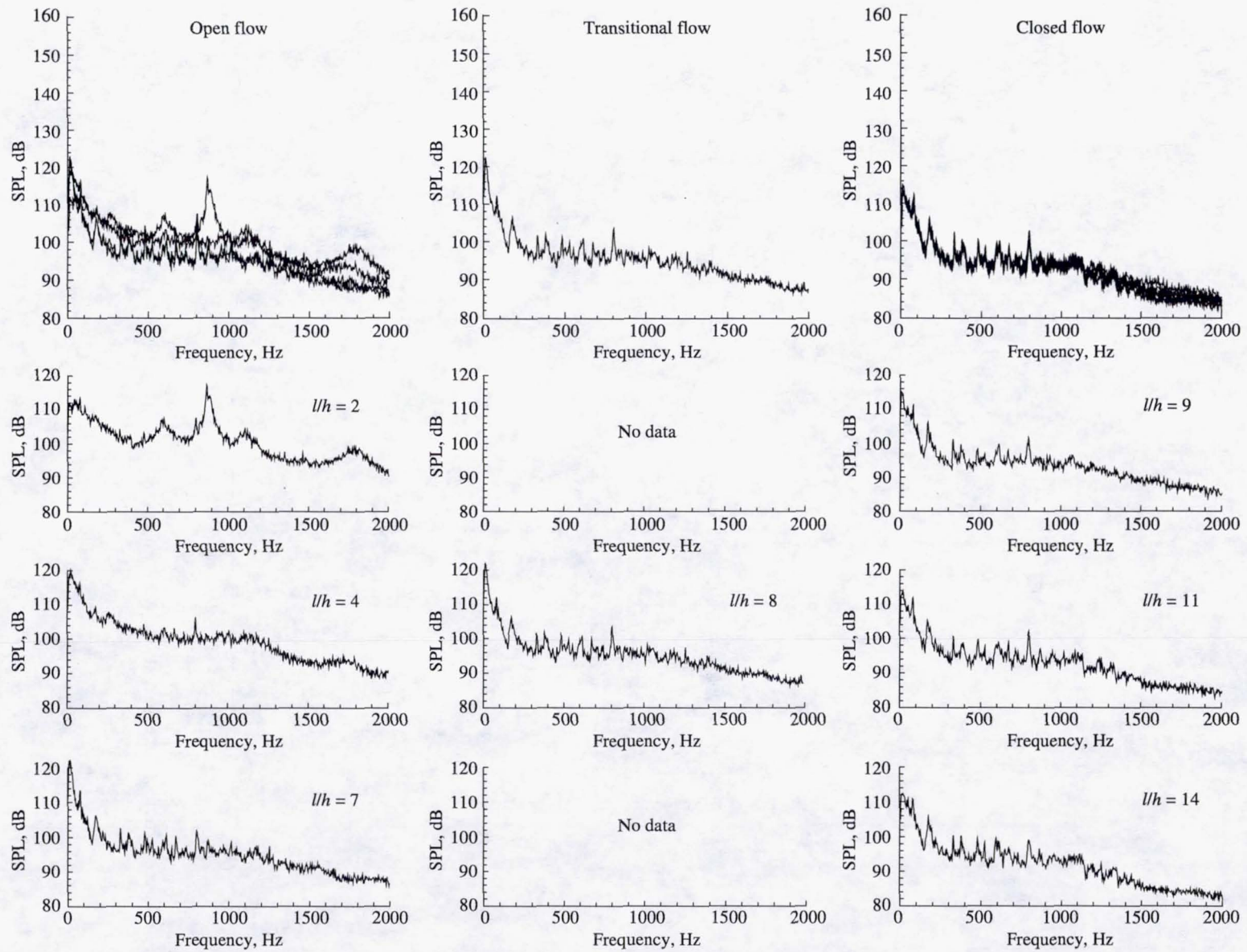
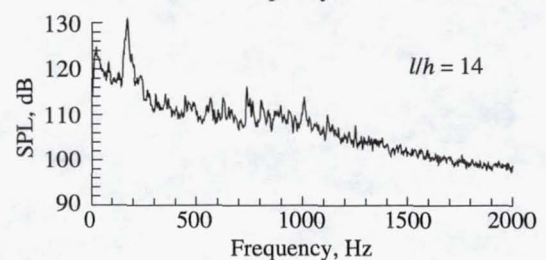
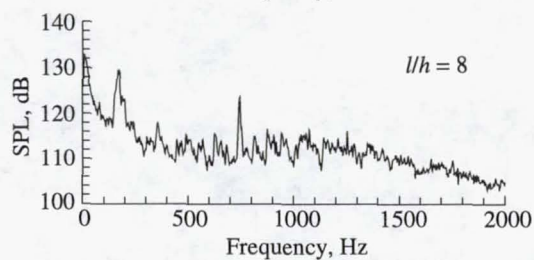
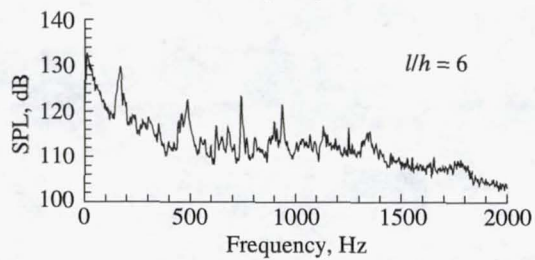
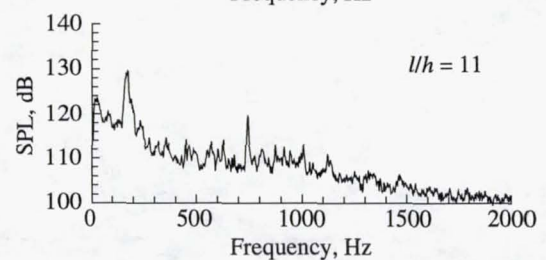
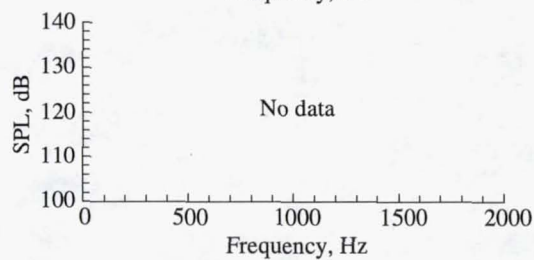
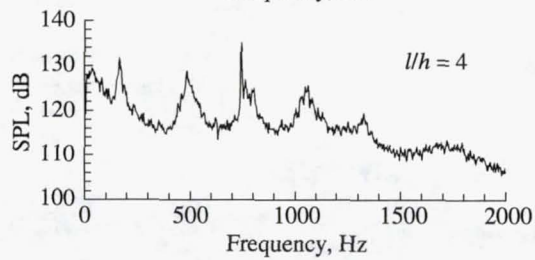
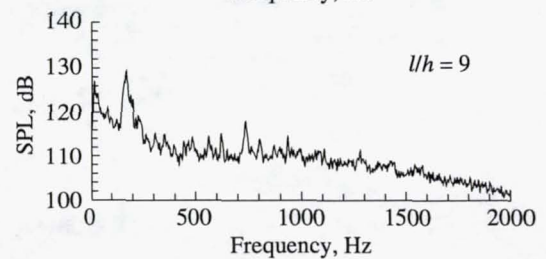
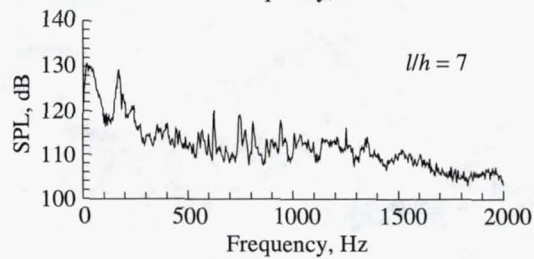
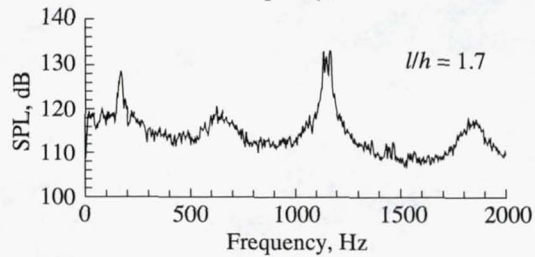
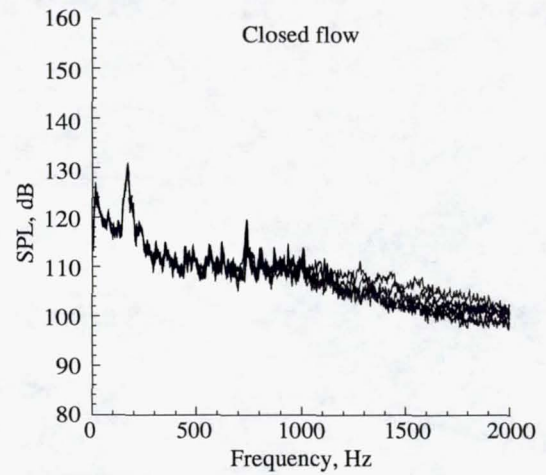
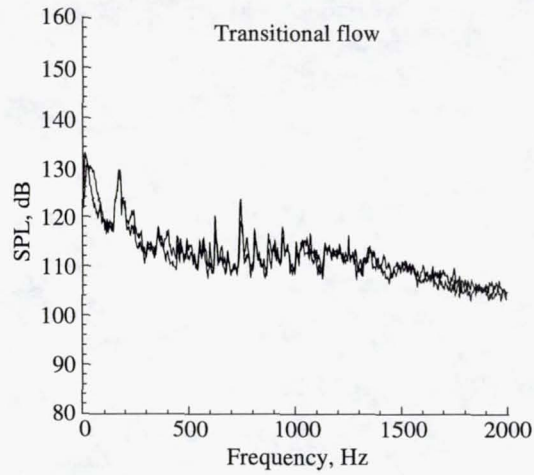
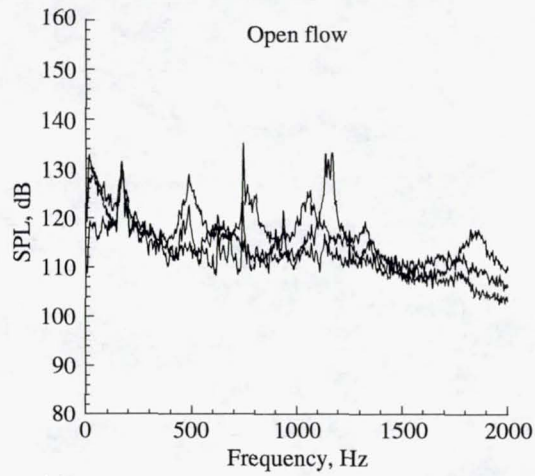


Figure 11. Pressure coefficient measured along length of cavity for  $M_\infty = 0.90$ ,  $w = 9.6$  in.,  $h = 2.4$  in., and  $l/h = 17.5$  (ref. 5).

(a)  $M_\infty = 0.20$ .Figure 12. Effect of cavity  $l/h$  on unsteady-pressure spectra from transducer 1 for  $w = 2.4$  in. and  $h = 2.4$  in.



(b)  $M_\infty = 0.40$ .

Figure 12. Continued.

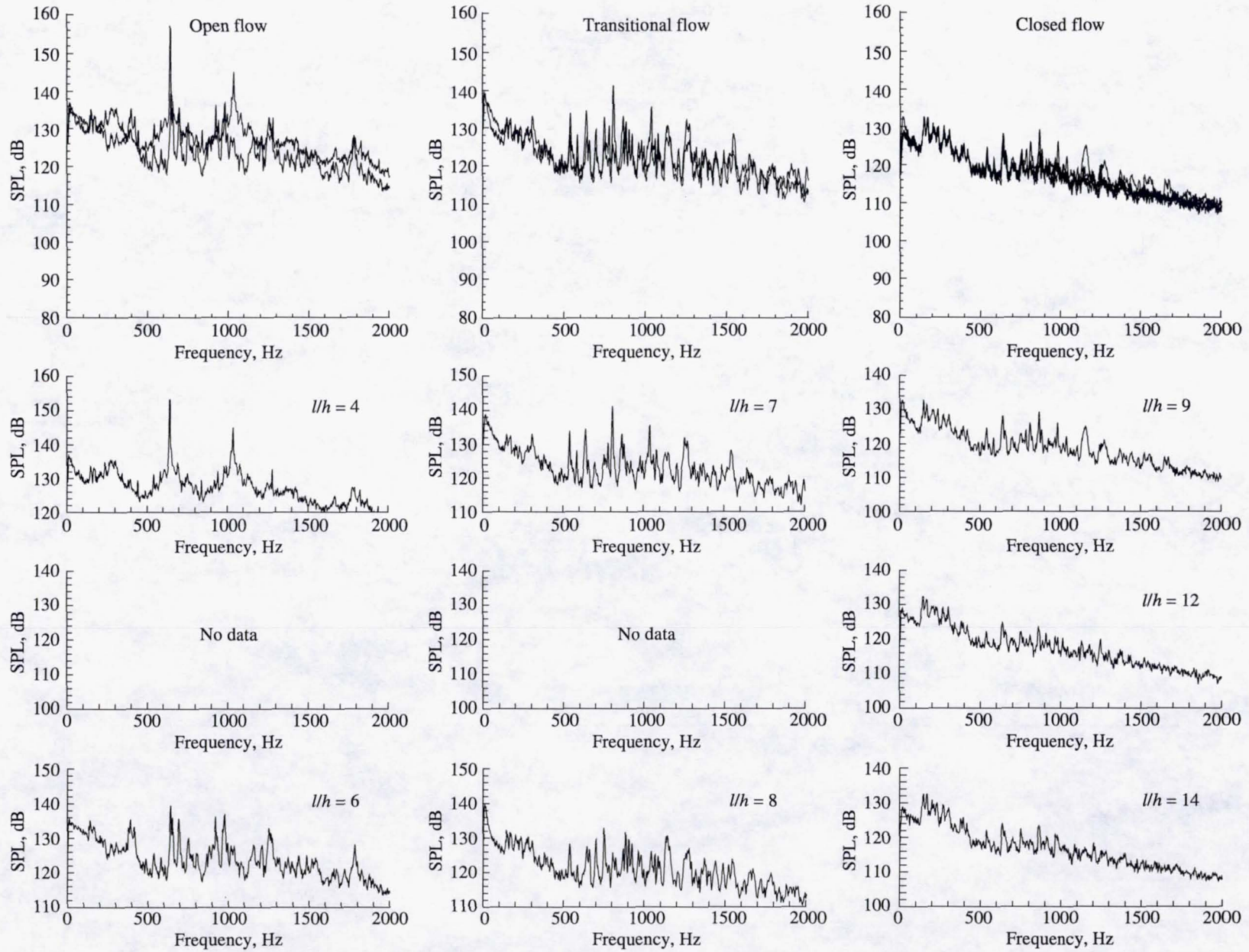
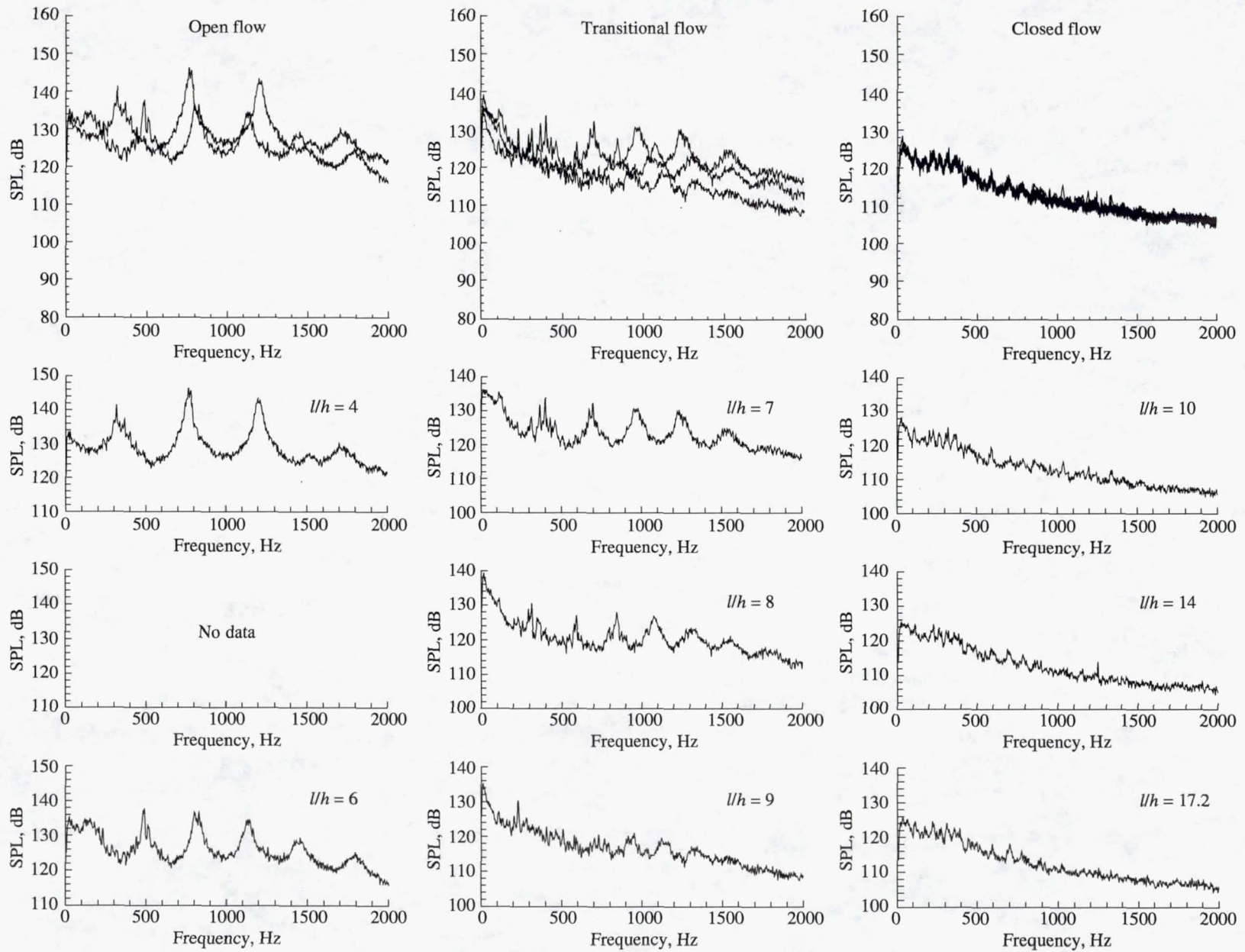
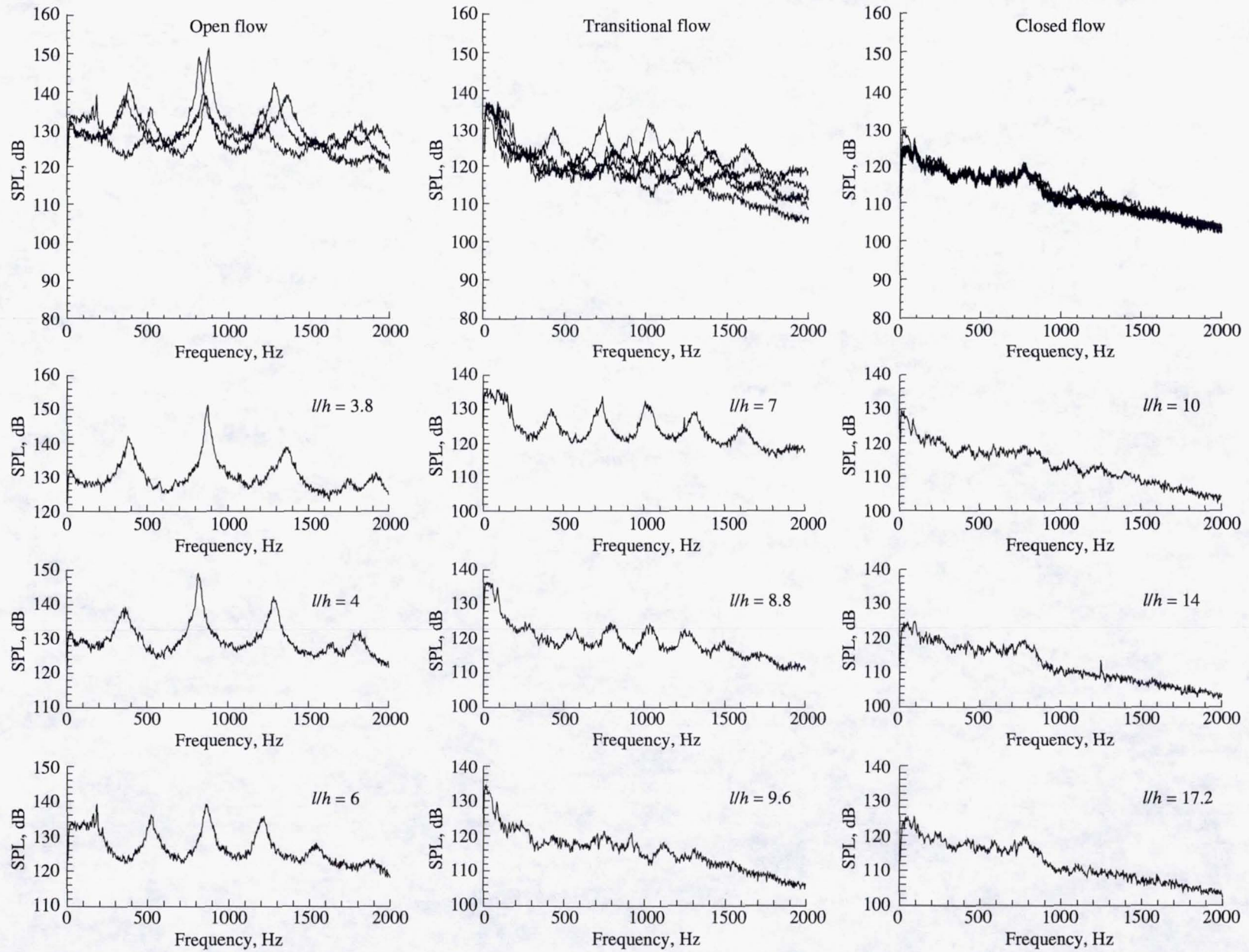
(c)  $M_\infty = 0.60$ .

Figure 12. Continued.



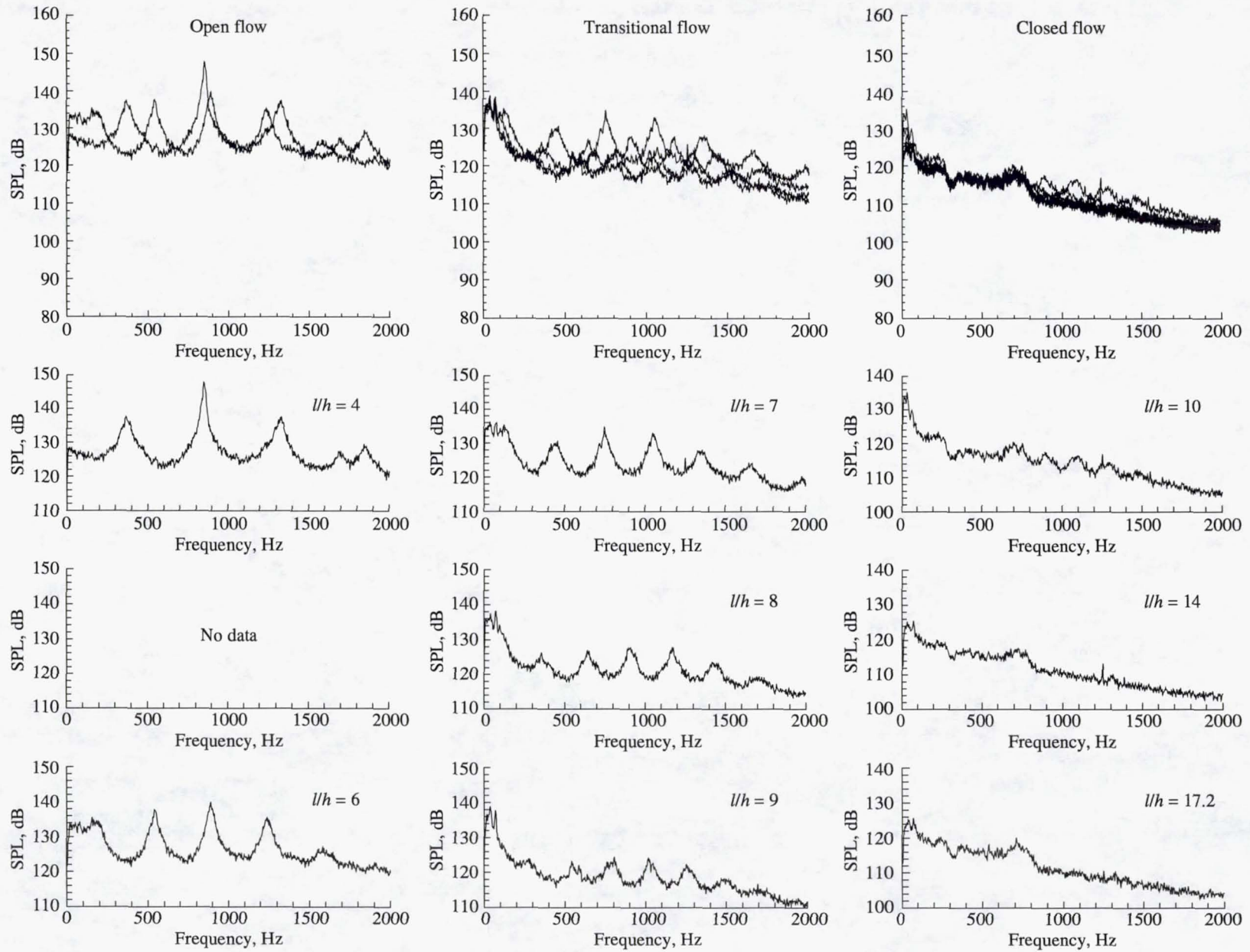
(d)  $M_\infty = 0.80$ .

Figure 12. Continued.



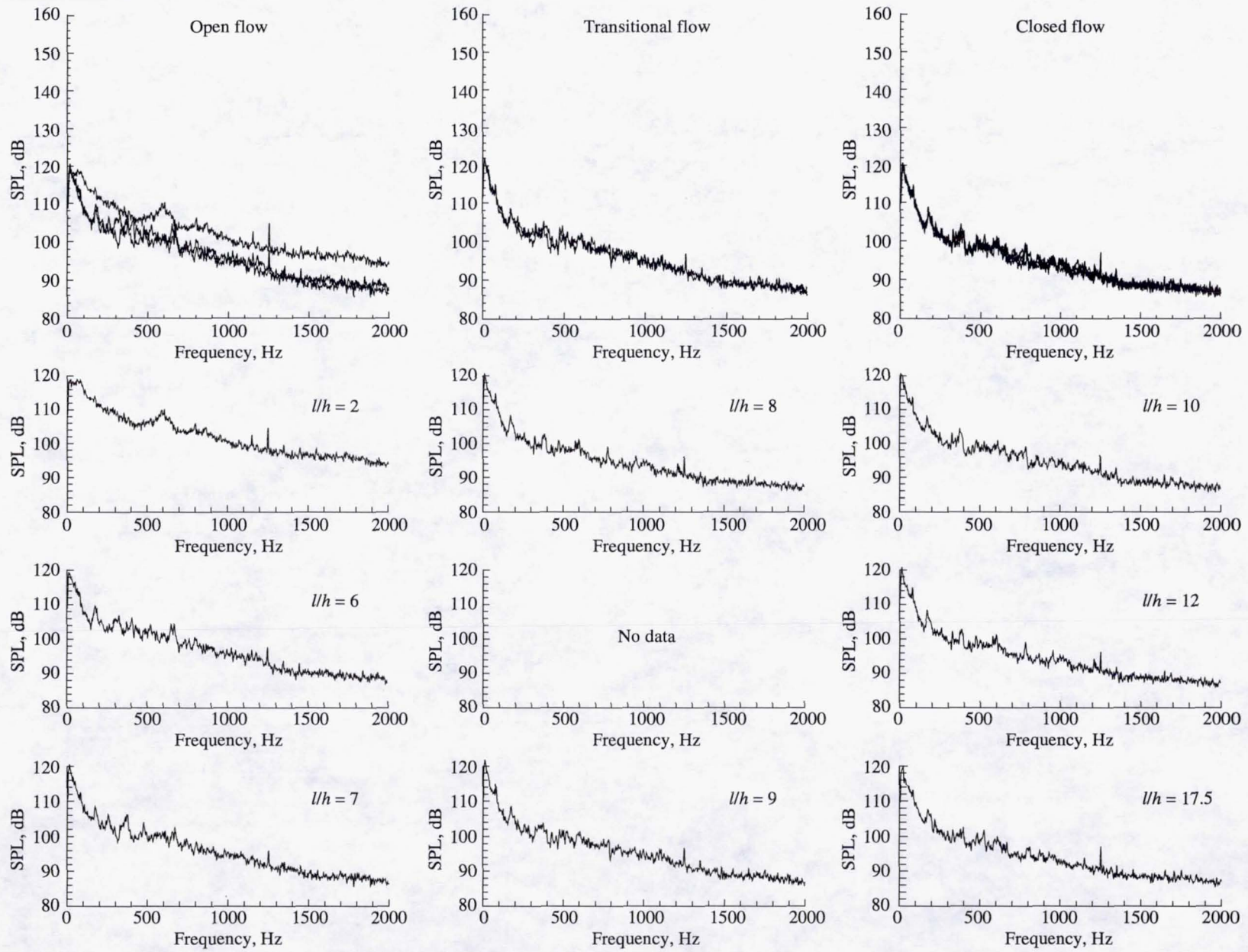
(e)  $M_\infty = 0.90$ .

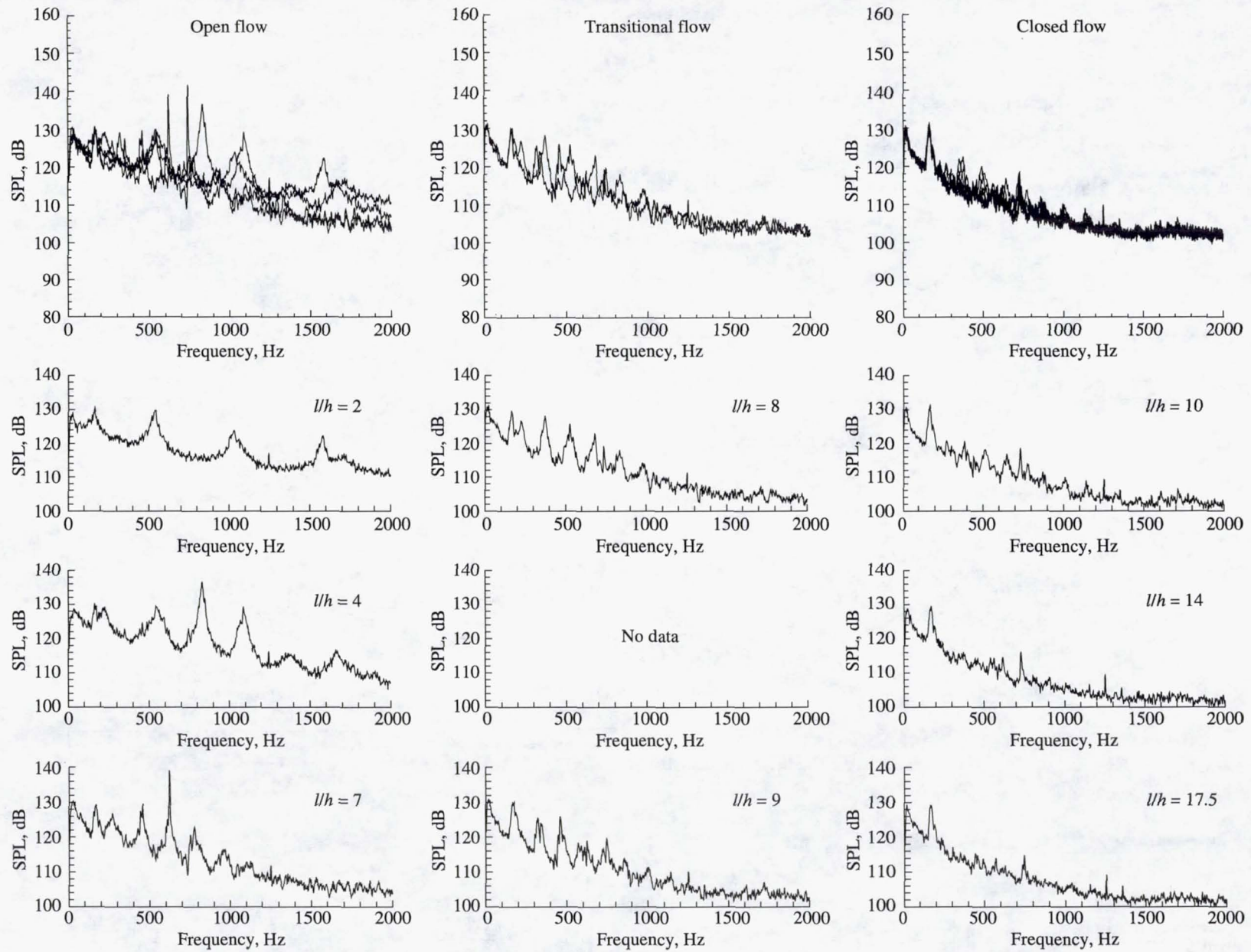
Figure 12. Continued.



(f)  $M_\infty = 0.95$ .

Figure 12. Concluded.

(a)  $M_\infty = 0.20$ .Figure 13. Effect of cavity  $l/h$  on unsteady-pressure spectra from transducer 1 for  $w = 9.6$  in. and  $h = 2.4$  in.



(b)  $M_\infty = 0.40$ .

Figure 13. Continued.

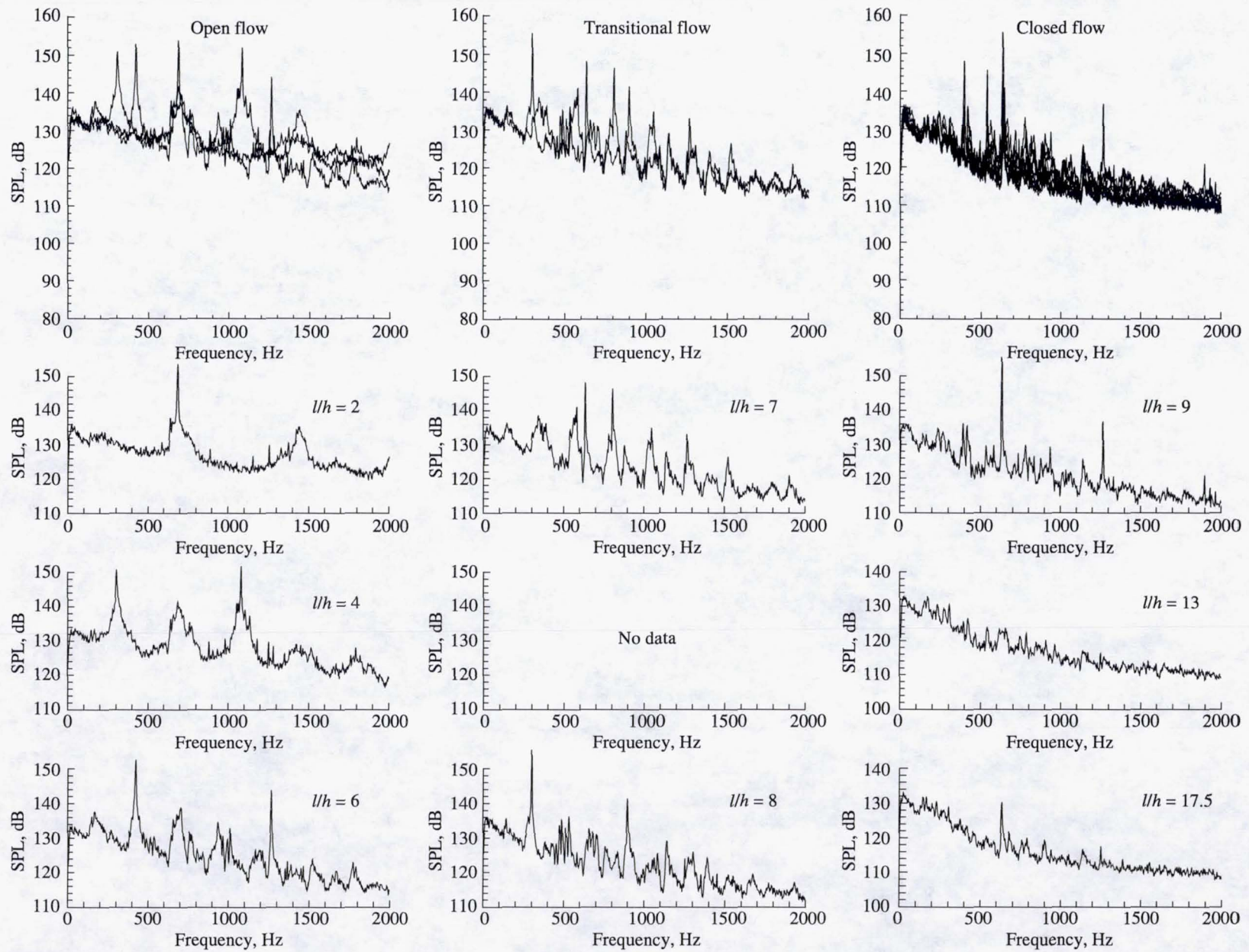
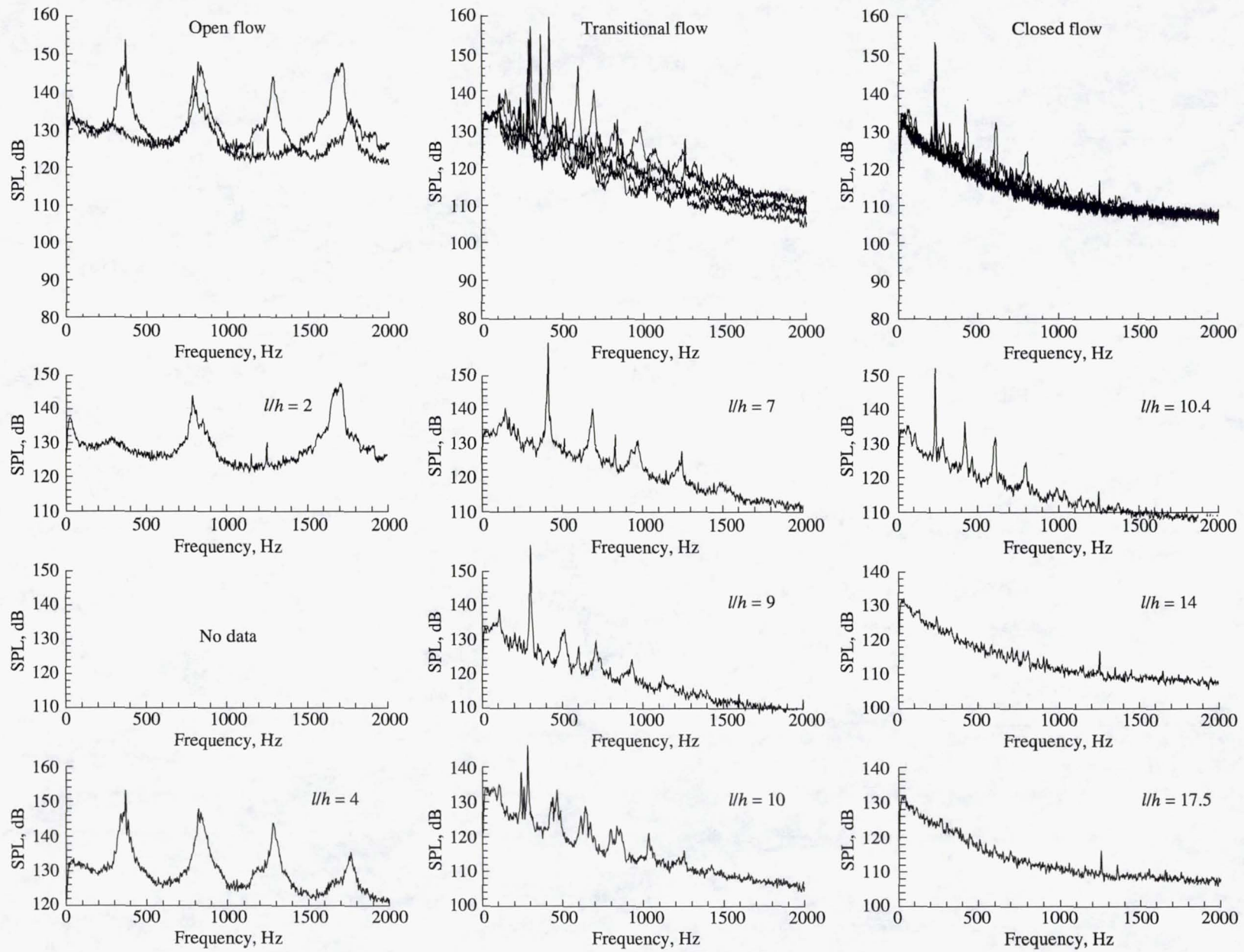
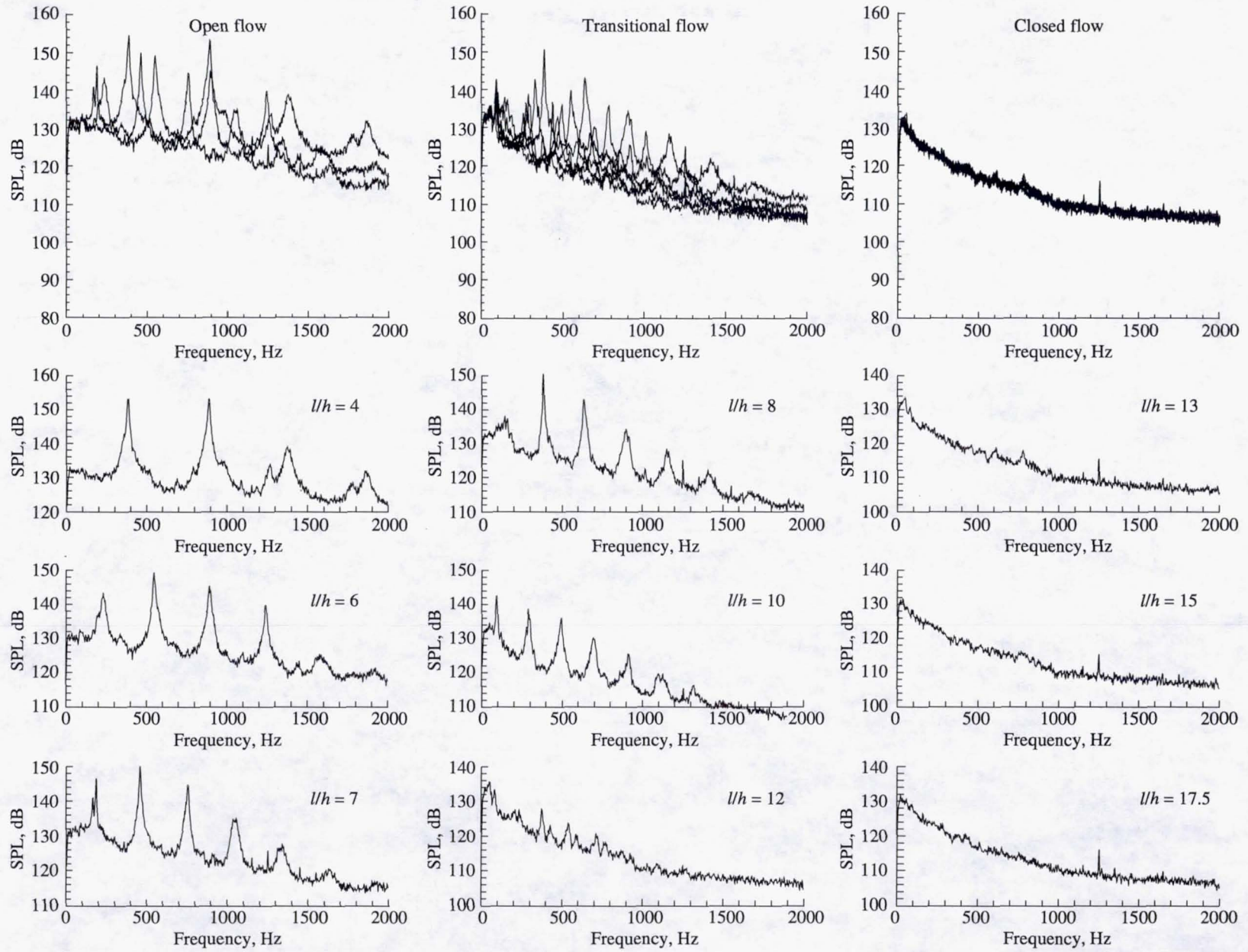
(c)  $M_\infty = 0.60$ .

Figure 13. Continued.



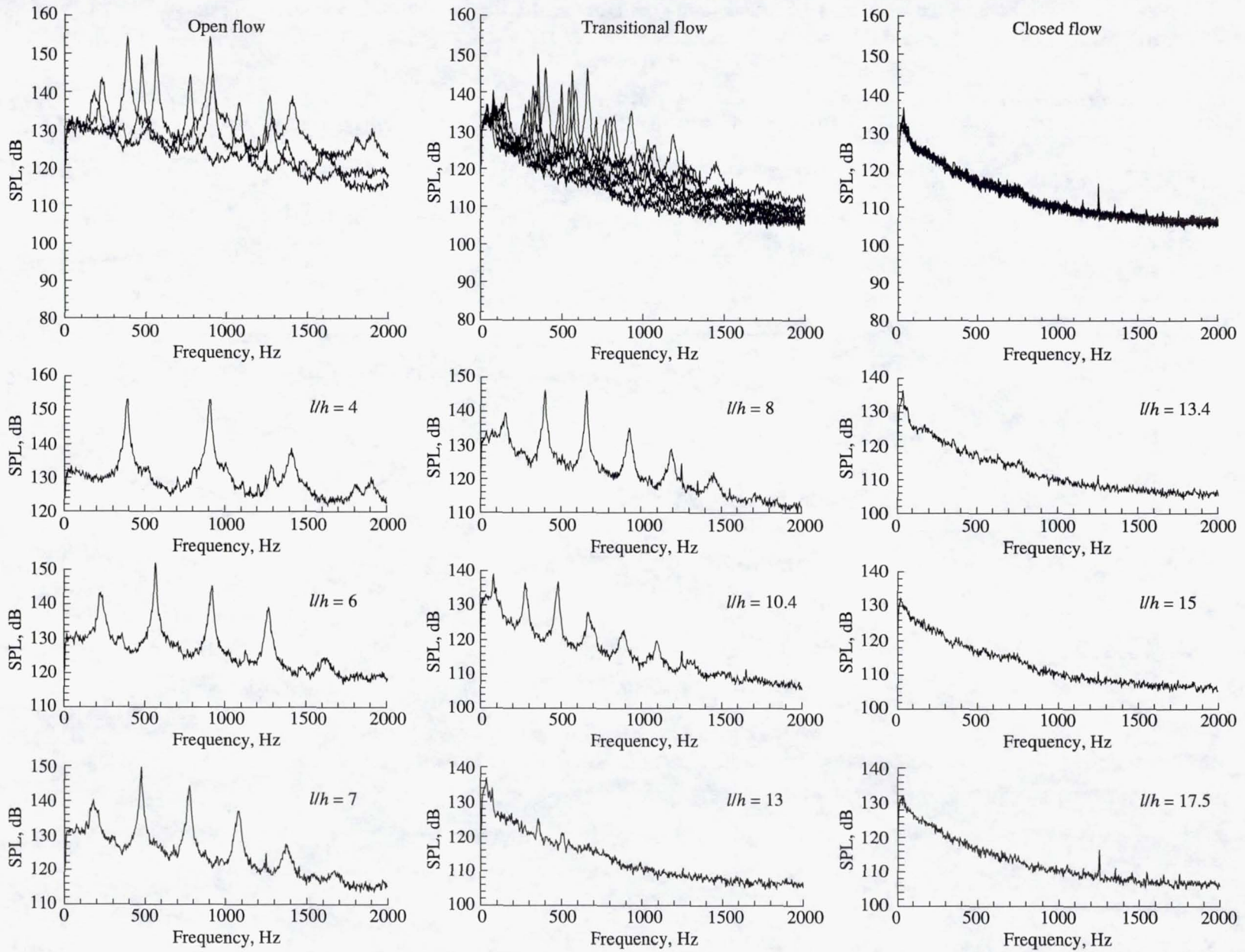
(d)  $M_\infty = 0.80$ .

Figure 13. Continued.



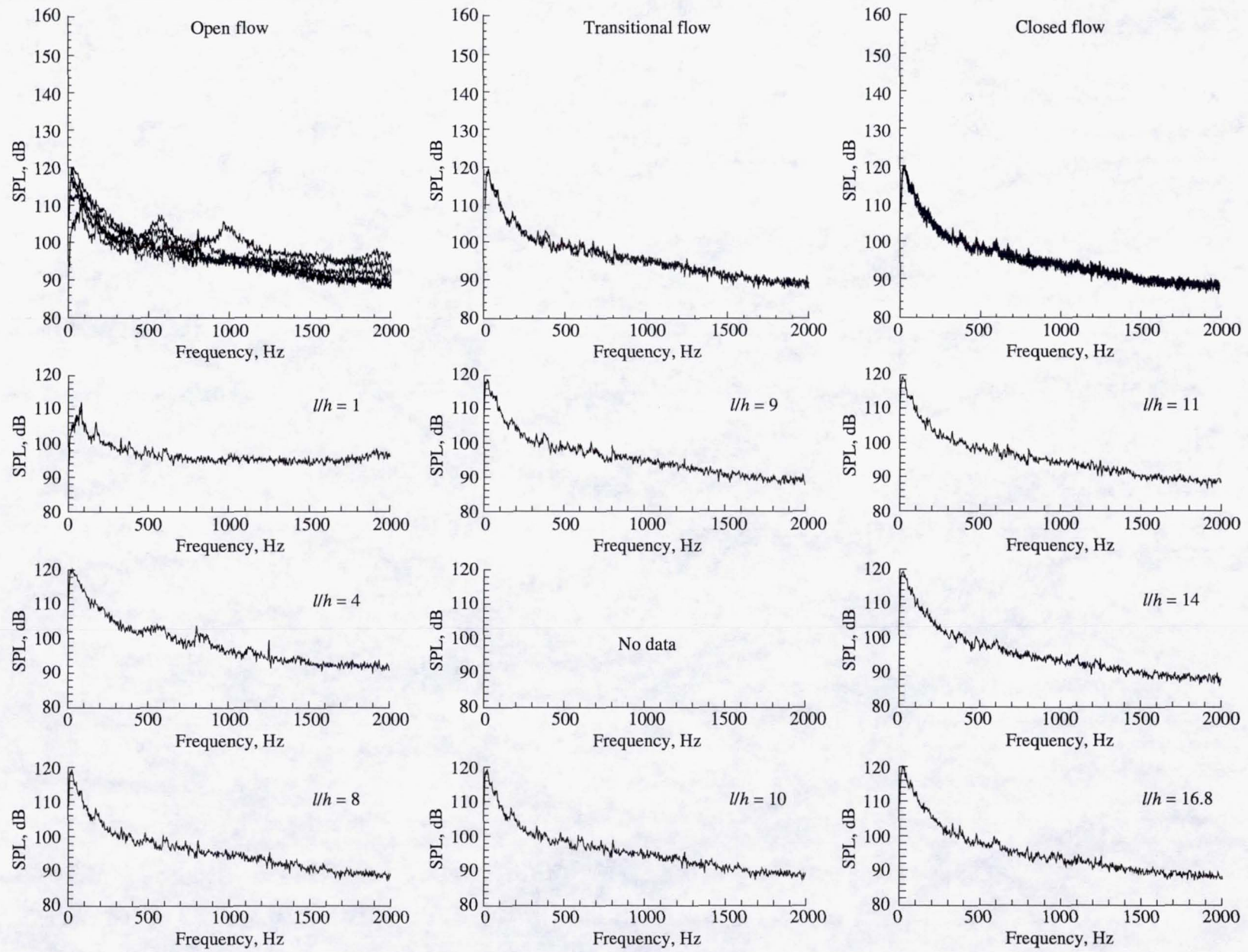
(e)  $M_\infty = 0.90$ .

Figure 13. Continued.



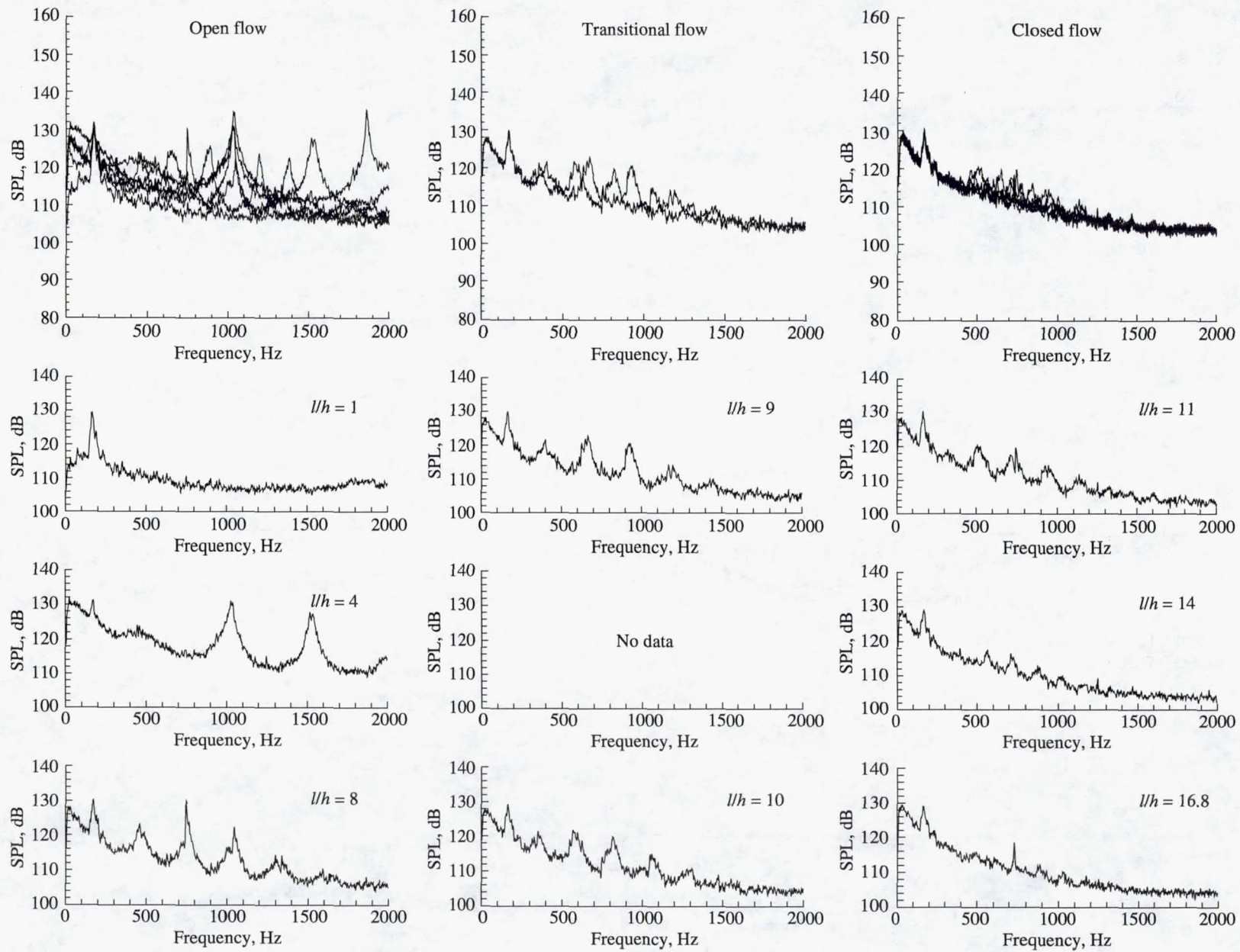
(f)  $M_\infty = 0.95$ .

Figure 13. Concluded.



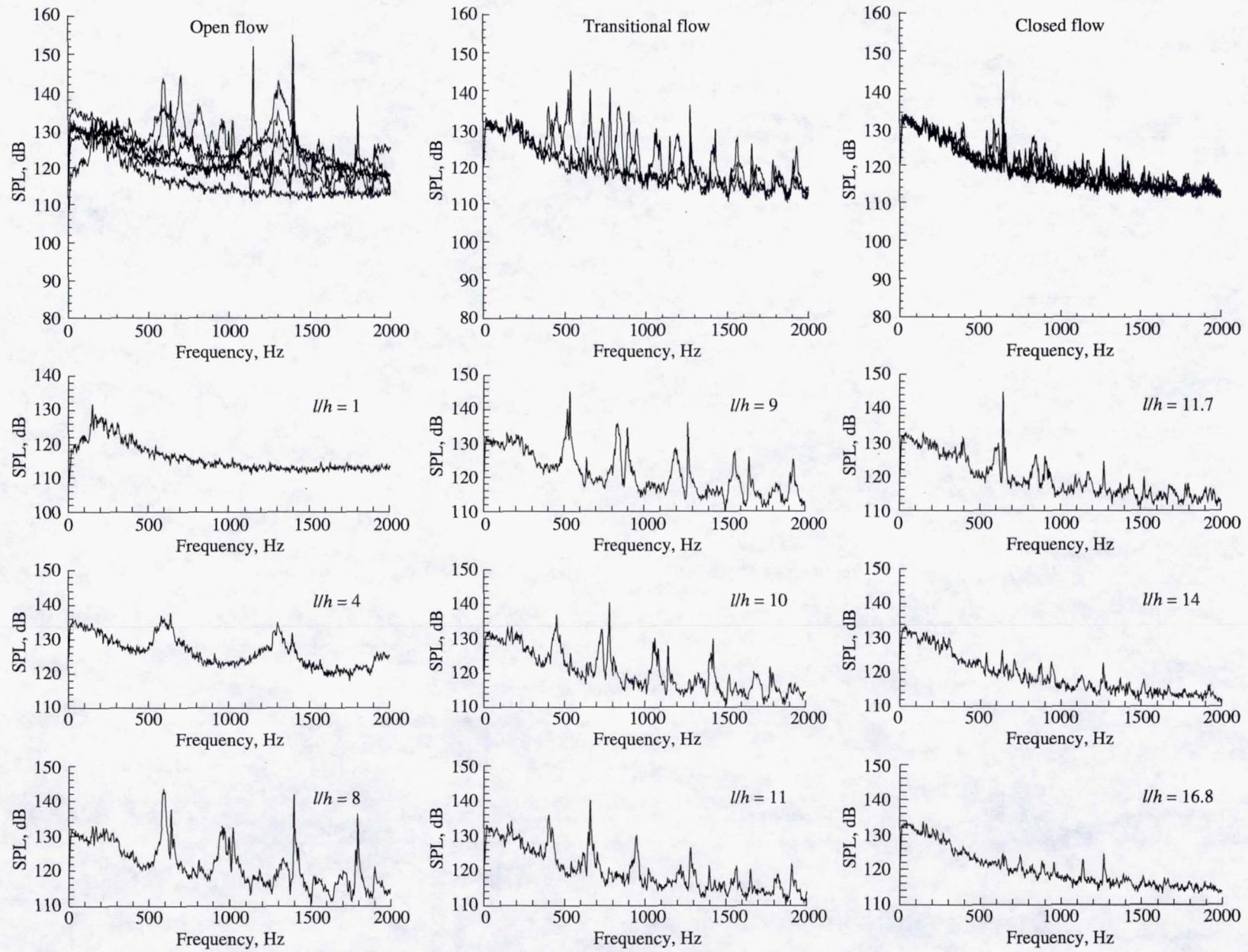
(a)  $M_\infty = 0.20$ .

Figure 14. Effect of cavity  $l/h$  on unsteady-pressure spectra from transducer 1 for  $w = 9.6$  in. and  $h = 1.2$  in.



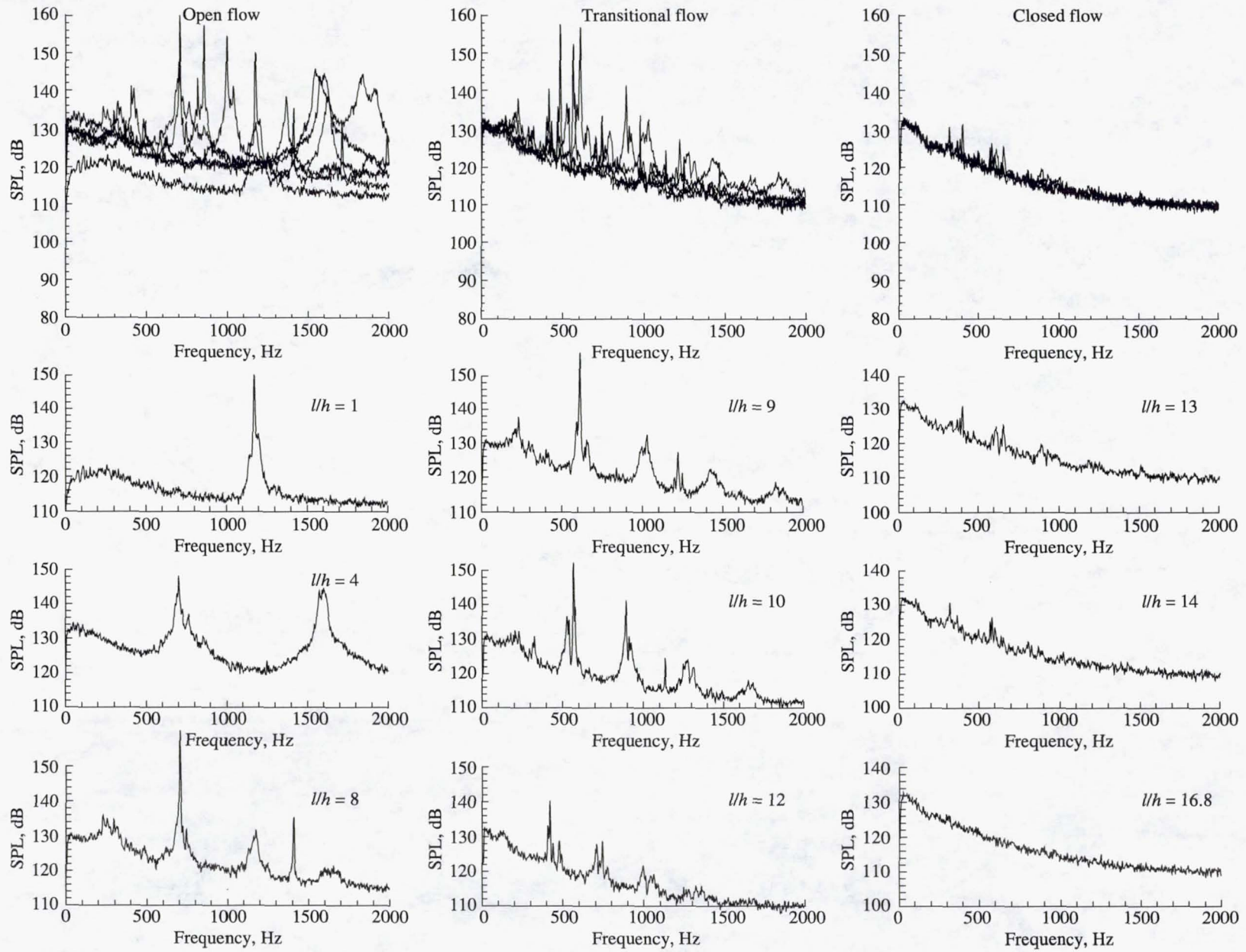
(b)  $M_\infty = 0.40$ .

Figure 14. Continued.



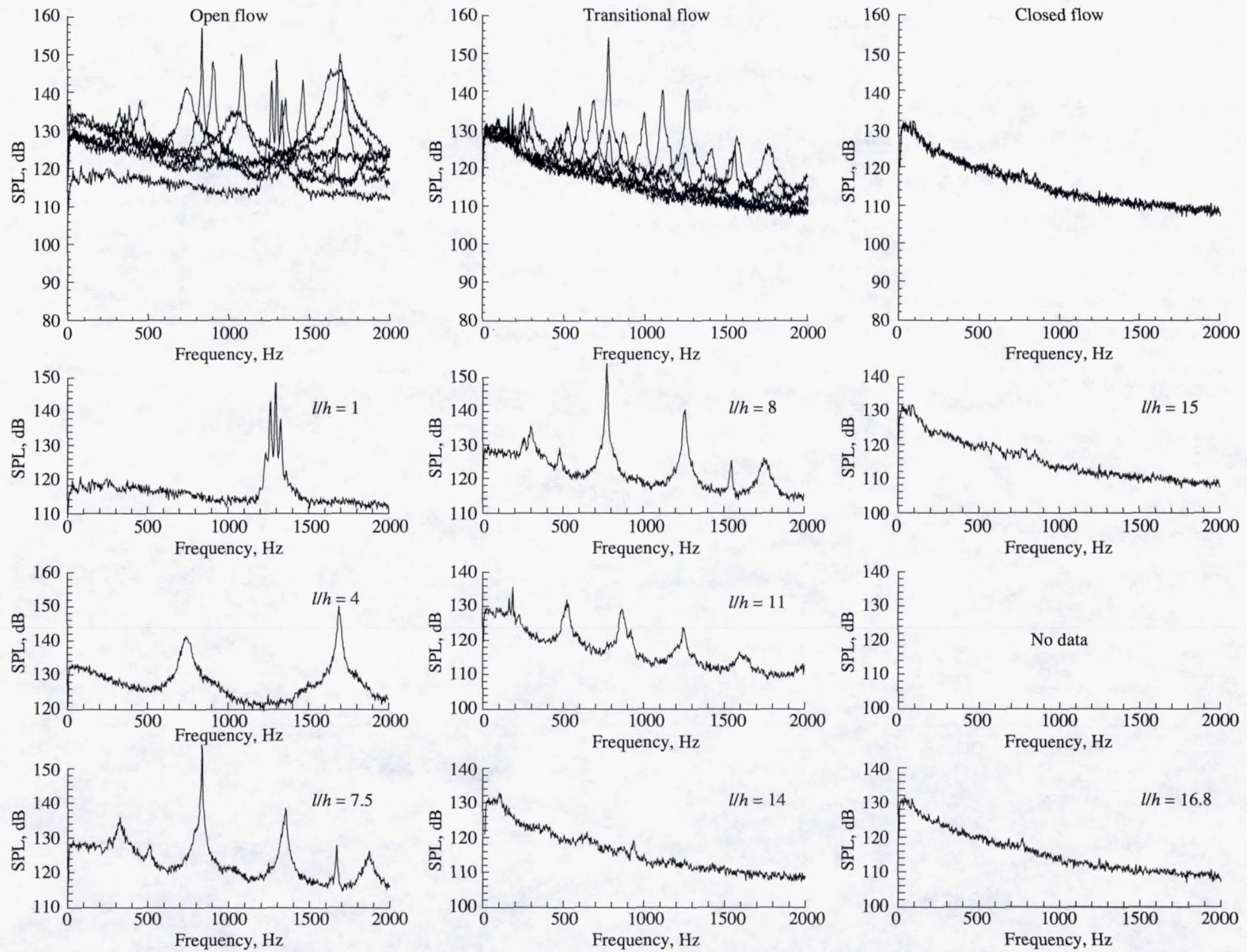
(c)  $M_\infty = 0.60$ .

Figure 14. Continued.



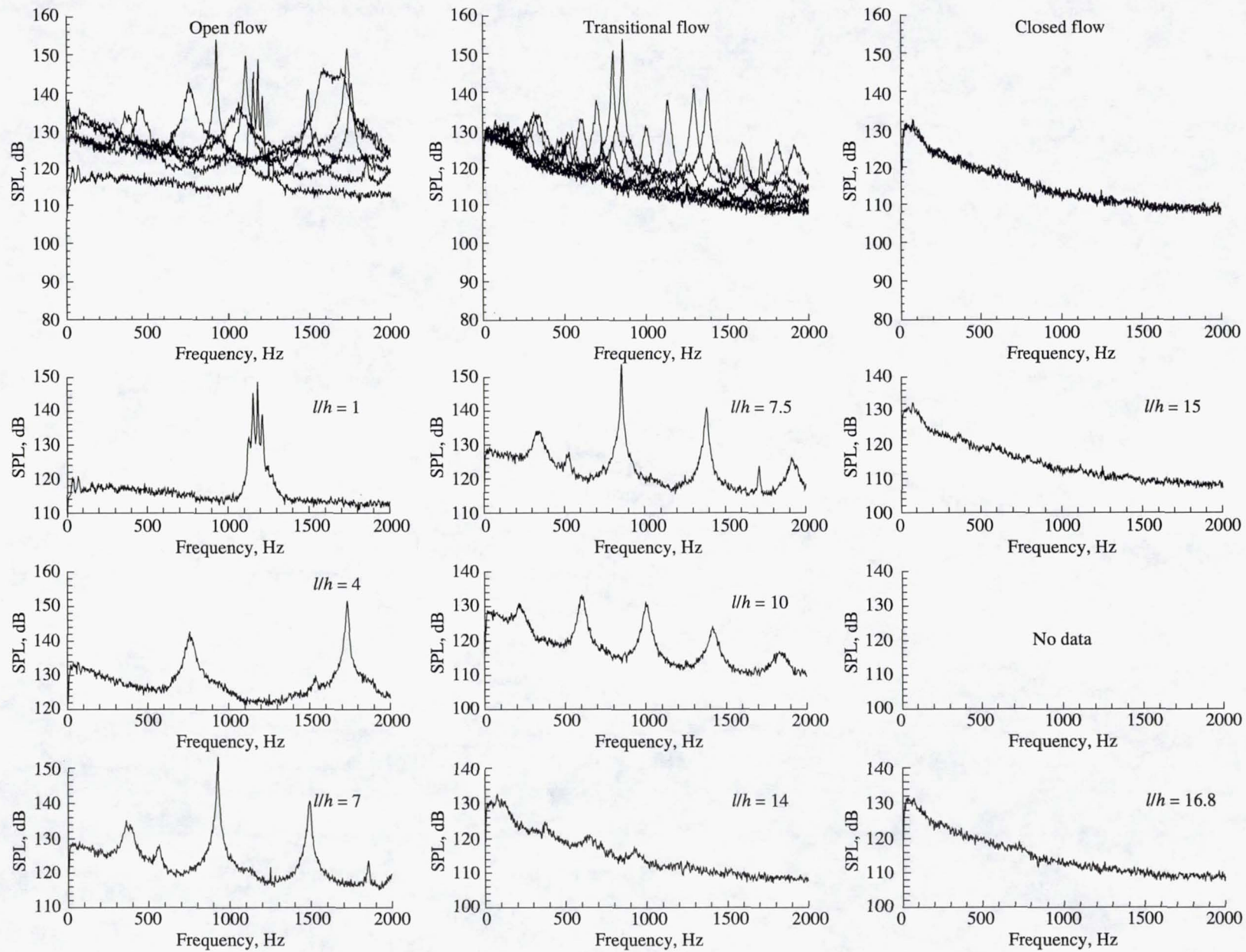
(d)  $M_\infty = 0.80$ .

Figure 14. Continued.



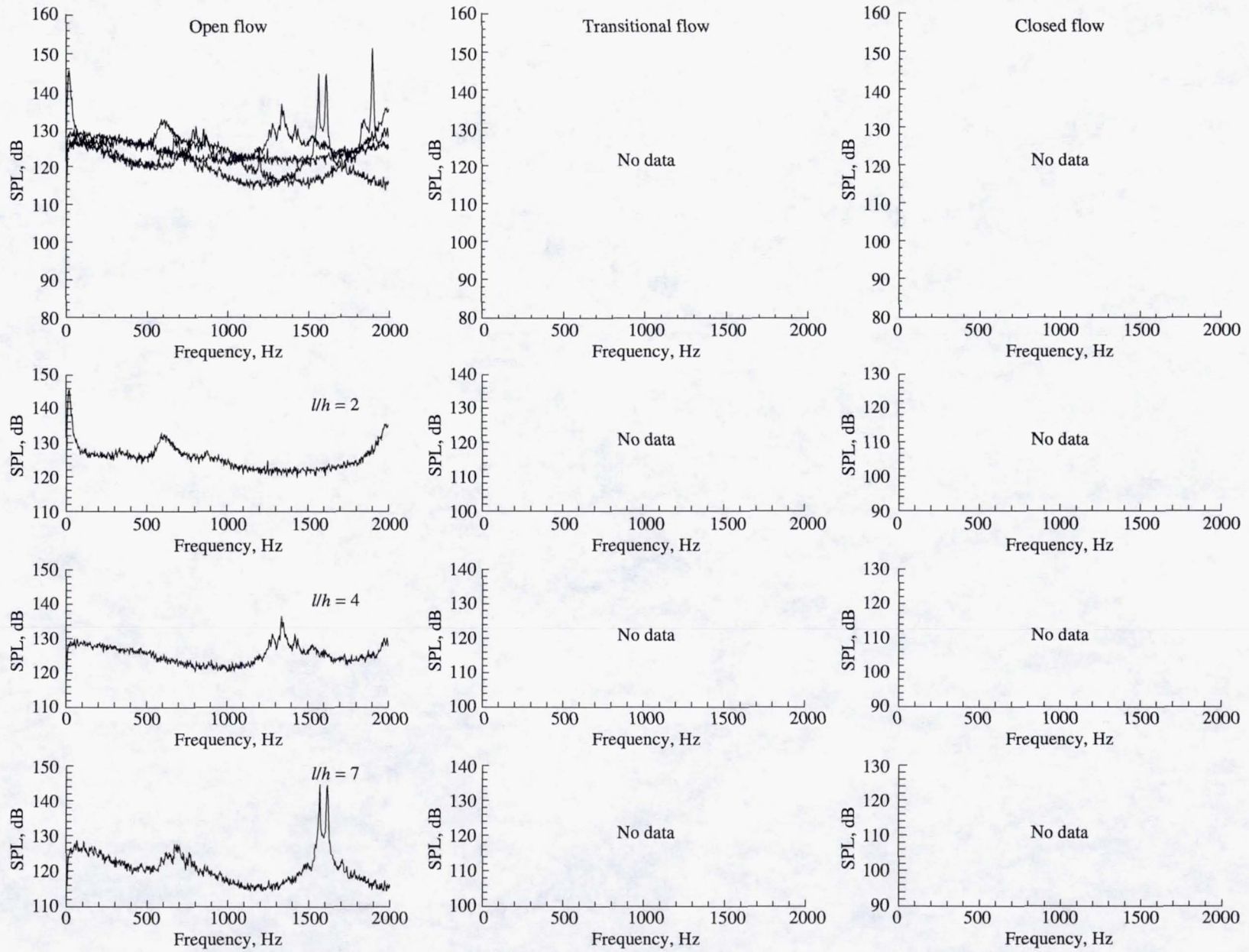
(e)  $M_\infty = 0.90$ .

Figure 14. Continued.



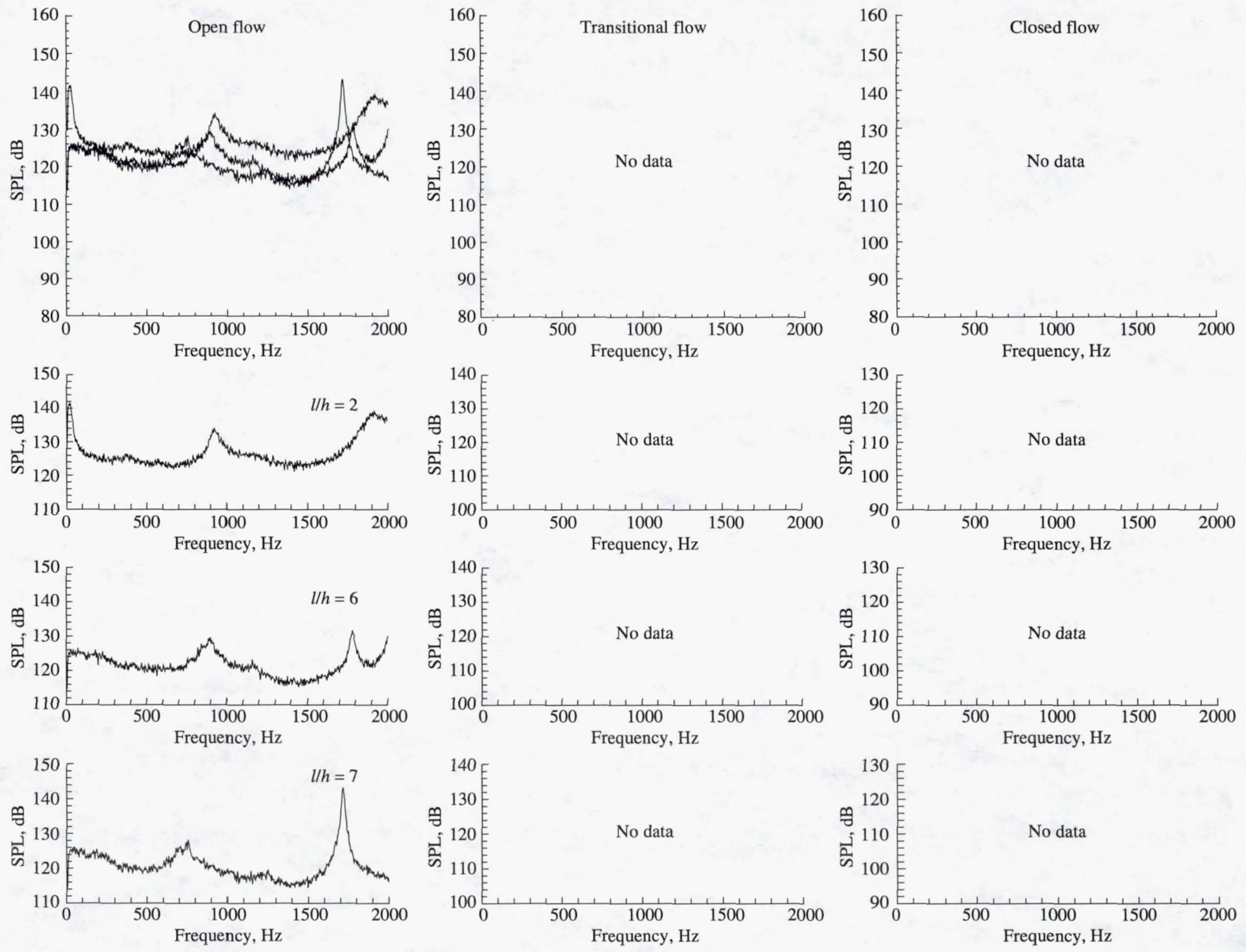
(f)  $M_\infty = 0.95$ .

Figure 14. Concluded.



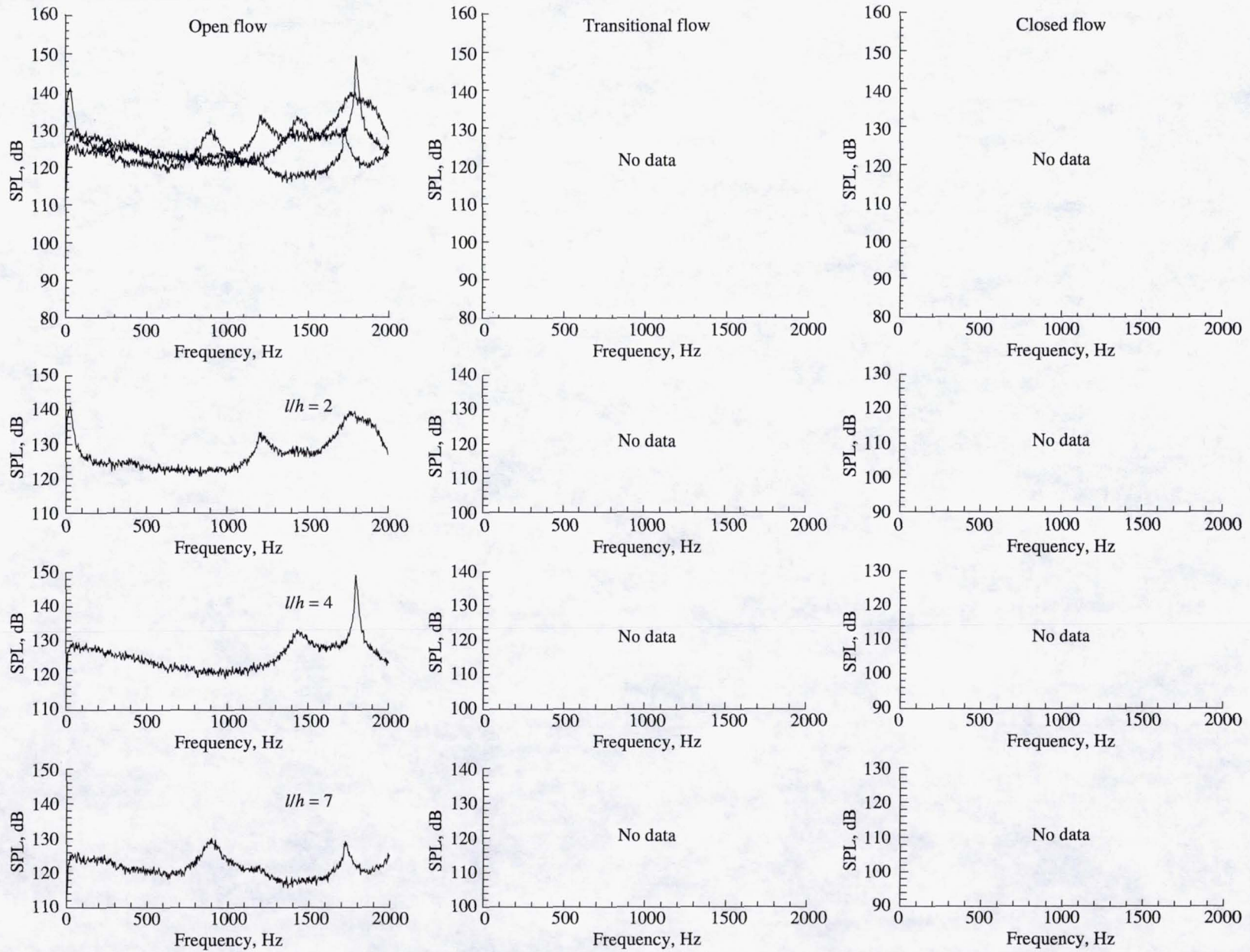
(a)  $M_\infty = 0.80$ .

Figure 15. Effect of cavity  $l/h$  on unsteady-pressure spectra from transducer 1 for  $w = 9.6$  in. and  $h = 0.6$  in.



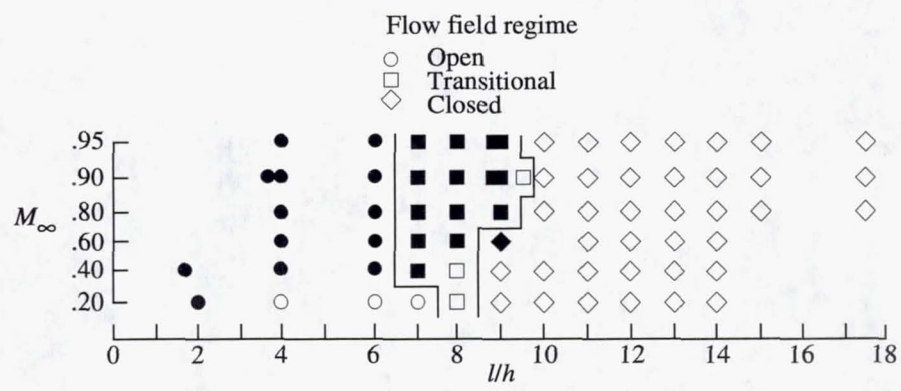
(b)  $M_\infty = 0.90$ .

Figure 15. Continued.

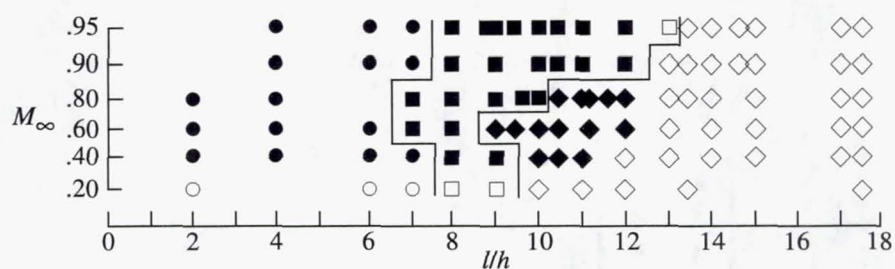


(c)  $M_\infty = 0.95$ .

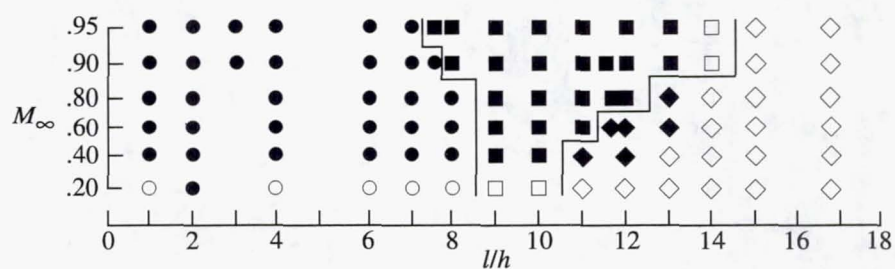
Figure 15. Concluded.



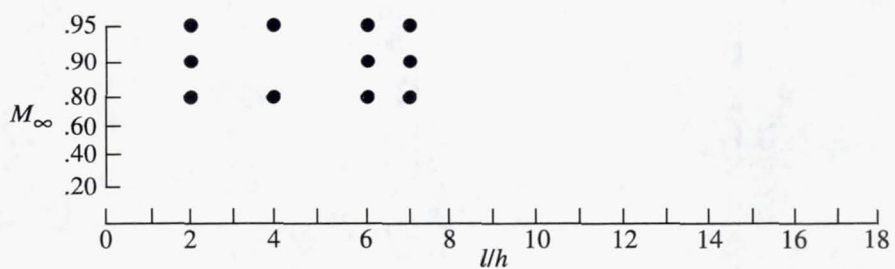
(a)  $w = 2.4$  in.;  $h = 2.4$  in.



(b)  $w = 9.6$  in.;  $h = 2.4$  in.

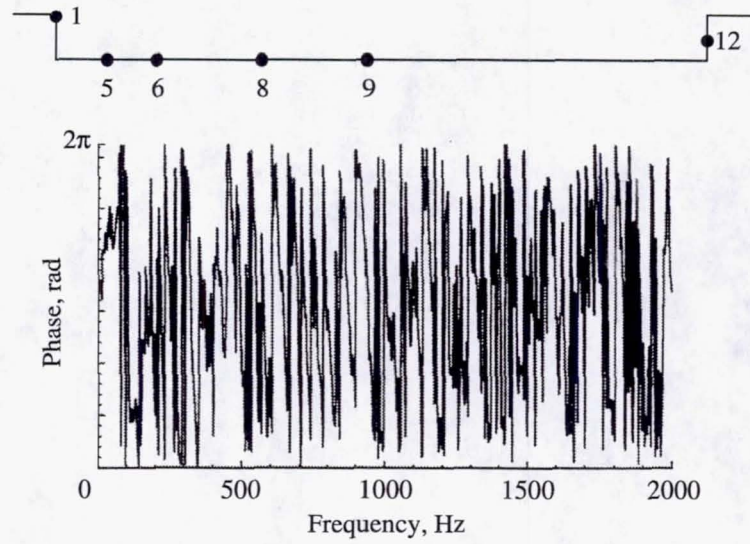


(c)  $w = 9.6$  in.;  $h = 1.2$  in.

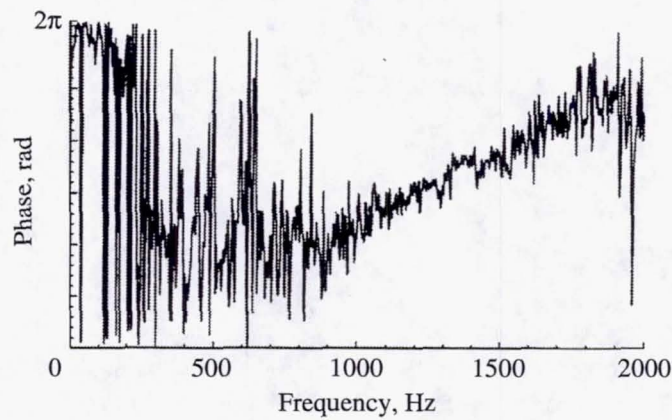


(d)  $w = 9.6$  in.;  $h = 0.6$  in.

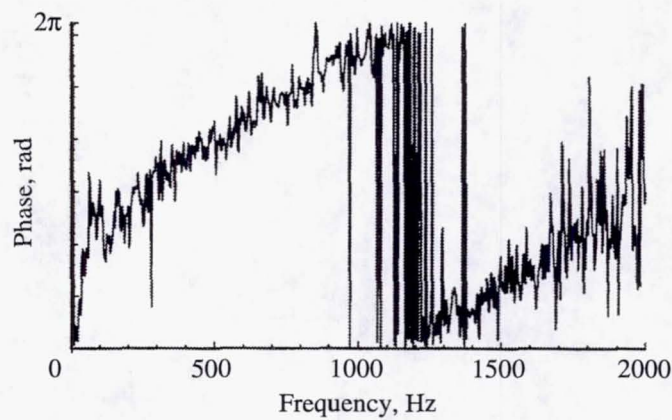
Figure 16. Occurrence of cavity resonance (superimposed on fig. 3). Solid symbols indicate resonant conditions.



(a) Fore and aft walls; transducers 1 and 12.

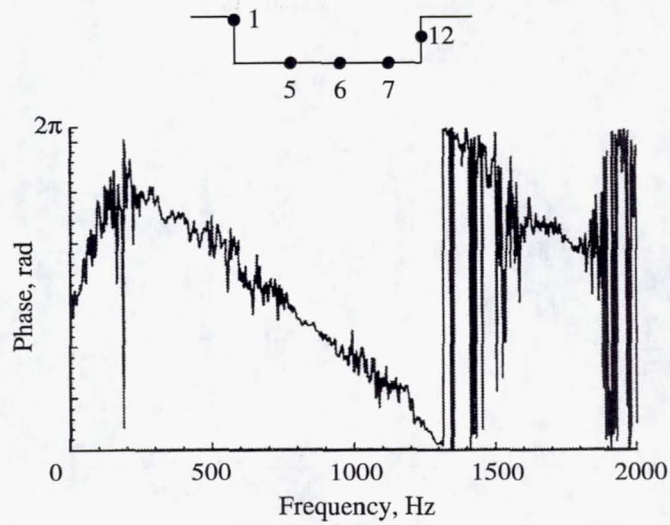


(b) Floor; transducers 5 and 6.

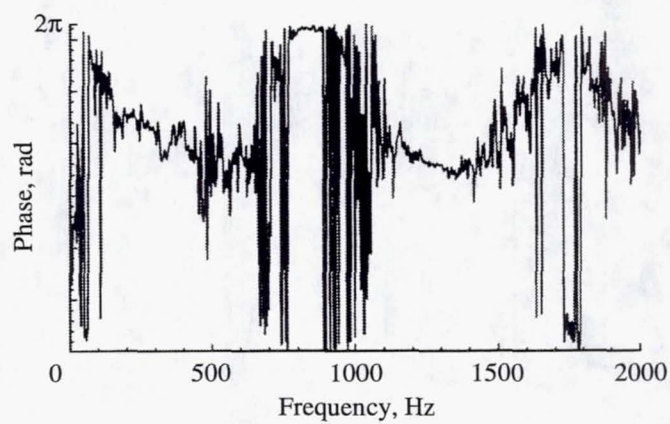


(c) Floor; transducers 8 and 9.

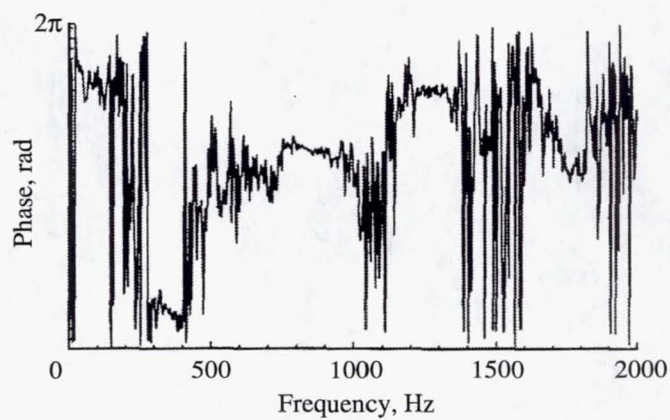
Figure 17. Phase shift between transducers in closed cavity flow without resonance for  $l/h = 14$  and  $M_\infty = 0.80$ .



(a) Fore and aft walls; transducers 1 and 12.

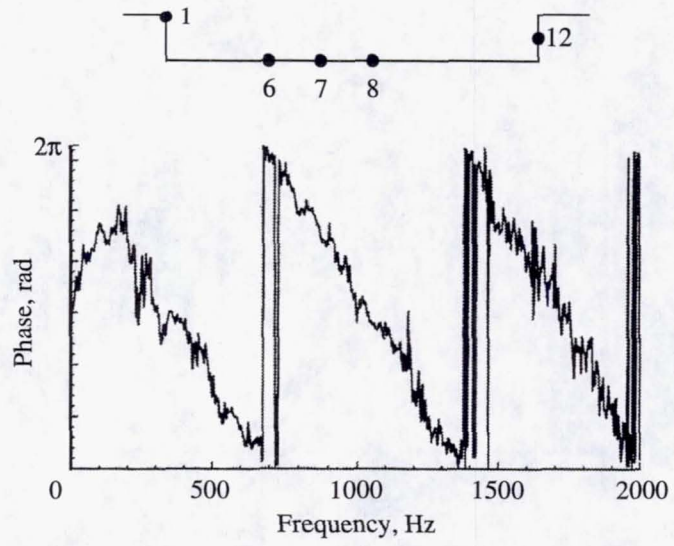


(b) Floor; transducers 5 and 6.

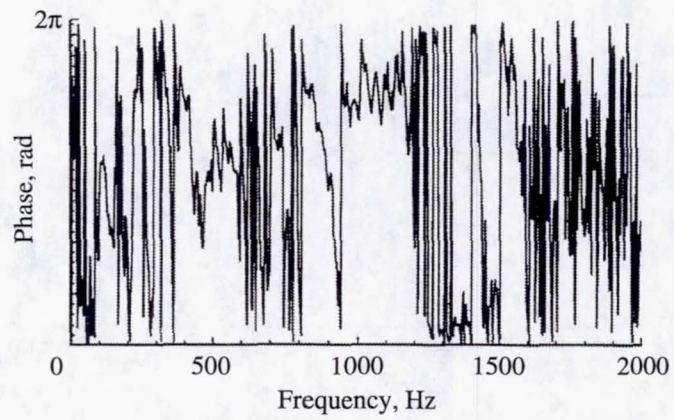


(c) Floor; transducers 6 and 7.

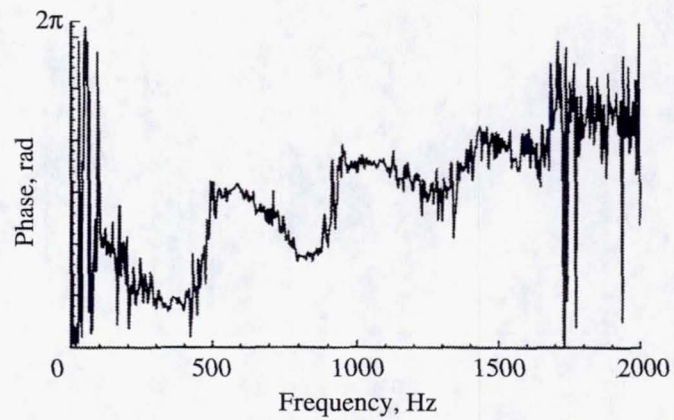
Figure 18. Phase shift between transducers in open cavity flow with resonance for  $l/h = 4$  and  $M_\infty = 0.80$ .



(a) Fore and aft walls; transducers 1 and 12.

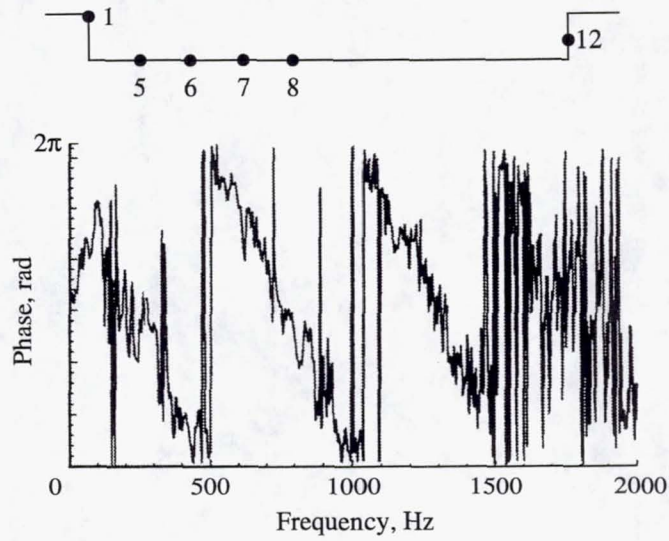


(b) Floor; transducers 6 and 7.

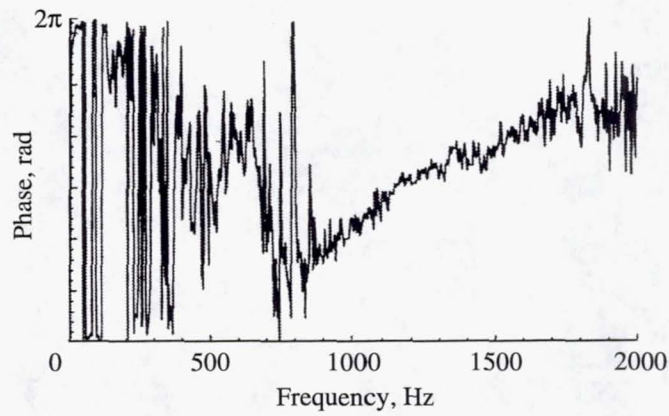


(c) Floor; transducers 7 and 8.

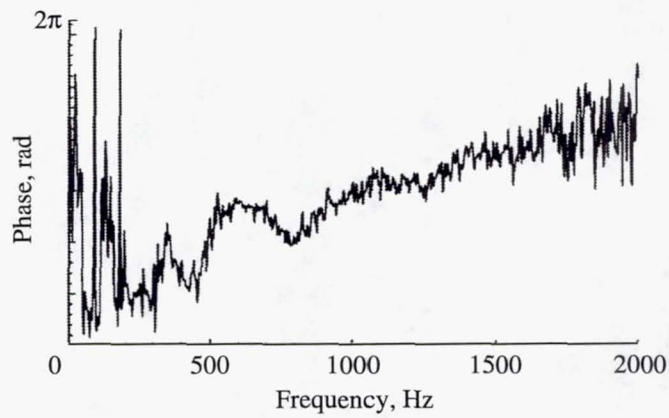
Figure 19. Phase shift between transducers in transitional cavity flow with resonance for  $l/h = 8$  and  $M_\infty = 0.80$ .



(a) Fore and aft walls; transducers 1 and 12.



(b) Floor; transducers 5 and 6.



(c) Floor; transducers 7 and 8.

Figure 20. Phase shift between transducers in closed cavity flow with resonance for  $l/h = 10.4$  and  $M_\infty = 0.80$ .

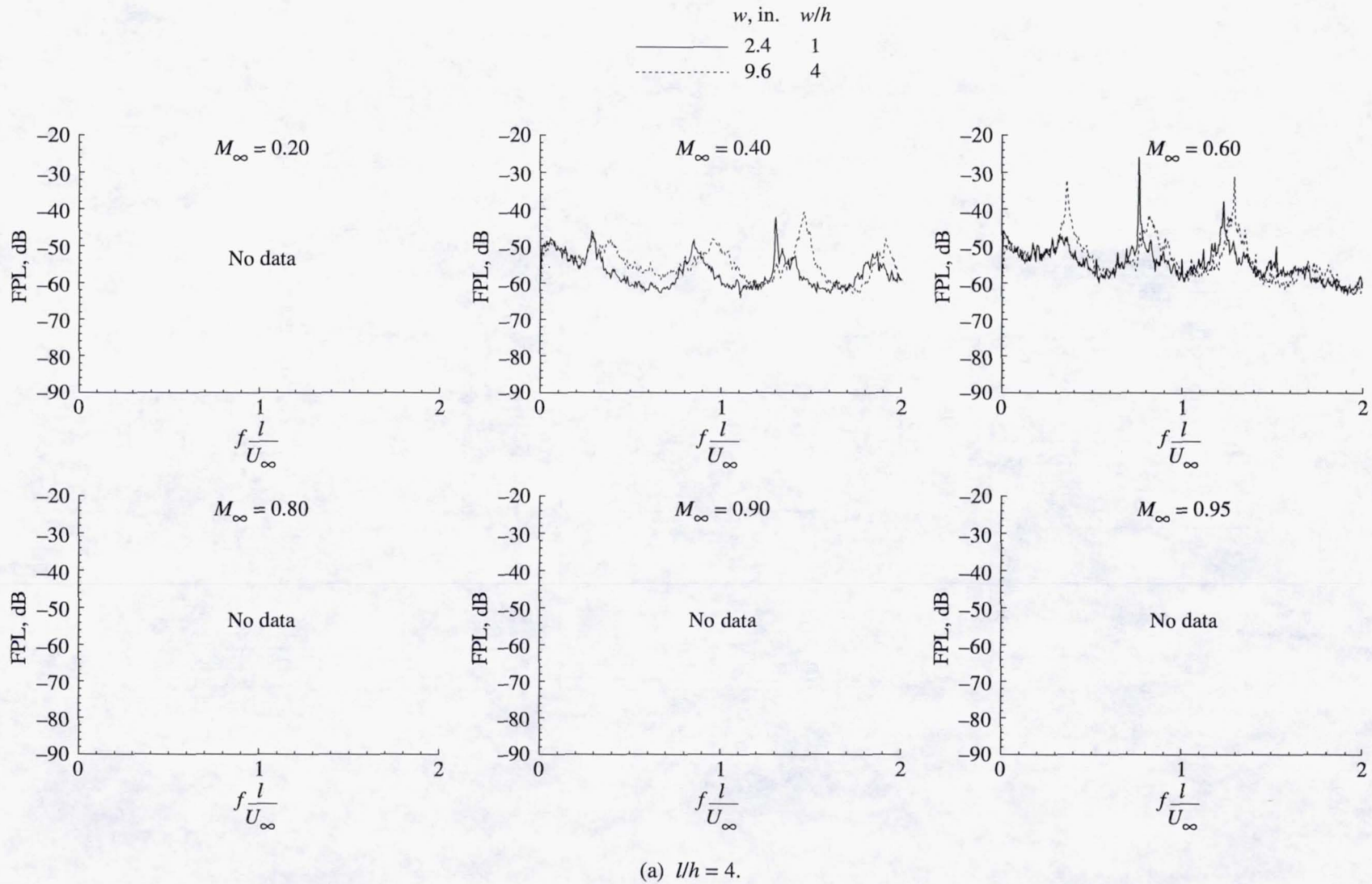
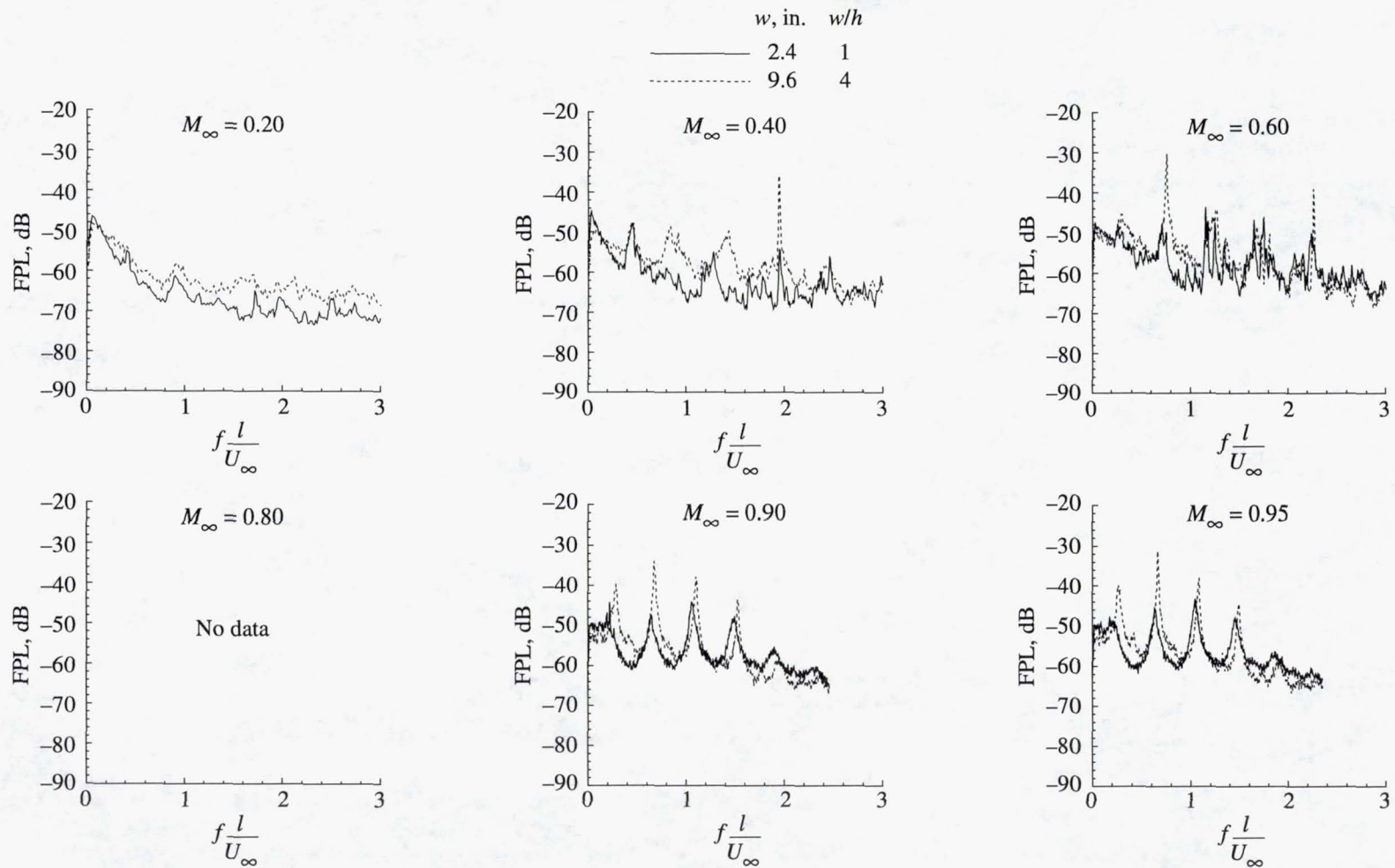


Figure 21. Effect of cavity width on nondimensional unsteady-pressure spectra from transducer 1 for  $h = 2.4$  in.



(b)  $l/h = 6$ .

Figure 21. Continued.

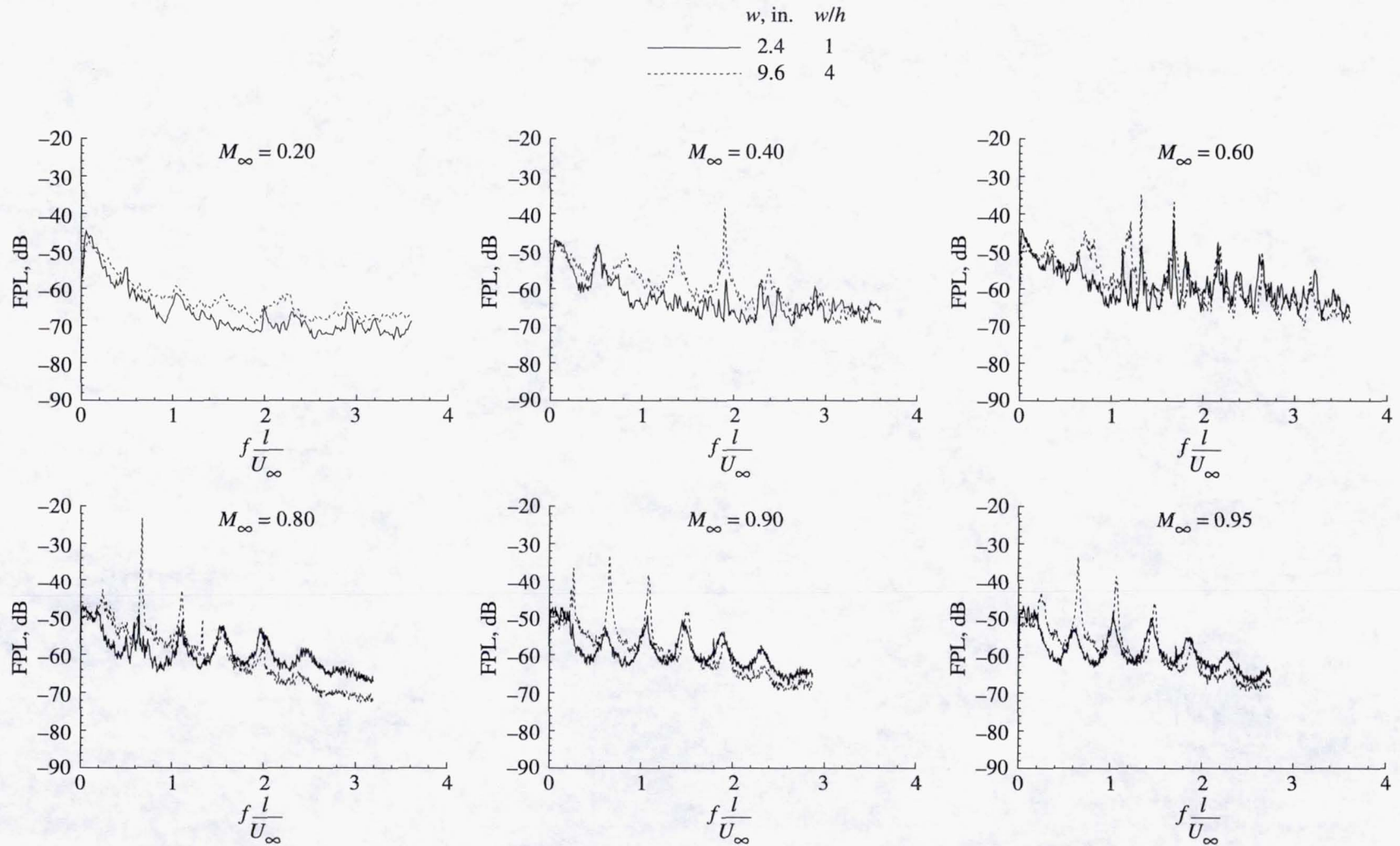
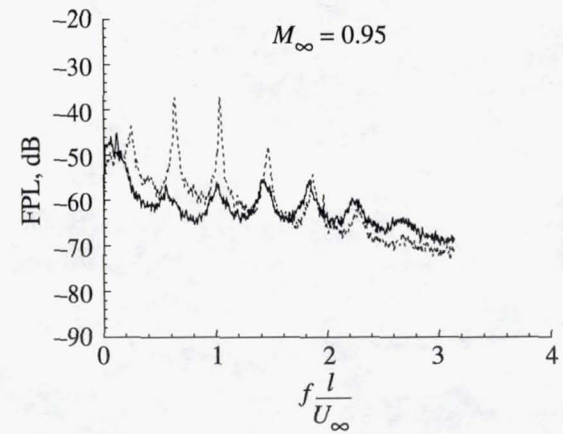
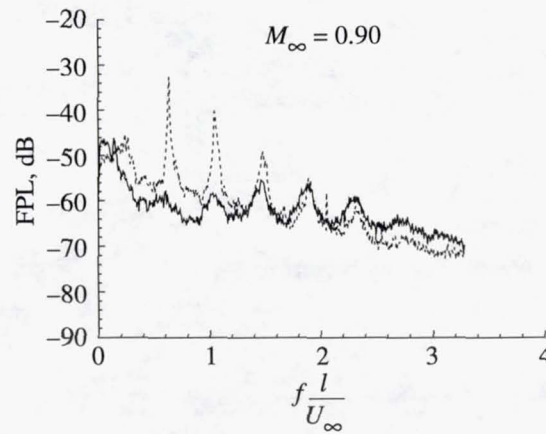
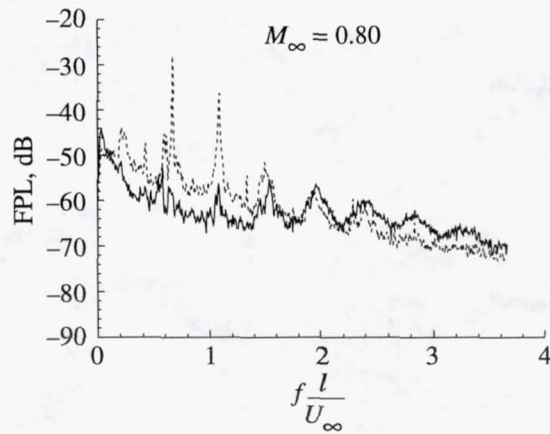
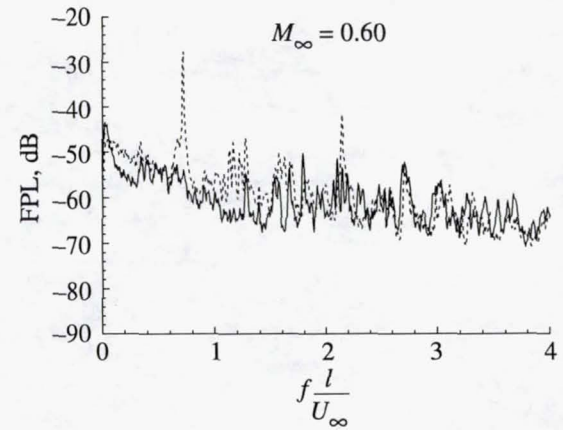
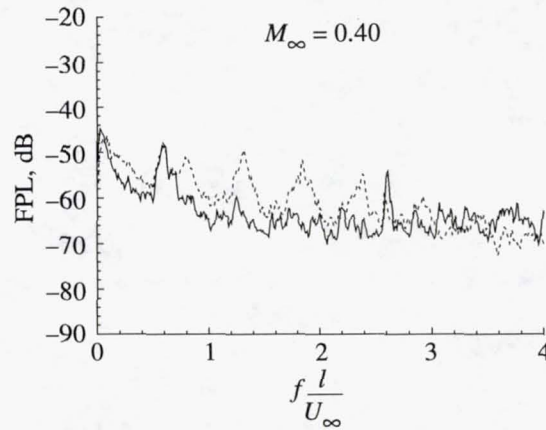
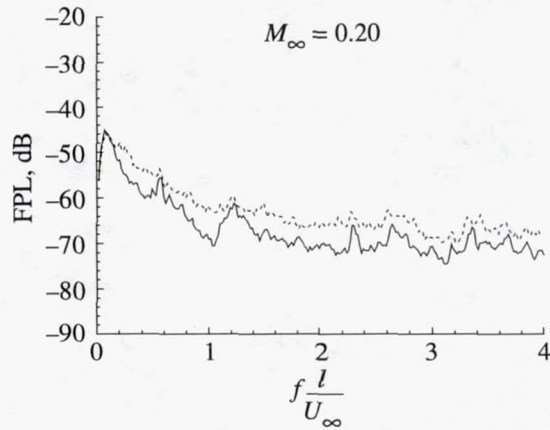
(c)  $lh = 7$ .

Figure 21. Continued.

	<i>w</i> , in.	<i>w/h</i>
—	2.4	1
---	9.6	4



(d)  $lh = 8$ .

Figure 21. Continued.

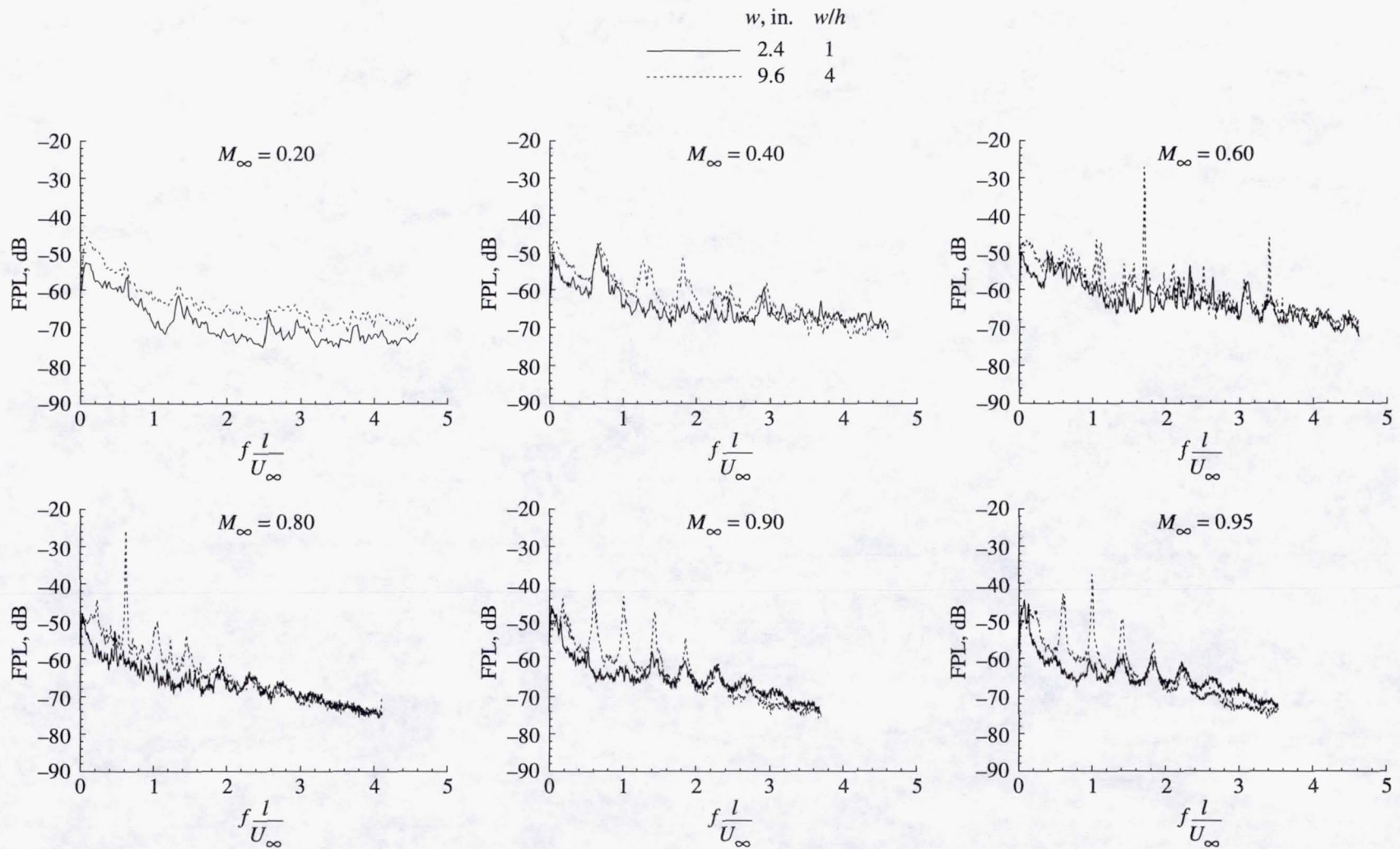
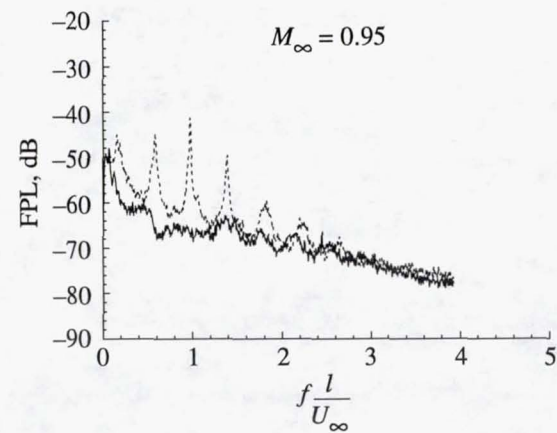
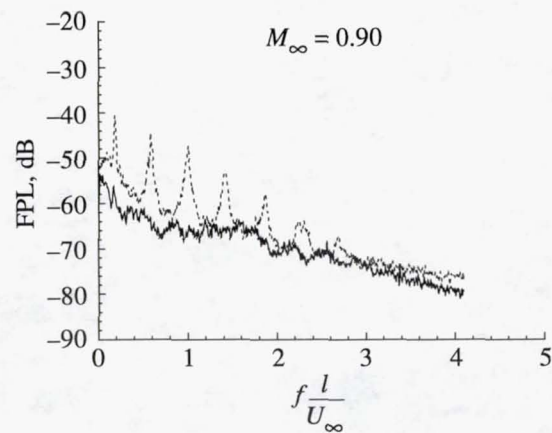
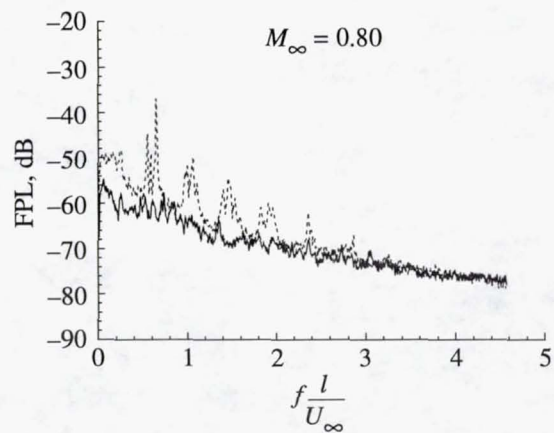
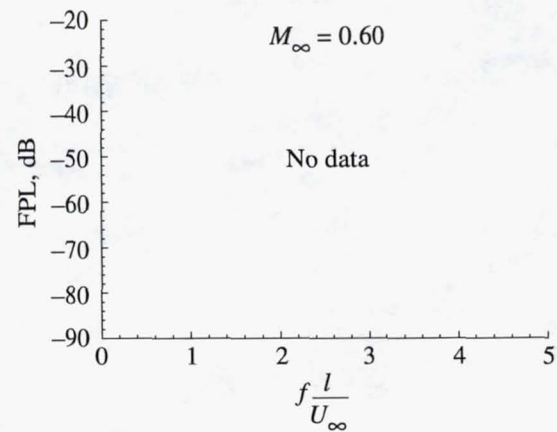
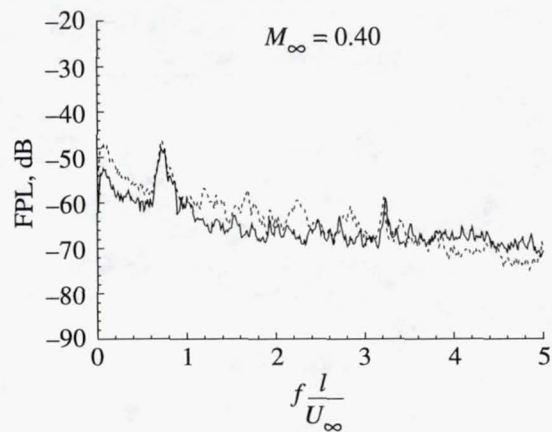
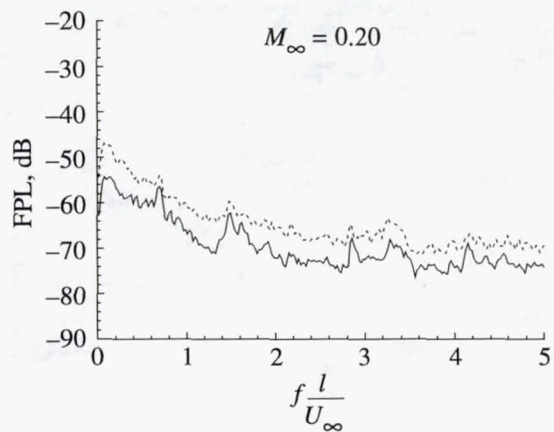
(e)  $l/h = 9$ .

Figure 21. Continued.

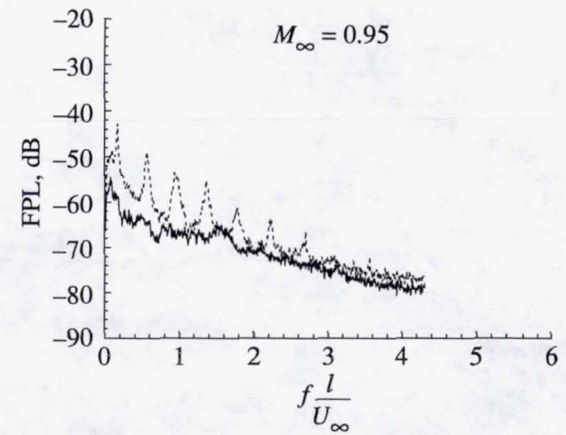
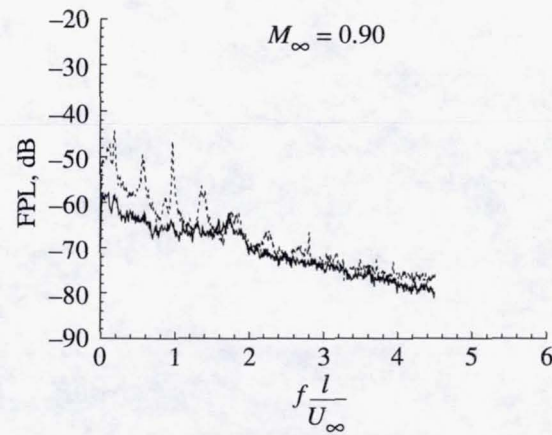
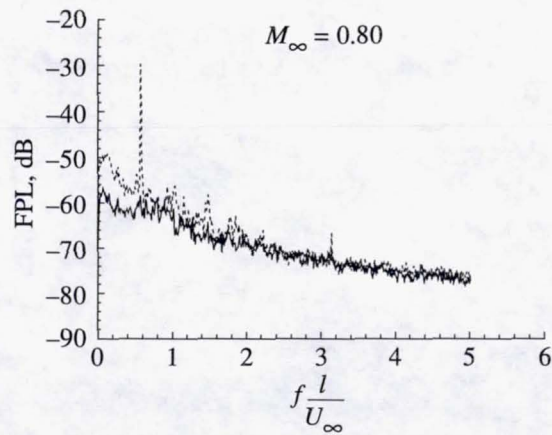
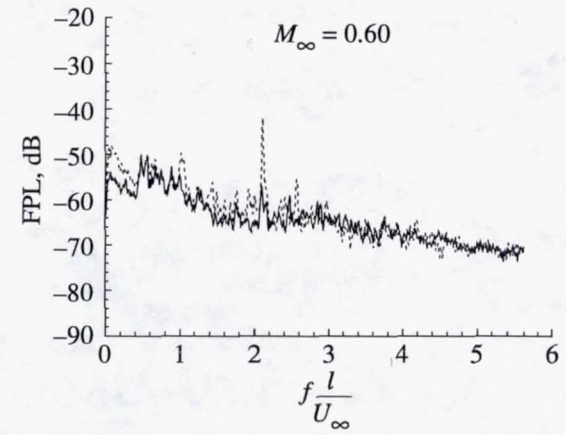
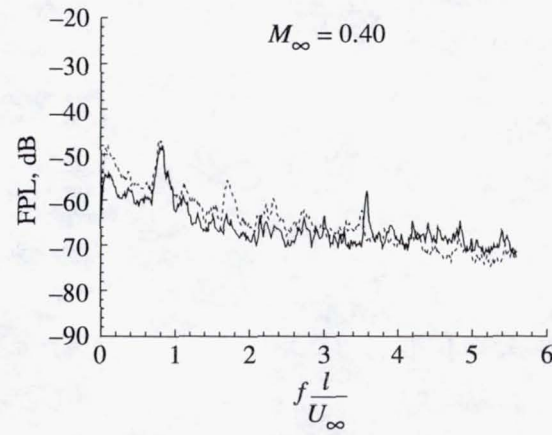
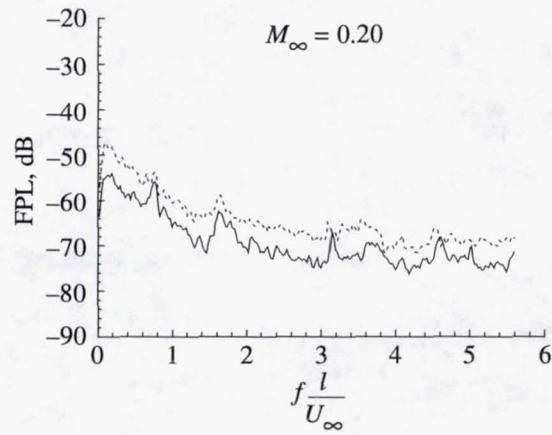
	<i>w</i> , in.	<i>w/h</i>
—	2.4	1
---	9.6	4



(f)  $lh = 10$ .

Figure 21. Continued.

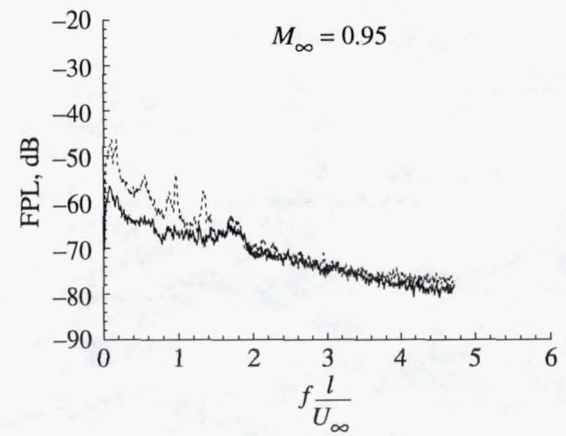
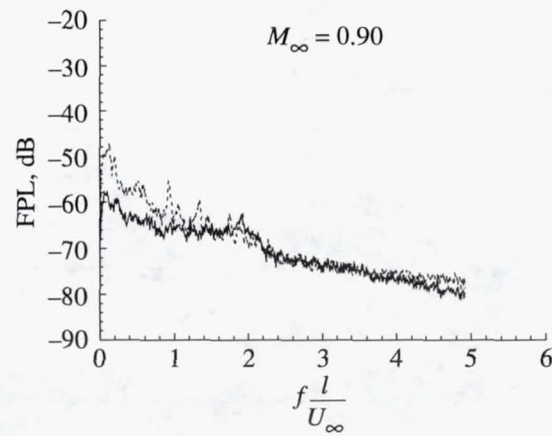
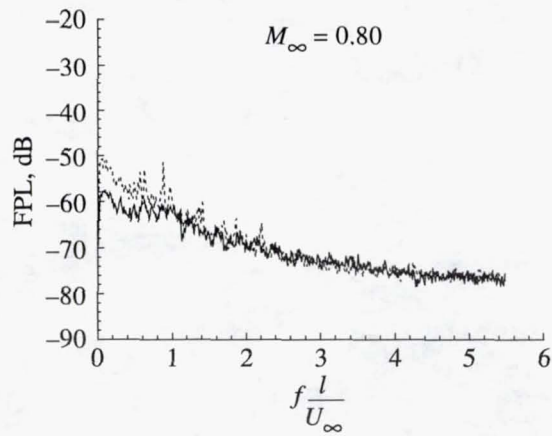
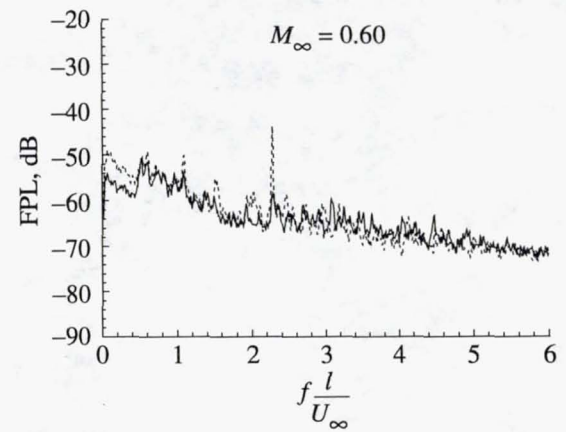
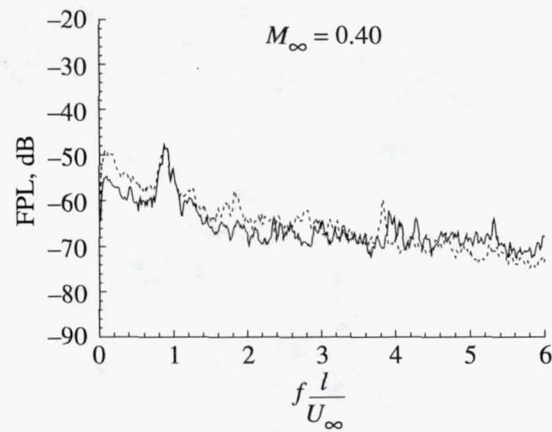
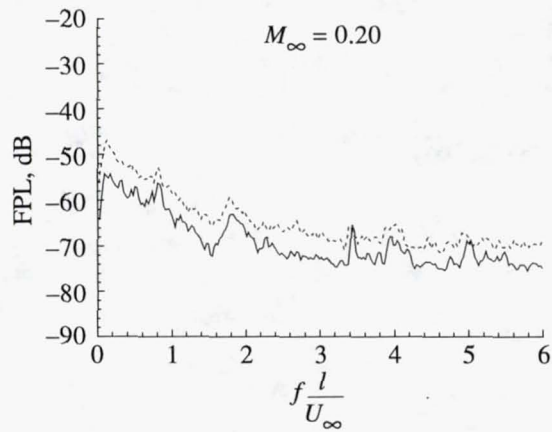
	w, in.	w/h
—	2.4	1
- - -	9.6	4



(g)  $l/h = 11$ .

Figure 21. Continued.

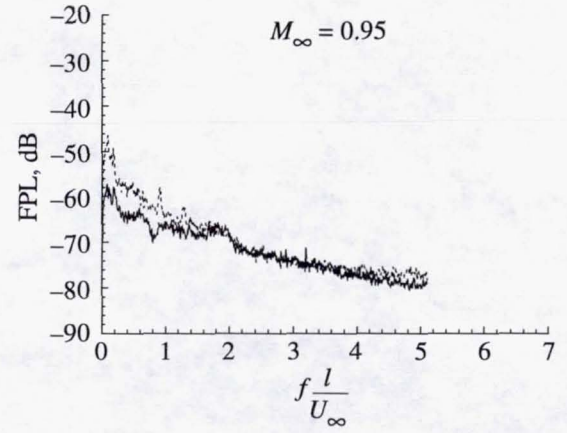
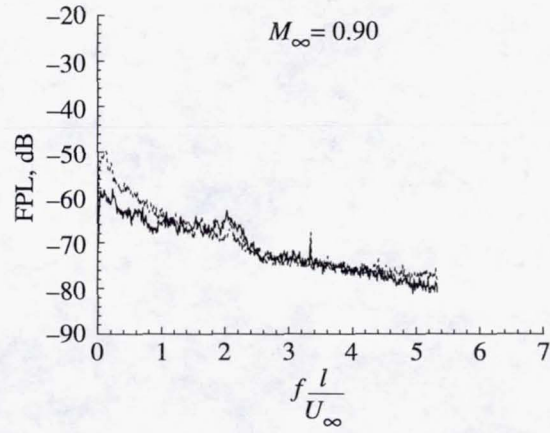
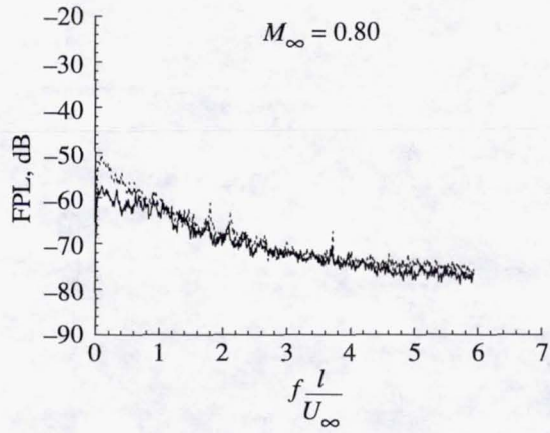
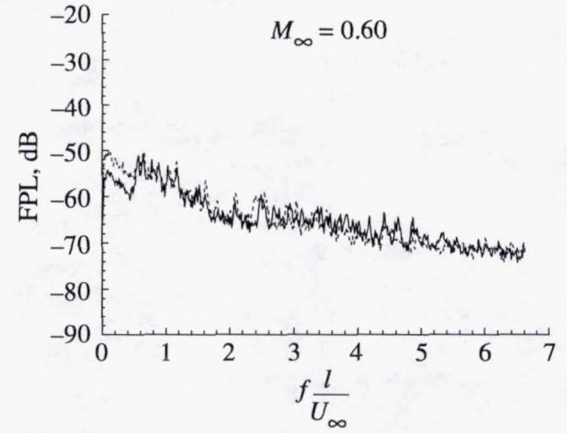
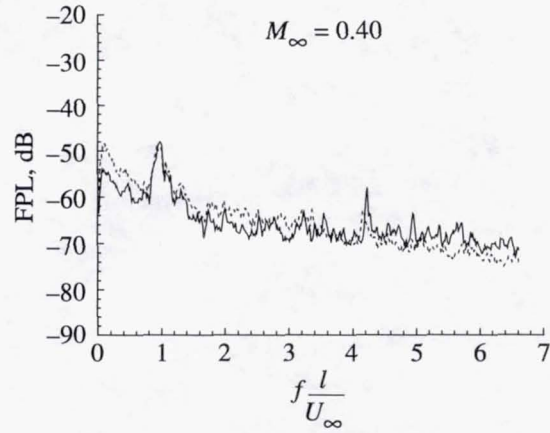
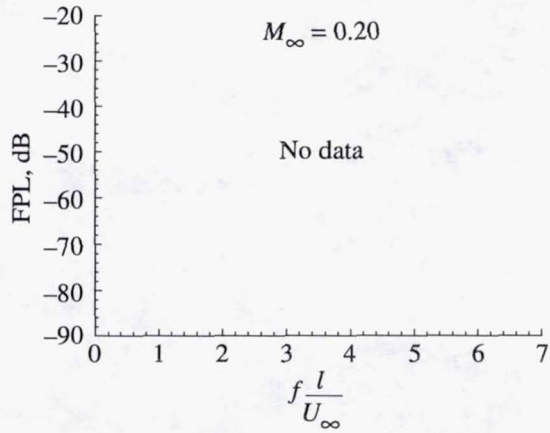
	<i>w</i> , in.	<i>w/h</i>
—	2.4	1
---	9.6	4



(h)  $lh = 12$ .

Figure 21. Continued.

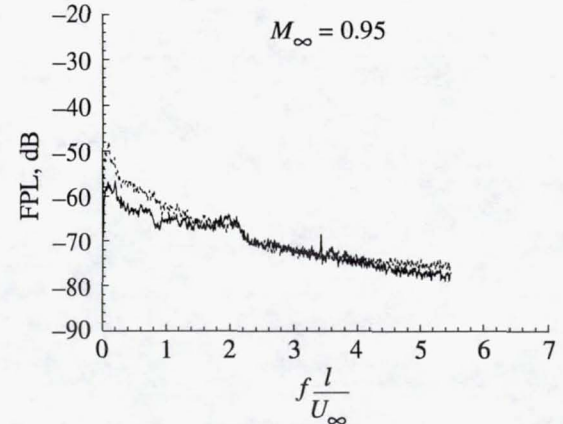
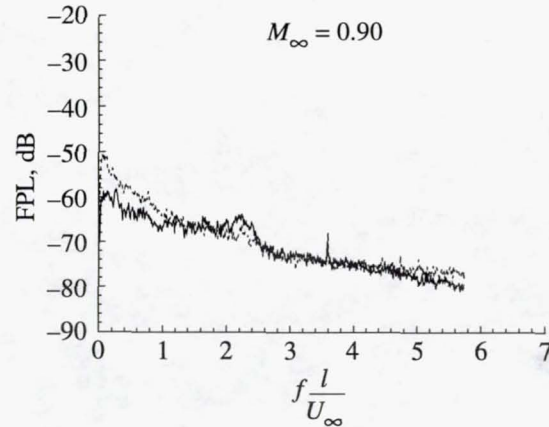
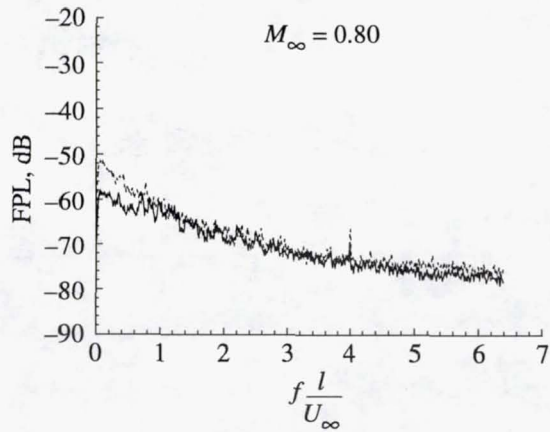
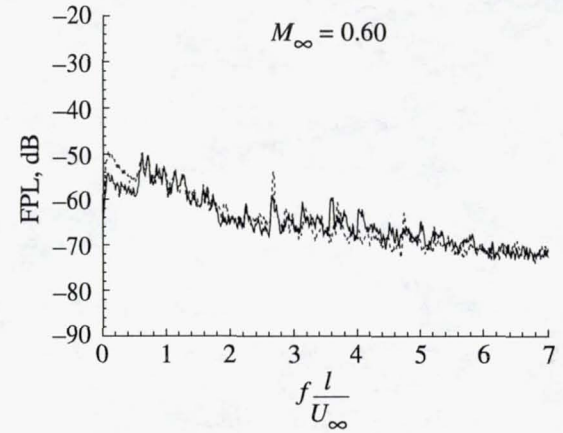
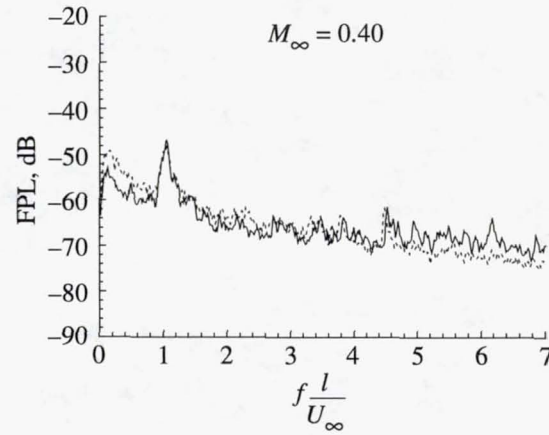
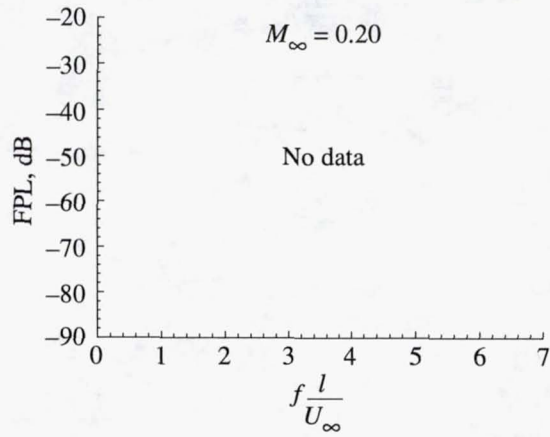
	$w, \text{ in.}$	$w/h$
—	2.4	1
- - -	9.6	4



(i)  $lh = 13.$

Figure 21. Continued.

	w, in.	w/h
—	2.4	1
---	9.6	4



(j)  $lh = 14$ .

Figure 21. Continued.

	w, in.	w/h
—	2.4	1
⋯	9.6	4

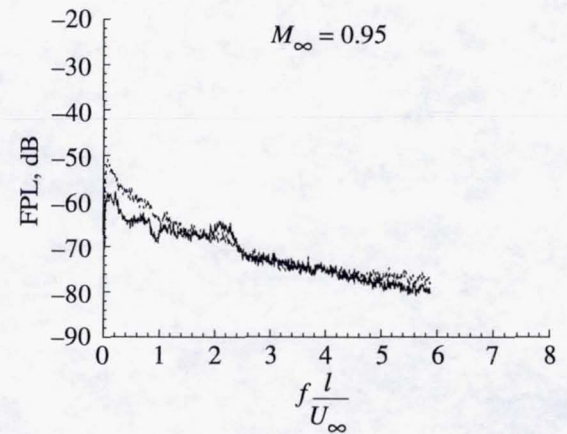
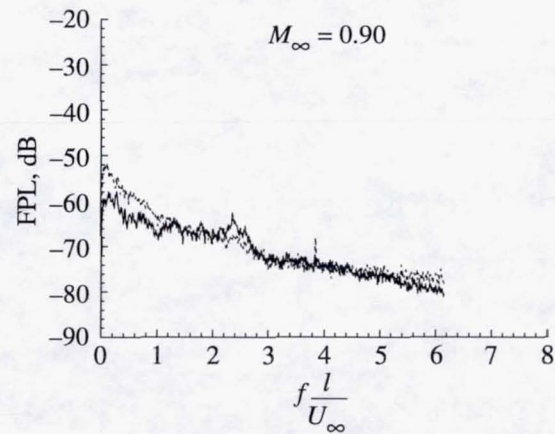
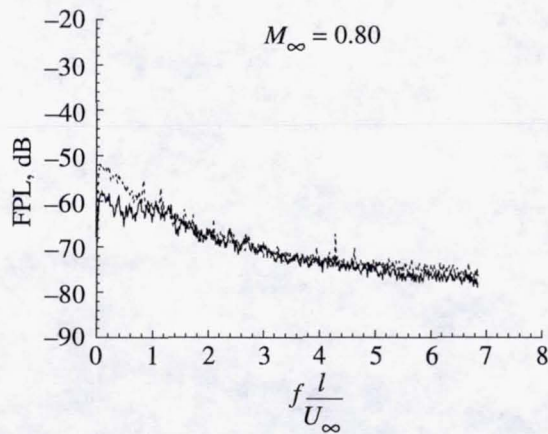
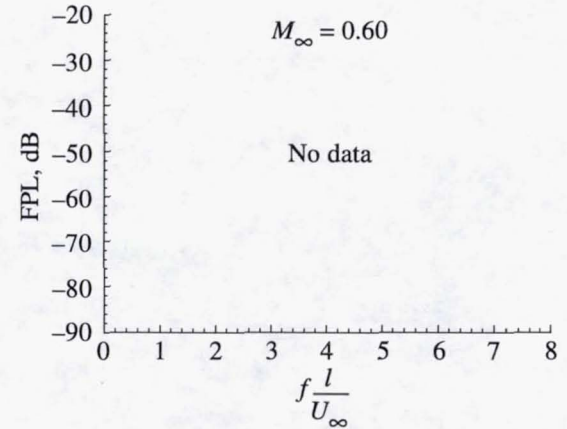
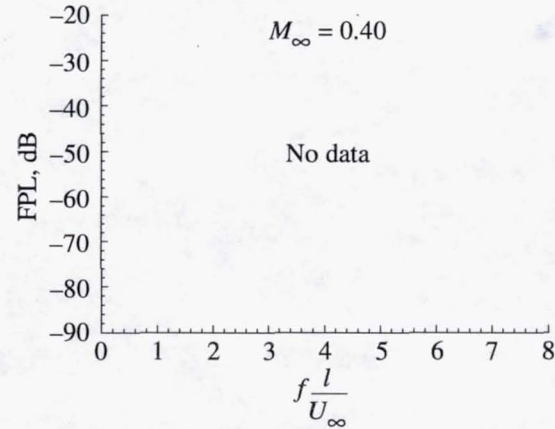
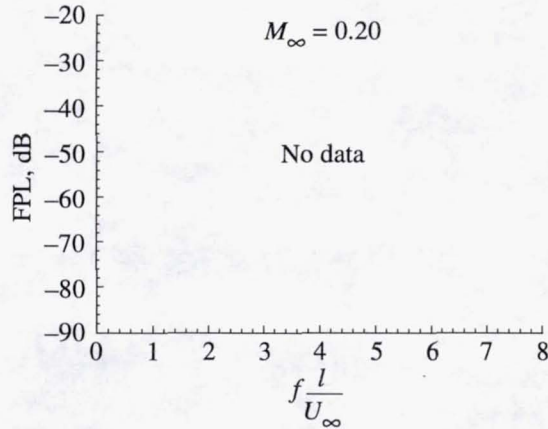
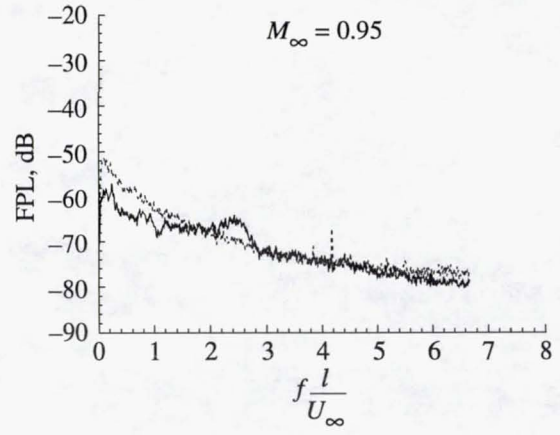
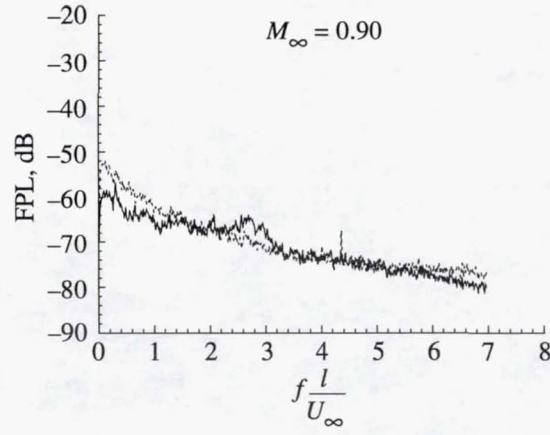
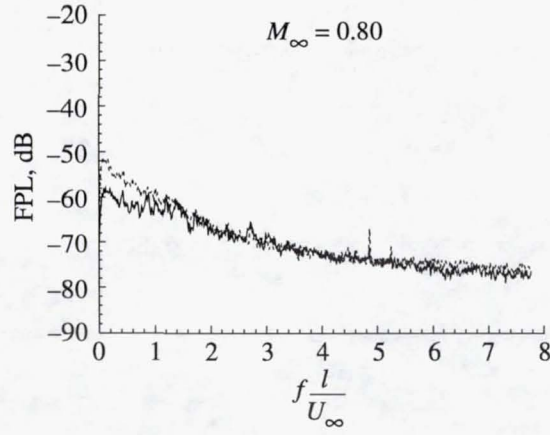
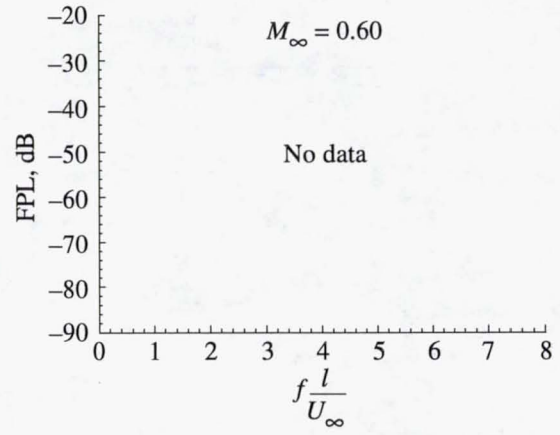
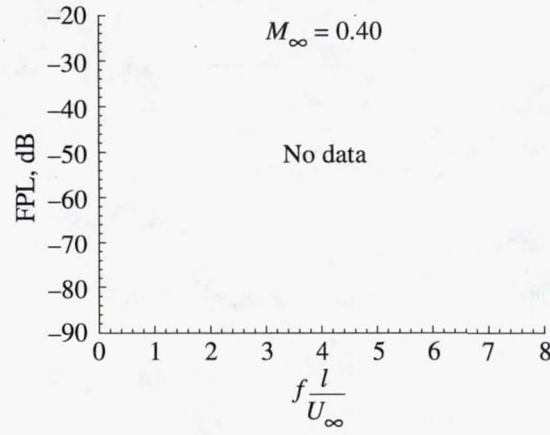
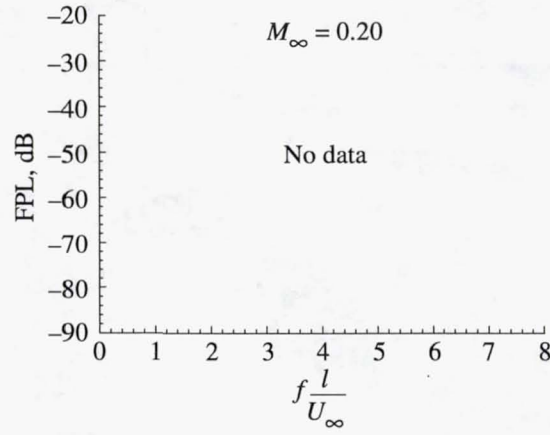
(k)  $l/h = 15$ .

Figure 21. Continued.

	w, in.	w/h
—	2.4	1
- - -	9.6	4



(1)  $lh = 17$ .

Figure 21. Concluded.

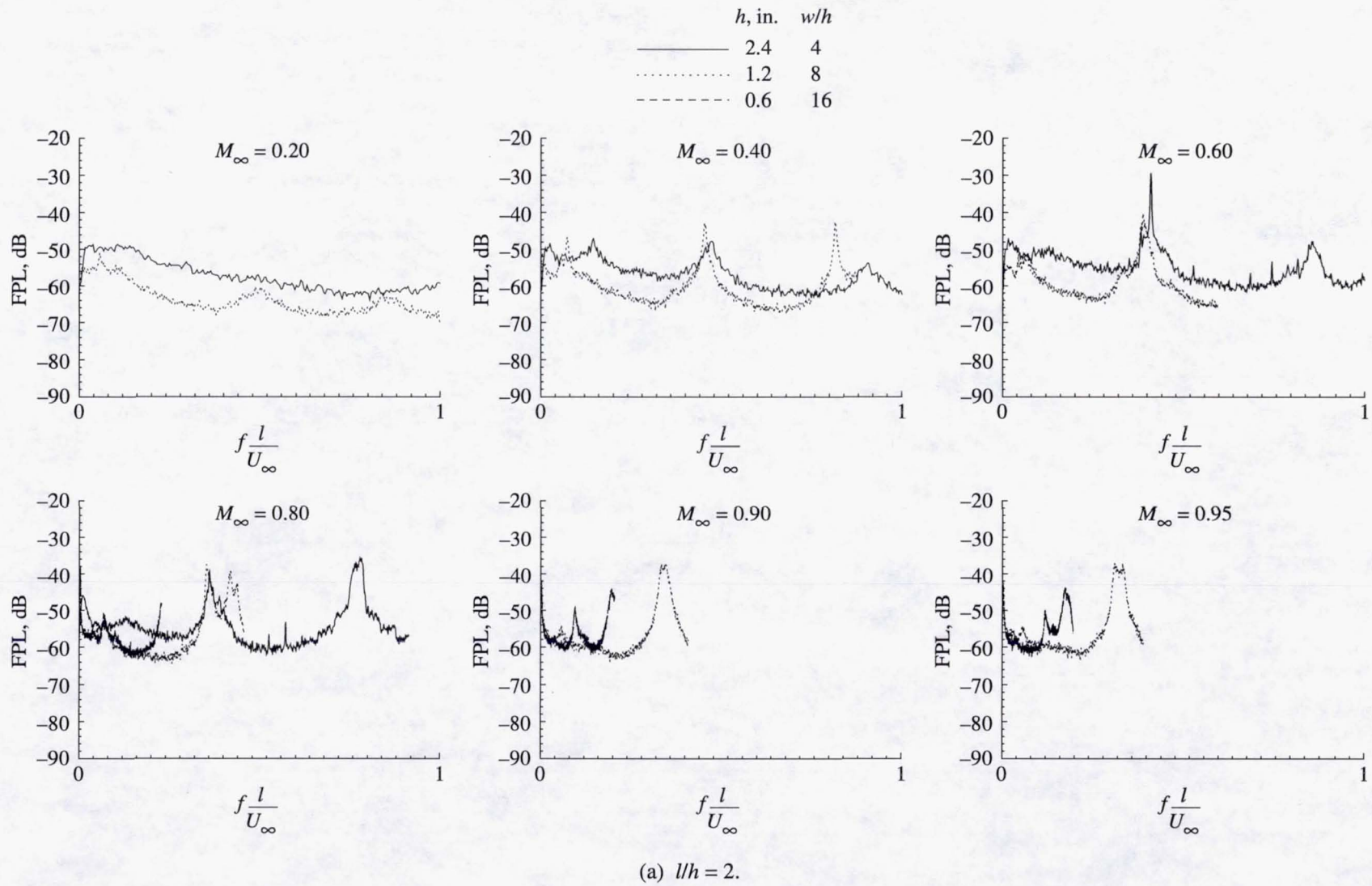
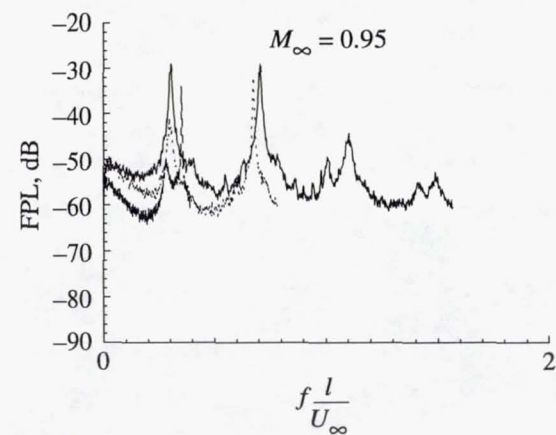
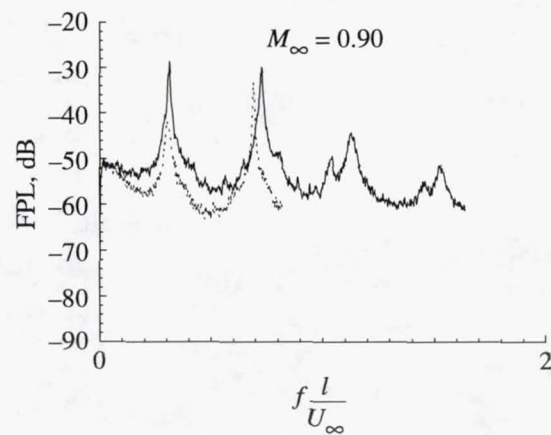
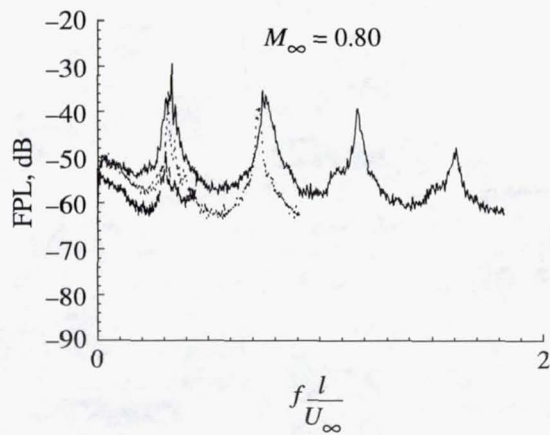
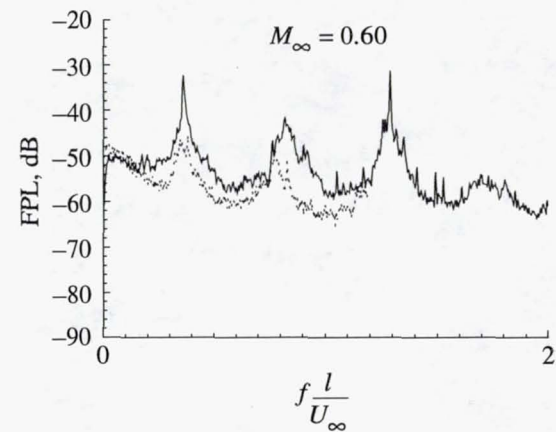
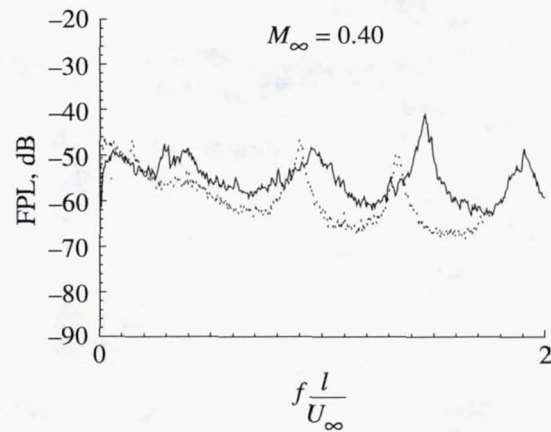
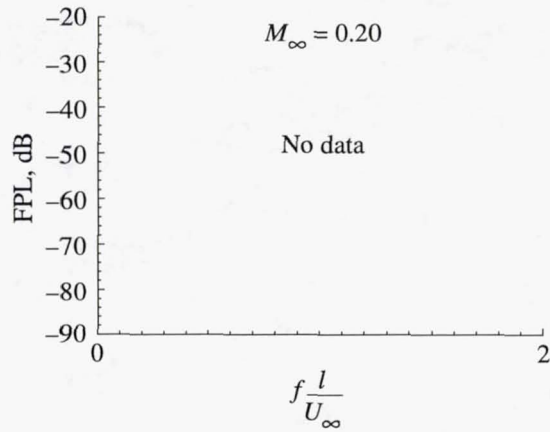


Figure 22. Effect of cavity depth on nondimensional unsteady-pressure spectra from transducer 1 for  $w = 9.6$  in.

$h$ , in.	$w/h$
—	2.4 4
⋯	1.2 8
- - -	0.6 16



(b)  $l/h = 4$ .

Figure 22. Continued.

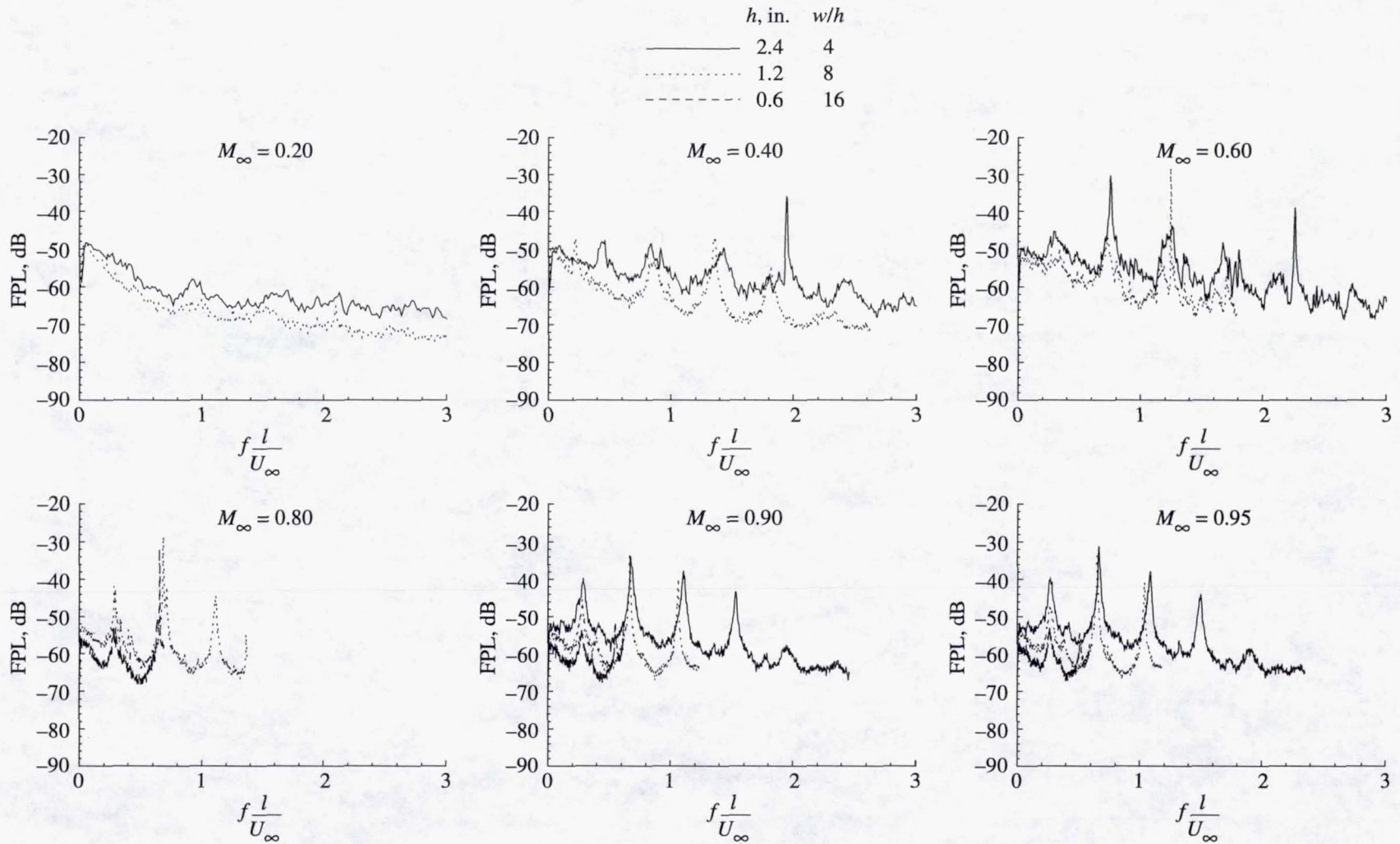
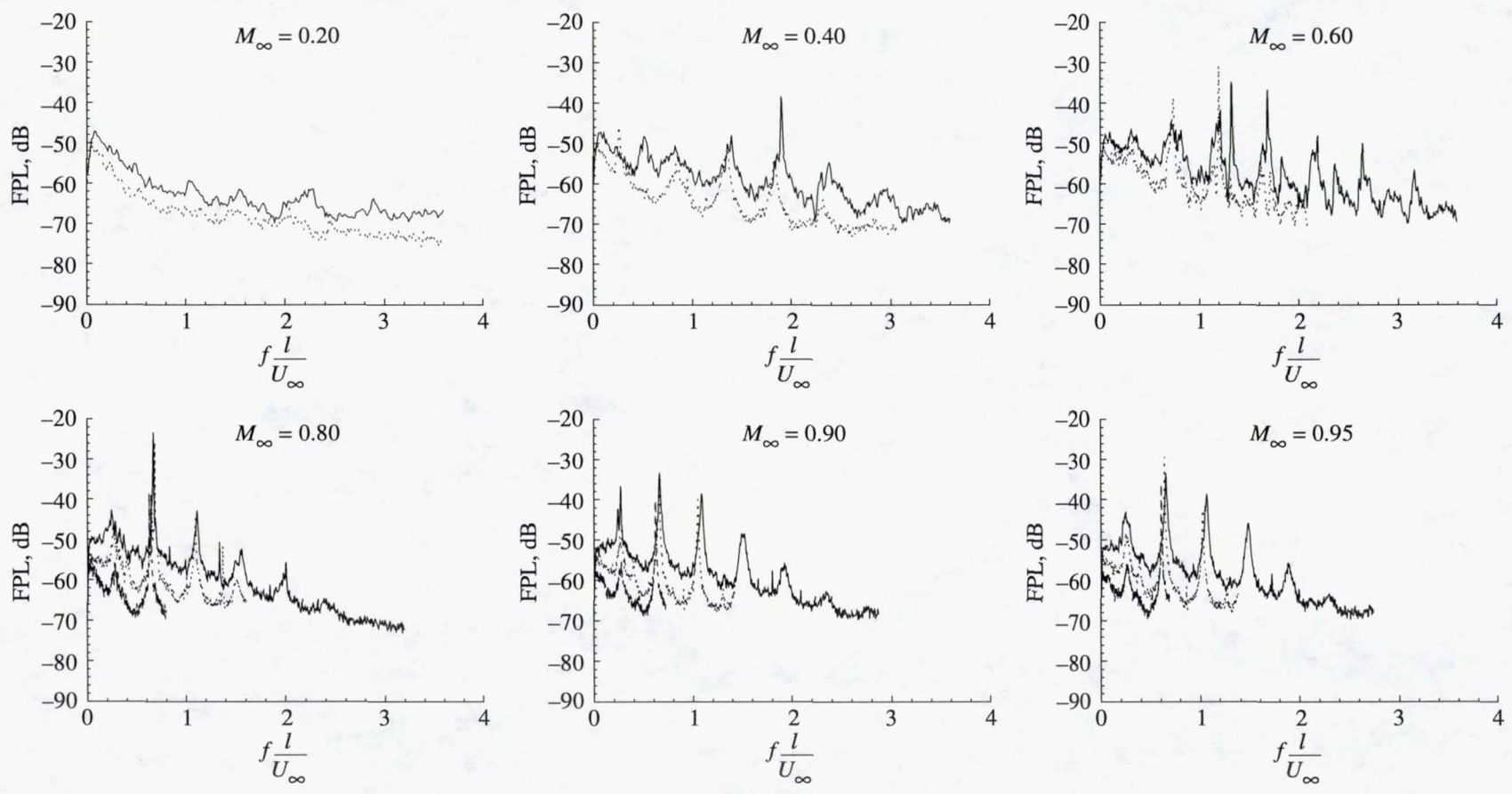
(c)  $l/h = 6$ .

Figure 22. Continued.

	$h$ , in.	$w/h$
—	2.4	4
⋯	1.2	8
- - -	0.6	16



(d)  $l/h = 7$ .

Figure 22. Continued.

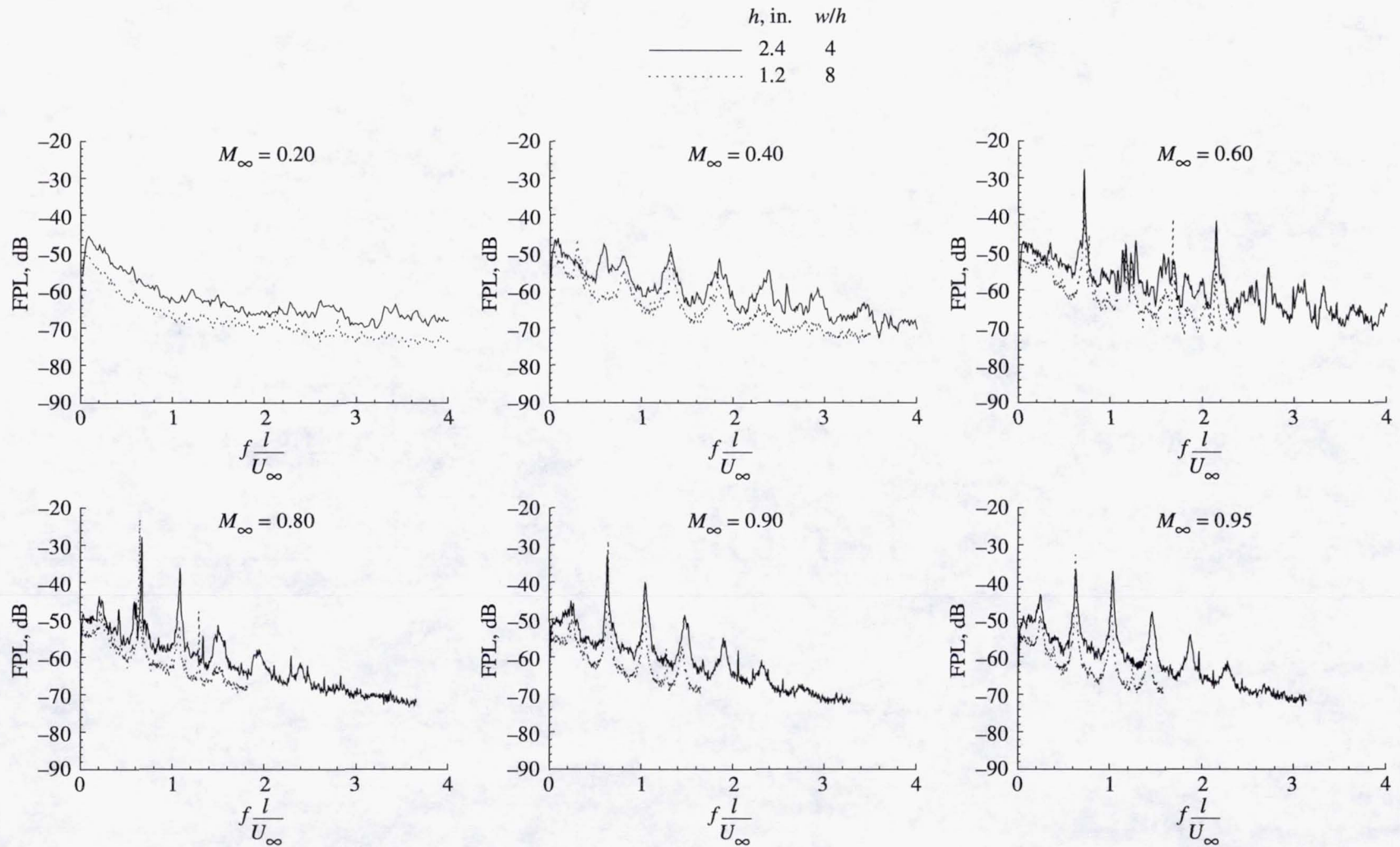
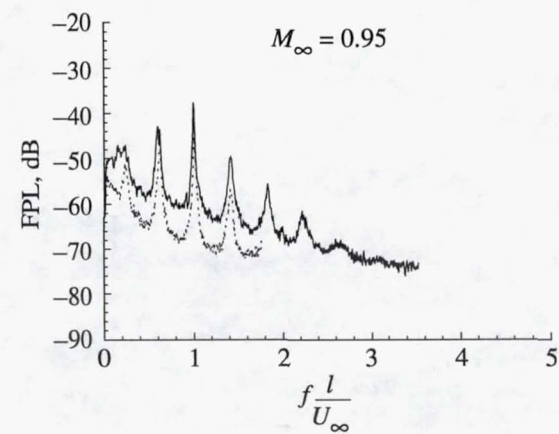
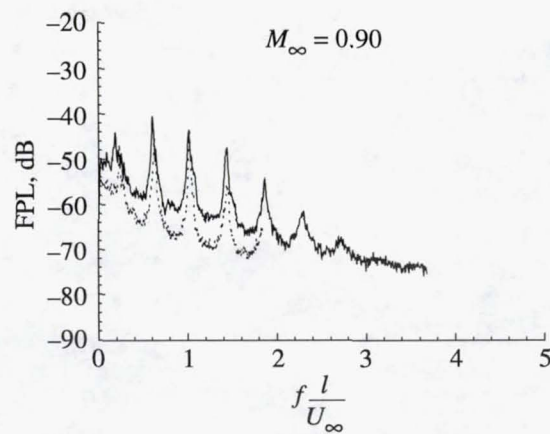
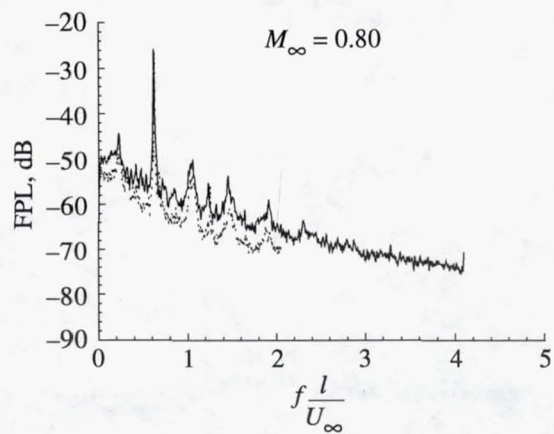
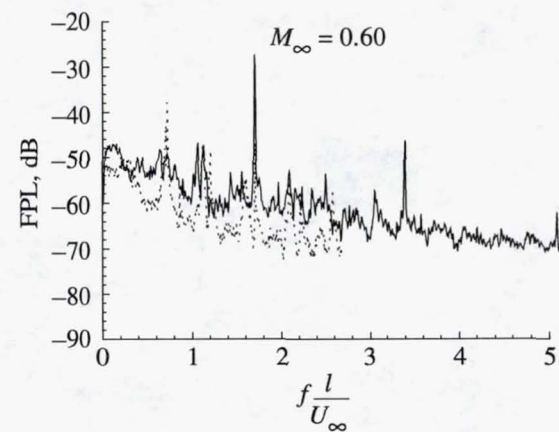
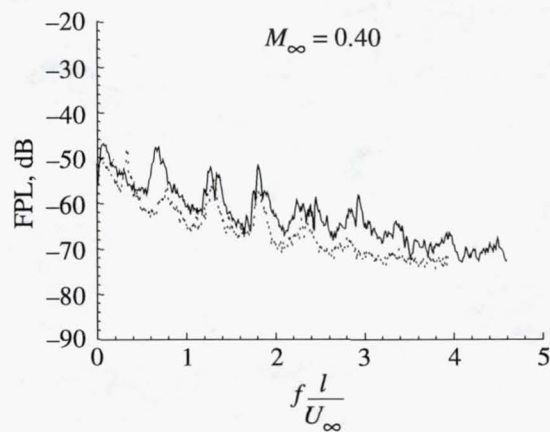
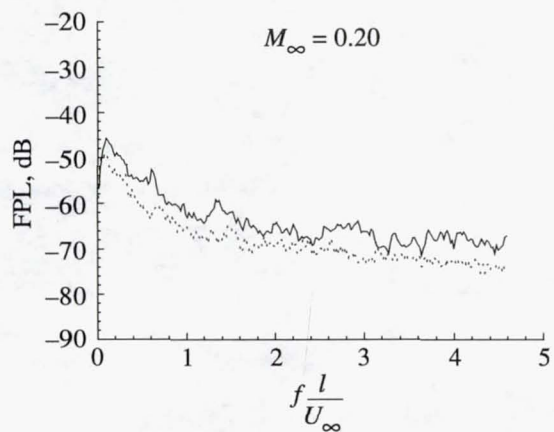
(e)  $l/h = 8$ .

Figure 22. Continued.

	<i>h</i> , in.	<i>w/h</i>
—————	2.4	4
·····	1.2	8



(f)  $l/h = 9$ .

Figure 22. Continued.

$h$ , in.	$w/h$
—	2.4 4
⋯	1.2 8

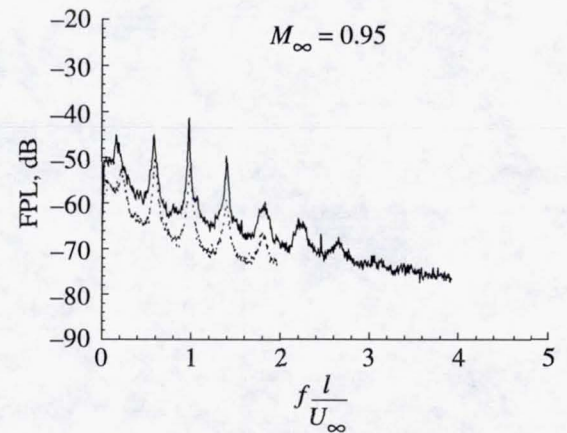
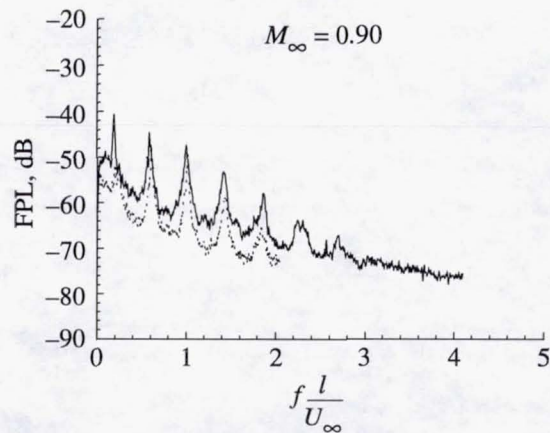
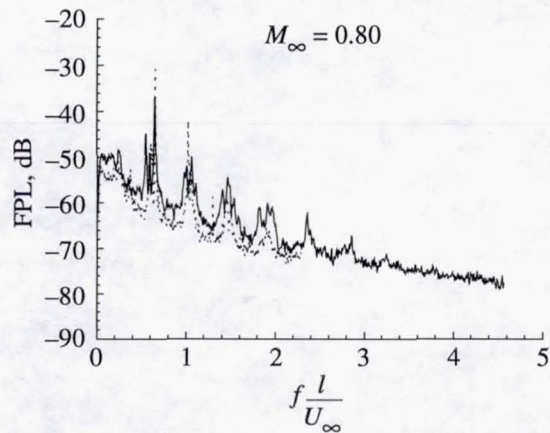
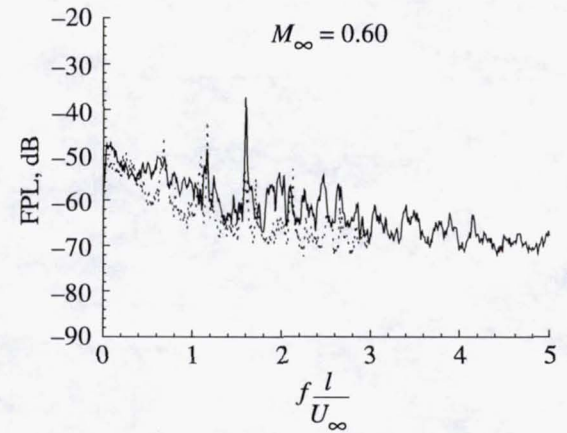
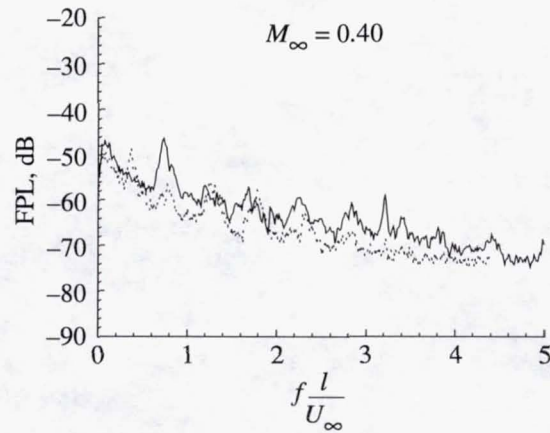
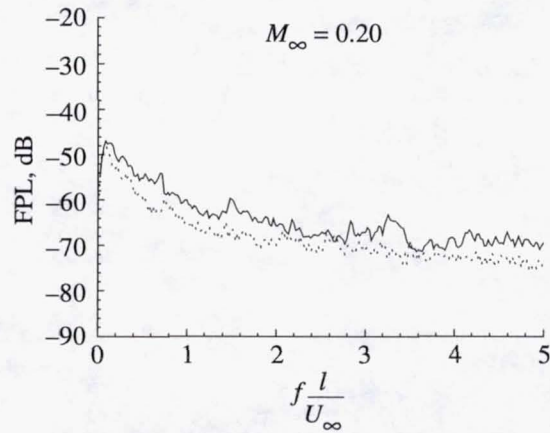
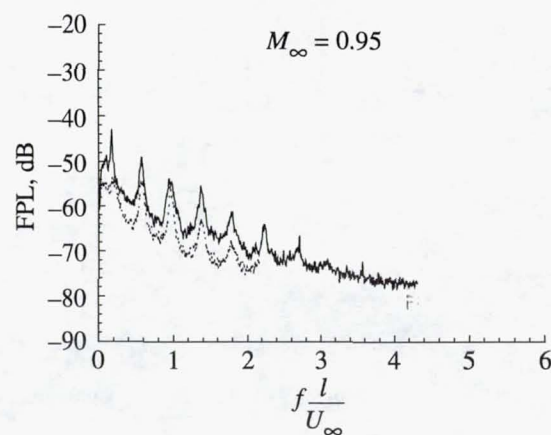
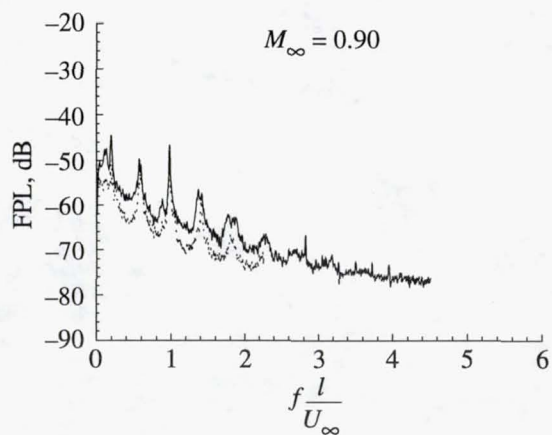
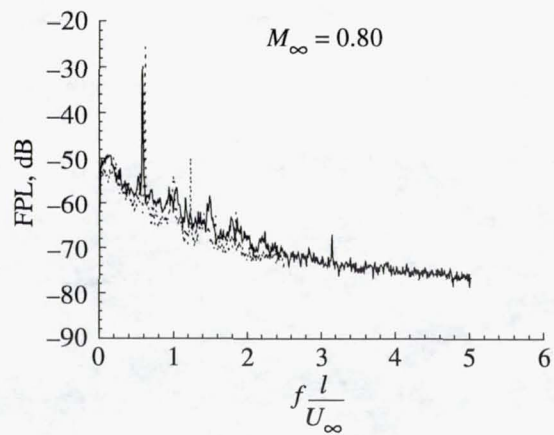
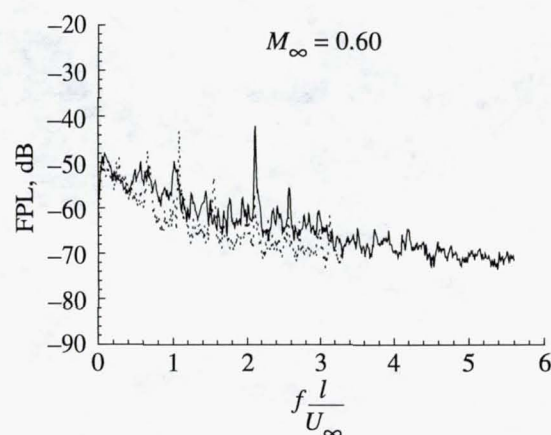
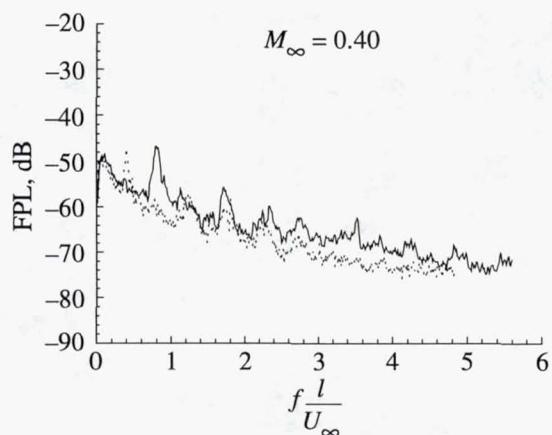
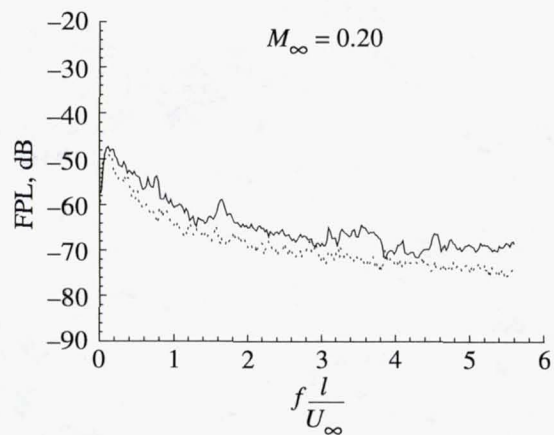
(g)  $l/h = 10$ .

Figure 22. Continued.

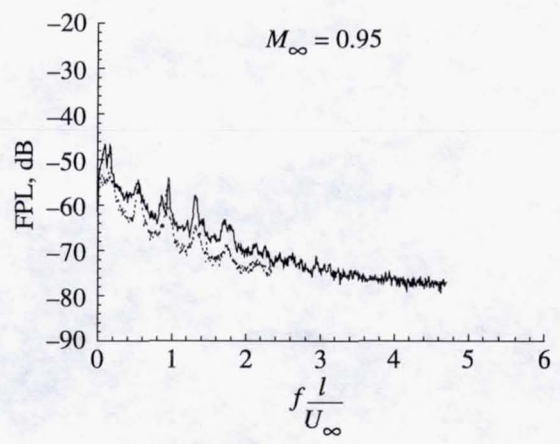
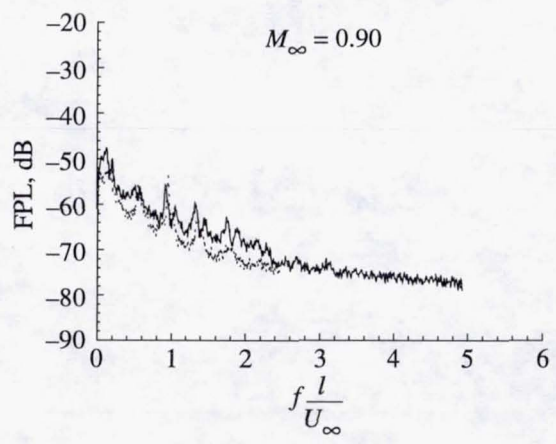
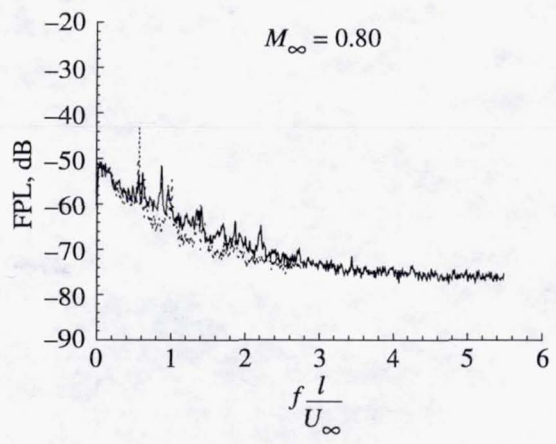
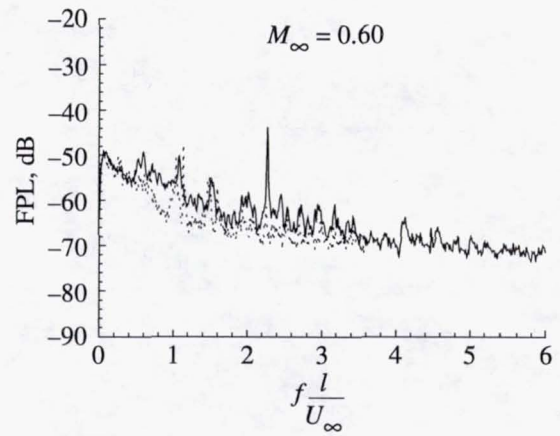
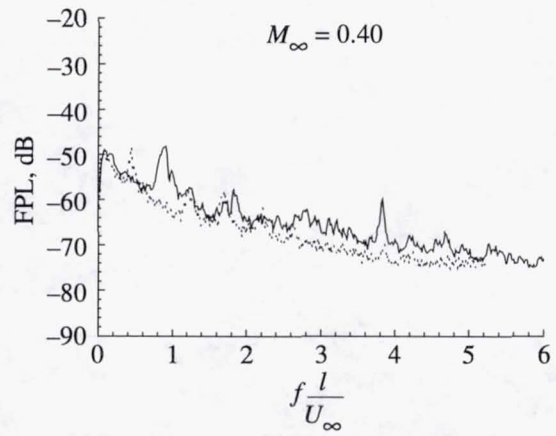
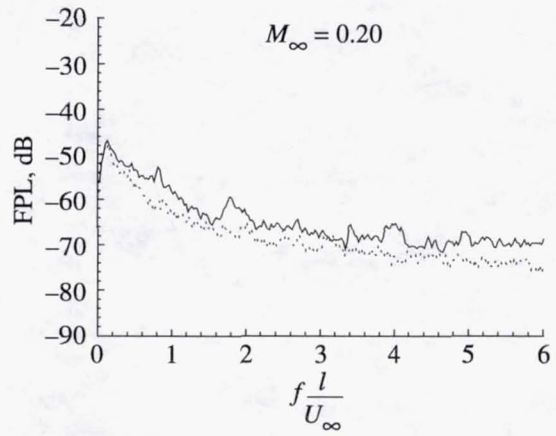
$h$ , in.	$w/h$
—	2.4    4
⋯	1.2    8



(h)  $l/h = 11$ .

Figure 22. Continued.

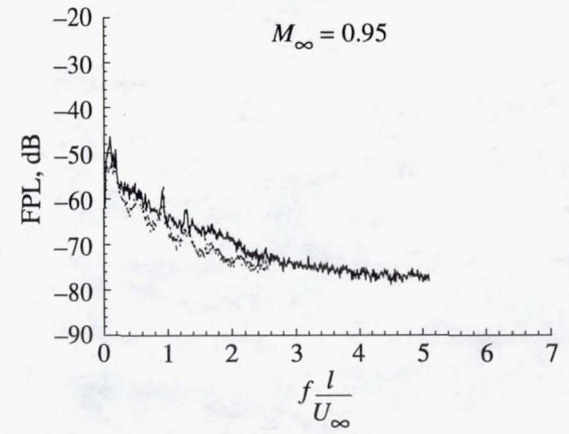
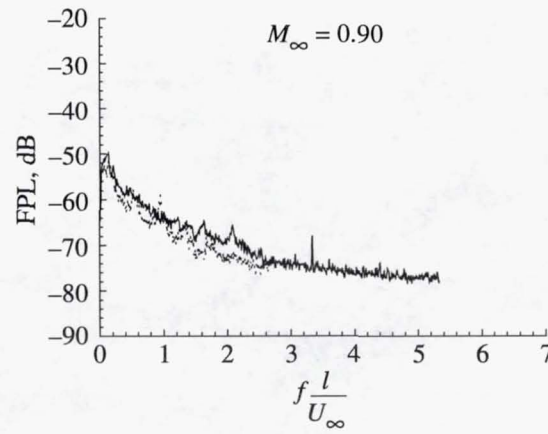
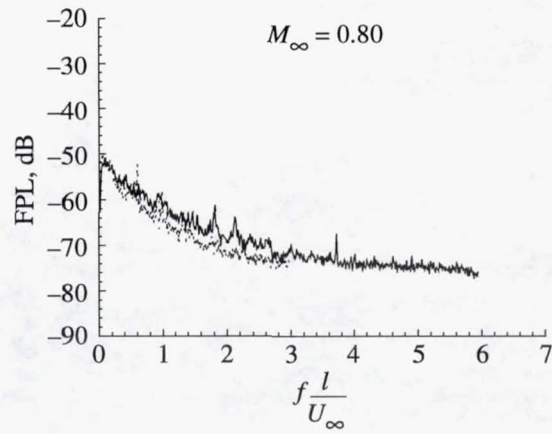
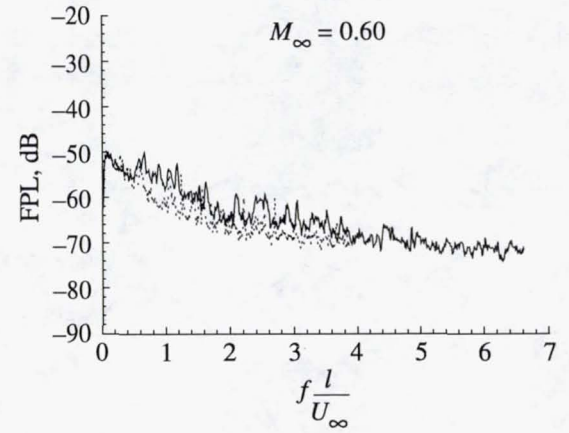
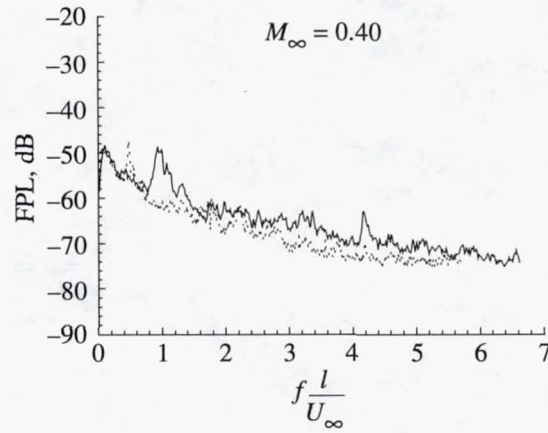
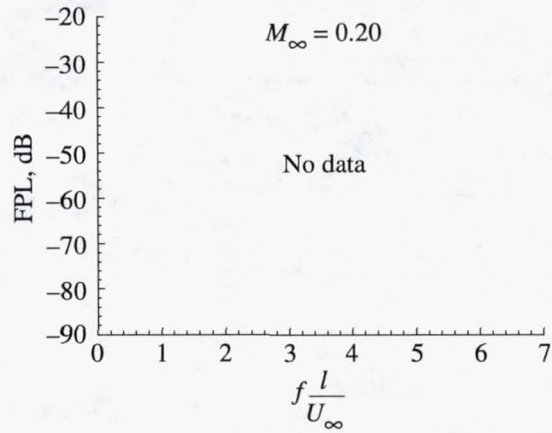
$h$ , in.	$w/h$
—	2.4 4
⋯	1.2 8



(i)  $lh = 12$ .

Figure 22. Continued.

	<i>h</i> , in.	<i>w/h</i>
—	2.4	4
⋯	1.2	8



(j)  $l/h = 13$ .

Figure 22. Continued.

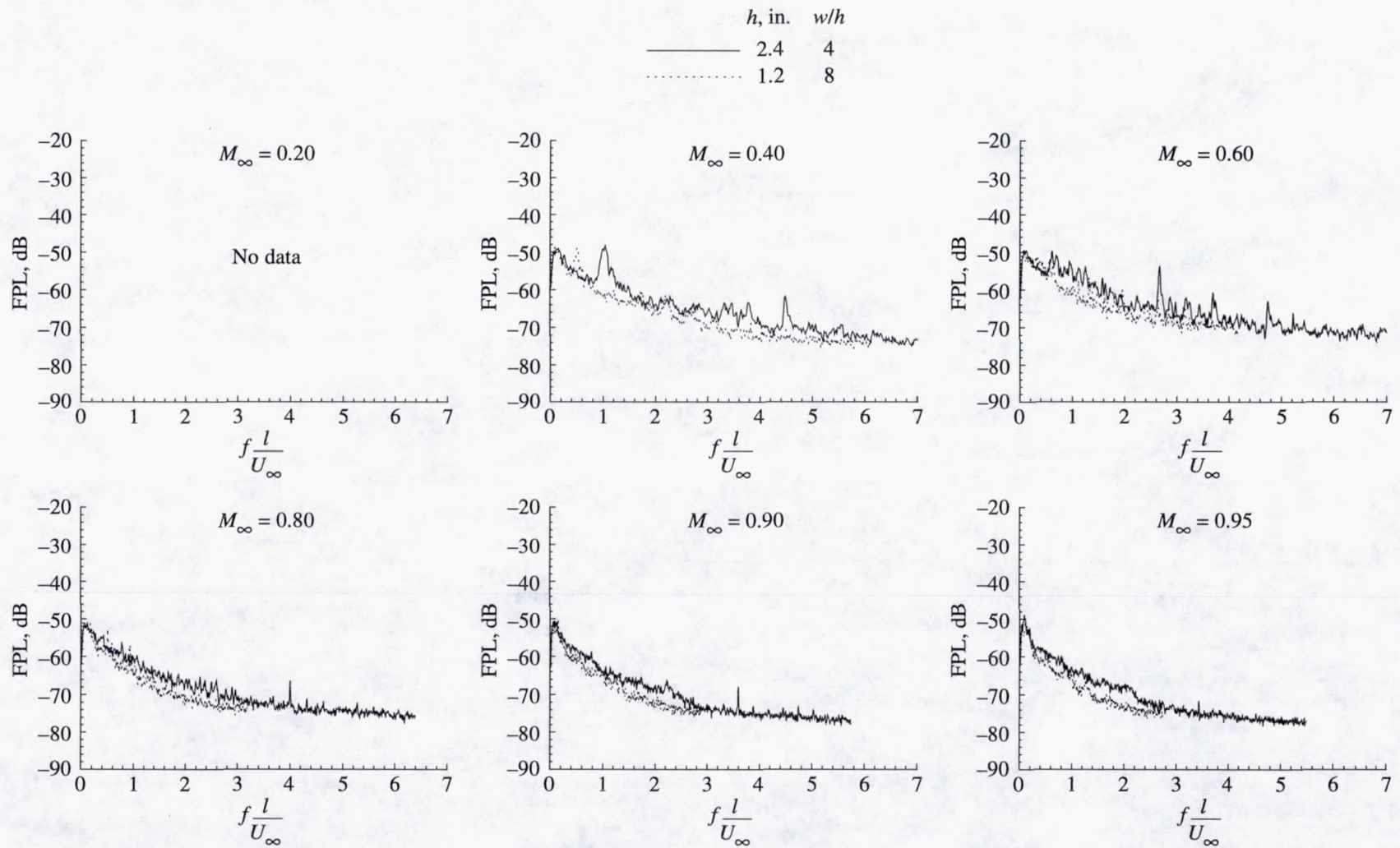
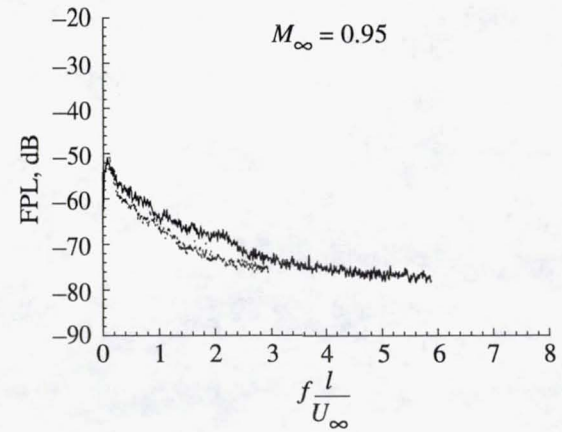
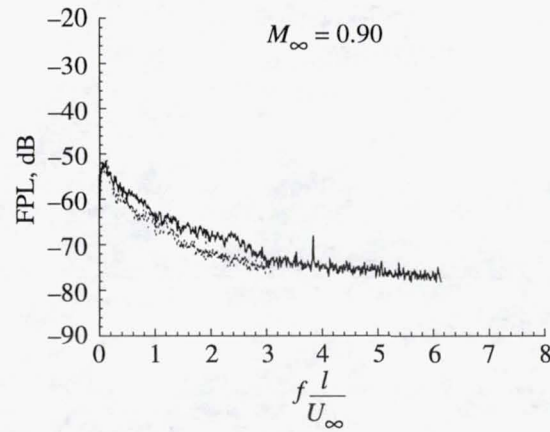
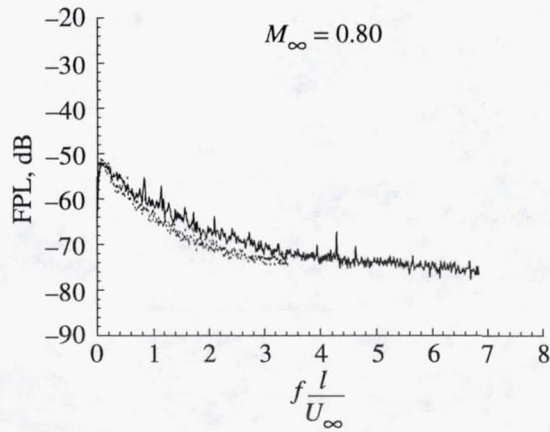
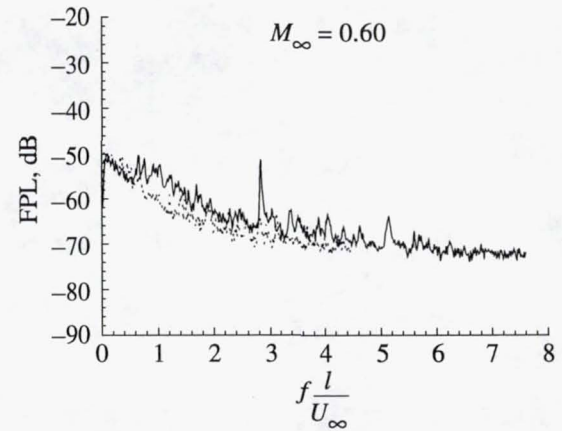
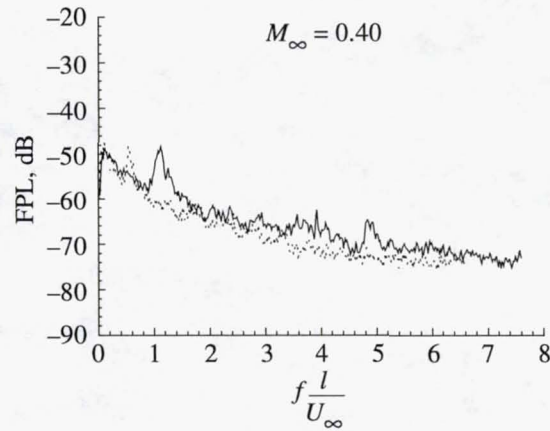
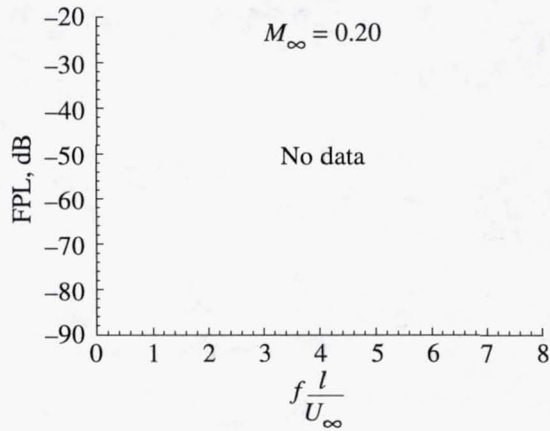
(k)  $l/h = 14$ .

Figure 22. Continued.

$h$ , in.	$w/h$
—	2.4    4
⋯	1.2    8



(1)  $l/h = 15$ .

Figure 22. Concluded.

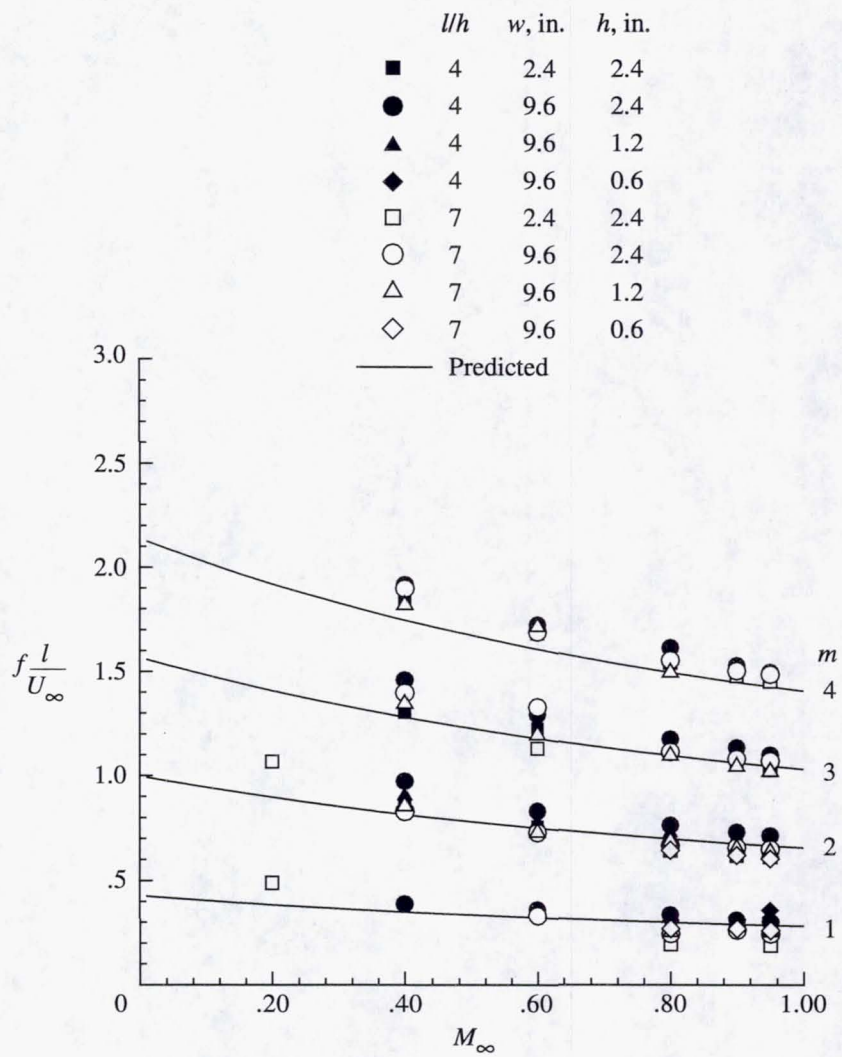


Figure 23. Nondimensional resonant frequencies.

An electronic "Supplement to NASA TP-3669" as a CD-ROM is available on request.

This supplement includes ASCII listings of the spectral data presented graphically in NASA TP-3669.

Requests for this "Supplement to NASA TP-3669" should be addressed to

ATTN USER SERVICES  
NASA CENTER FOR AEROSPACE INFORMATION  
800 ELKRIDGE LANDING ROAD  
LINTHICUM HEIGHTS MD 21090-2934

Cut here ✂ -----

Please send \_\_\_\_\_ copies of electronic "Supplement to NASA TP-3669" to

Attn: \_\_\_\_\_

Name

\_\_\_\_\_

Title

\_\_\_\_\_

Organization

\_\_\_\_\_

Street address

\_\_\_\_\_

City and State

\_\_\_\_\_

Zip code